



# *Research on Engineering Structures & Materials*

Volume 5 Issue 1  
February 2019

P-ISSN: 2148-9807 E-ISSN: 2149-4088

***J***

***R***

***E***

***S***

***M***

[www.jresm.org](http://www.jresm.org)



Research Group

The International Journal of **Research on Engineering Structures and Materials (RESM)** is a peer-reviewed open access journal (p-ISSN: 2148-9807; o-ISSN: 2149-4088) published by MIM Research Group. It is published in February, June and September.

The main objective of RESM is to provide an International academic platform for researchers to share scientific results related to all aspects of mechanical, civil and material engineering areas.

RESM aims the publication of original research articles, reviews, short communications technical reports, and letters to the editor on the latest developments in the related fields.

All expenditures for the publication of the manuscripts are most kindly reimbursed by *MIM Research Group*. Thus, authors do not need to pay for publishing their studies in the journal.

The scope of the journal covers (but not limited to) behavior of structures, machines and mechanical systems, vibration, impact loadings and structural dynamics, mechanics of materials (elasticity, plasticity, fracture mechanics), material science (structure and properties of concrete, metals, ceramics, composites, plastics, wood, etc.), nano-materials performances of new and existing buildings and other structural systems, design of buildings and other structural systems, seismic behavior of buildings and other structural systems, repair and strengthening of structural systems, case studies and failure of structural systems, safety and reliability in structural and material engineering, use of new and innovative materials and techniques in energy systems and mechanical aspects of biological systems (biomechanics and biomimetics).

**The topics covered in RESM include:**

- Structural Engineering
- Mechanical Engineering
- Material Engineering
- Earthquake Engineering
- Nano-technology
- Energy Systems

**Abstracting and Indexing**

Please visit <http://www.jresm.org> for more information.

**Graphics and Design**

Dr. H Ersen Balcioğlu

[ersen.balcioğlu@usak.edu.tr](mailto:ersen.balcioğlu@usak.edu.tr)



**RESEARCH on  
ENGINEERING STRUCTURES &  
MATERIALS**



**Published by MIM Research Group**

# RESEARCH on ENGINEERING STRUCTURES & MATERIALS

## Editorial Board

---

<b>Editor in Chief</b>		
Hayri Baytan Özmen	Usak University	Turkey
<b>Editor (Energy, Thermodynamics)</b>		
Canan Kandilli	Usak University	Turkey
<b>Editor (Mechanics, Materials)</b>		
H. Ersen Balcioglu	Usak University	Turkey
<b>Editor (Physics, Fluid Dynamics)</b>		
Antonio F. Miguel	University of Evora	Portugal
<b>Guest Editor</b>		
Süha Orçun Mert	Van Yüzüncü Yıl University	Turkey

---

## Editorial Office

---

<b>Publishing Manager &amp; Copyeditor</b>		
H. Ersen Balcioglu	Usak University	Turkey
<b>Publishing Assistant</b>		
Hakan Yilmaz	Pamukkale University	Turkey

---

### Editorial Board Members

---

Farid Abed-Meraim	Arts et Metiers ParisTech	France
P. Anbazhagan	Indian Institute of Science	India
Raffaele Barretta	University of Naples Federico II	Italy
R.S. Beniwal	Council of Scientific and Industrial Research	India
Antonio Caggiano	University of Buenos Aires	Argentina
Noel Challamel	University of South Brittany	France
Abdulkadir Çevik	Gaziantep University	Turkey
J. Paulo Davim	University of Aveiro	Portugal
Hom Nath Dhakal	University of Portsmouth	UK
S. Amir M. Ghannadpour	Shahid Beheshti University	Iran
Ali Goodarzi	Harvard University	USA
Jian Jiang	National Institute of Standards and Technology	USA
Ramazan Karakuzu	Dokuz Eylül University	Turkey
Arkadiusz Kwiecien	Cracow University of Technology	Poland
Stefano Lenci	Universita Politecnica delle Marche	Italy
Yuan Meini	North University of China	China
Stergios A. Mitoulis	University of Surrey	UK
Mohammad Mehdi Rashidi	University of Tongji	China
Pier Paolo Rossi	University of Catania	Italy
Neritan Shkodrani	Polythecnic University of Tirana	Albania
Faris Tarlochan	Qatar University	Qatar
Y.B. Yang	National Taiwan University	Taiwan

### Advisory Board Members

---

Irfan Ay	Balikesir University	Turkey
Fevzi Bedir	Gebze Technical University	Turkey
Tunde Bello-Ochende	Duke University	UK
Felipe Bertelli	Universidade Estadual de Campinas	Brazil
Alexei Biryukov	Donetsk National Technical University	Ukraine
Aslı Gunay Bulutsuz	Yıldız Technical University	Turkey
Şennur Candan	Bilecik University	Turkey
Habibe Demir	Iskenderun Technical University	Turkey
Ozgun Demircan	Ondokuz Mayıs University	Turkey
Nermin Demirkol	Kocaeli University	Turkey
Mehmet Emin Deniz	Batman University	Turkey
Sergey V. Dorozhkin	-	Russia
Elizaldo Domingues dos Santos	Universidade Federal do Rio Grande	Brazil
Erdogan Guk	Loughborough University	UK
Mehmet Gavgali	Atatürk University	Turkey
Gökhann Gece	Ankara University	Turkey
Khashayar Hosseinzadeh	Babol Noshirvani University	Iran
Serkan Islak	Kastamonu University	Turkey
Liércio AndreIsoldi	Universidade Federal do Rio Grande	Brazil
Mariatti Jaafar	Universiti Sains Malaysia	Malaysia
Draiche Kada	Universita Ibn Khaldoun de Tiaret	Algeria
Abdullah Cahit Karaođlanlı	Bartın University	Turkey
Hamid Khan	National University of Computer and Emerging Sciences	Pakistan
K. Mahato	National Institute of Technology	India

## Advisory Board Members

---

Upendra K. Mallela	Largy Services Limited	India
Faruk Mert	Gazi University	Turkey
V. Mohanavel	St. Peter's University	India
Sobhan Mosayebidorcheh	Babol Noshirvani University	Iran
Márcio Wrague Moura	Universidade Federal do Rio Grande	Brazil
Enea Mustafaraj	Epoka University	Albania
Seung Hoon Nahm	Center for Energy Materials Metrology	Republic of Korea
George Oguntala	University of Bradford	UK
Philip Oladijo	Botswana International University	Botswana
Serkan Özel	Bitlis Eren University	Turkey
Hayri Baytan Ozmen	Usak University	Turkey
Luiz Rocha	Universidade do Vale do Rio dos Sinos	Brazil
Binnur Sağbaş	Yıldız Technical University	Turkey
Gözde Sarı	Celal Bayar University	Turkey
Hakan Sarıkaya	Usak University	Turkey
Yakup Say	Munzur University	Turkey
Ramachandran Chidambaram Seshadri	Stony Brook University	USA
Mohsen Sheikholesmani	Babol Noshirvani University	Iran
Sushil Kumar Singh	Motilal Nehru National Institute of Technology	India
Faris Tarlochan	Qatar University	Qatar
Hamide Tekeli	Süleyman Demirel University	Turkey
Mehmet Topuz	Yüzüncü Yıl University	Turkey
Gül Tosun	Fırat University	Turkey

## Advisory Board Members

---

Şaban Uysal	Karabük University	Turkey
Flavia Zinani	Universidade do Vale do Rio dos Sinos	Brazil

## In This Issue

### Research Article

- 1 **Hakan Sarıkaya, Gülşah Susurluk**  
Effect of polypropylene fiber addition on thermal and mechanical properties of concrete

### Research Article

- 13 **Vebil Yıldırım**  
Exact radial free vibration frequencies of a thick-walled sphere made of an isotropic and homogeneous material – A case study with a carbon nanofiller reinforced aluminum hollow sphere

### Research Article

- 33 **Zeynep Ömeroğulları Başyigit**  
Inclusion compound formation between hazelnut oil and gamma cyclodextrin

### Research Article

- 43 **M. G. Sobamowo**  
Finite element analysis of transient thermal performance of a convective-radiative cooling fin: effects of fin tip conditions and magnetic field

### Research Article

- 75 **Canan Kandilli**  
Finite element analysis of transient thermal performance of a convective-radiative cooling fin: effects of fin tip conditions and magnetic field

Free access to tables of content, abstracts and full text of papers for web visitors.

Copyright © 2019  
Research on Engineering Structures & Materials  
MIM Research Group Publications  
ISSN 2148-9807  
<http://www.jresm.org>

Research on Engineering Structures & Materials  
MIM Reseach Group Publications  
ISSN 2148-9807  
<http://www.iresm.org>

## ABSTRACTING / INDEXING

The international journal of Research on Engineering Structures and Materials (RESM) is currently Abstracted/Indexed by CrossRef, Google Scholar, Universal Impact Factor, Scientific Indexing Service, Research Bible, CiteFactor, Electronic Journal Library, Open Academic Journals Index, Global Impact Factor, Directory of Research Journals Indexing, Materials Science & Engineering Database (ProQuest) Engineering Journals (ProQuest), ULAKBİM TR Index (Tubitak) and under evaluation by many other respected indexes.

Check web site for current indexing info.





Research Article

## Effect of polypropylene fiber addition on thermal and mechanical properties of concrete

Hakan Sarıkaya<sup>\*a,1</sup>, Gülşah Susurluk<sup>b,2</sup>

<sup>1</sup> Civil Engineering Department, Faculty of Engineering, Uşak University, Uşak, Turkey

<sup>2</sup> Textile Technology Department, Associate's Degree Vocational School, Beykent University, Istanbul, Turkey

### Article Info

#### Article history:

Received 9 Nov 2018

Revised 3 Jan 2019

Accepted 22 Jan 2019

#### Keywords:

Fiber concrete;

Polypropylene fiber;

Mechanical strengths

### Abstract

The concrete is a brittle material which has low tensile strength and tensile strain capacity. These weak points of concrete can be fixed by using fibers made of different materials with high technical specifications in concrete. In this study, it is aimed to investigate the physical and mechanical properties of concretes obtained by using polypropylene fibers at different ratios by keeping amount of cement constant in the concrete mixtures. 100x100x100 mm cube specimens for compressive strength, 100x100x500 mm beam specimens for tensile strength in bending tests were produced. Also, 100x100x100 mm cube specimens for thermal conductivity tests were produced and these samples were tested by cutting to 80x40x10 mm. It was observed that as the rates of fibers were increased, ultrasonic velocity, water absorption and flexural strength were increased but slump, thermal conductivity coefficient and compressive strength were decreased.

© 2018 MIM Research Group. All rights reserved.

## 1. Introduction

Since the existence of humankind, the second basic necessity has been the sheltering after the necessity of eating and drinking, In this way the building sector has always remained on the agenda and has continued to work on developing practical methods. In today's world, as in all areas, the basic goal is to reach the solution at the earliest with minimal expenditure. Various special properties have been developed or some special concrete with different production and application techniques are widely used due to emerging needs in today's use. It is very important to design and economical production of concrete for the purpose of use [1]. Due to the increase in the world population, complex and multi-storey buildings have been widespread in recent years instead of simple and single storey buildings. As the building height and number of floors increase, the quality of the material used becomes important [2]. In multi-storey buildings, concrete performance is of great importance in order to reduce the structural safety and the effect of the earthquake [3].

Concrete; is a composite material consisting of mortar phase and aggregate which is obtained by mixing cement, water, aggregate and additives if necessary (mineral, chemical, fiber etc.) in certain conditions and ratios. Concrete is in plastic form at the beginning and gains resistance by hardening due to chemical reaction (hydration) over time between cement and water [4]. When concrete has just been mixed, it takes the name of fresh

\*Corresponding author: [hakan.sarikaya@usak.edu.tr](mailto:hakan.sarikaya@usak.edu.tr)

<sup>a</sup>[orcid.org/0000-0002-8043-3302](http://orcid.org/0000-0002-8043-3302); <sup>b</sup>[orcid.org/0000-0003-3284-2248](http://orcid.org/0000-0003-3284-2248)

DOI: <http://dx.doi.org/10.17515/resm2018.72ma1109>

Res. Eng. Struct. Mat. Vol. 5 Iss. 1 (2019) 1-12

concrete and when it hardens it becomes hardened concrete [5]. When the materials which form the composition in concrete, are specifically rated, the mixture can be poured anyplace and brings a plastic mass that can take the shape of the mold [6].

The concrete is a brittle material which has low tensile strength and tensile strain capacity. Conventional concrete is typically shows poor performance in terms of fatigue strength, cavitation, abrasion resistance, tensile strength, deformation capacity, shear strength, load carrying strength after cracking and toughness. Where these properties of concrete are obviously required, the addition of high-tech fibers produced from different materials within the concrete improves the above weaknesses of the concrete. Thus, polypropylene fiber, carbon fiber, plastic-glass based fibers and steel fibers have begun to be used in concrete. In terms of advantages in the field of Civil Engineering, the importance of fiber reinforced concrete is increasing rapidly and important steps have been taken to improve the properties of composites [7].



Fig. 1 Polypropylene Fiber

The polypropylene fiber used in this study is a very light polymer that is grouped within the thermoplastics as material type. It forms almost half of the raw materials used in daily life such as clothes hangers, kitchen and bathroom utensils, buttons, electrical materials, cables, yarns, laboratory utensils, stretch films, automotive Industry, etc. From this point of view, it is also possible to say that polypropylene fiber is a cheap plastic to manufacture. The most important effect of polypropylene fiber in concrete or plaster is to control cracks due to plastic shrinkage within the first few hours after pouring concrete into the mold. In the first phase of concrete hardening, the rate of formation of concrete strength is slower than the rate of formation of tensile stresses due to shrinkage. This plastic shrinkage is essentially a natural consequence of evaporation and chemical reaction starting between water and cement [8]. Polypropylene fibers are not very effective in increasing the mechanical strength of concrete compared to steel fibers. Nevertheless, they give energy absorbing capability to concrete at minimum levels and they are very effective in plastic shrinkage. Polypropylene fibers are particularly preferred against non-strong shrinkage. The function of polypropylene fibers is limited with the soft, plastic phase of concrete, the strength-enhancing effect of the steel fibers also persists significantly after the concrete setting and hardening. Steel fibers also have a crack-proof and limiting effect in the plastic phase of concrete. However, it is weaker than the effect of polypropylene fibers dispersed perfectly in concrete (Fig. 1). In addition, steel fibers give the material a certain strength and toughness, which significantly increases the strength of the concrete and reduces the cracks that will occur in hardened concrete due to their long-term drying shrinkage [9].

If we look at the literature studies using polypropylene fiber in concrete;

According to Acıkgenc et al [10] polypropylene fibers were added into concrete by the rate of 1% and 2% by volume and concrete samples were produced. When the fiber ratio is 1% in concrete, the compressive strength of the concrete is increased, and the compressive strength of concrete is decreased when it is 2%. In addition, as the water/cement ratio decreased, the compressive strength increased and the flexural strength increased as the fiber ratio increased. Likewise, capillary water absorption and abrasion resistance properties of concrete were also positively affected by polypropylene fibers. As the properties of fresh concrete and concrete mixture proportions were changed, polypropylene fibers had different influence on strength and durability. According to Sumer and Saribiyik [11] polypropylene fiber and silica fume were added into concrete by the rate of 0.1%, 0.5% and 1% by volume and concrete samples were produced. It was observed that as the fiber ratio increased, compressive and flexural strength increased. Likewise, it has been determined that polypropylene fiber has a positive effect on the abrasion resistance and capillary water absorption properties of the concrete and it would be appropriate to use it in field concrete. According to Salahaldeen and Muhsen [12] concrete cube samples of 150 mm x 150 mm x 150 mm dimensions were produced by using rate of 1%, 1.5% and 2% polypropylene fiber in concrete. The compressive strengths of concrete samples were investigated and the percentage increase of compressive strength of polypropylene fiber concrete mixes compared to the mix without fiber is observed from 4 to 12%. According to Topcu et al [13] polymer based polypropylene fibers were added to mortar mixtures in ratio of 0.6% 0.8% 0.9% and 1.1% by volume. On the mortars, compressive strength, flexural strength, ultrasonic velocity, water absorption and dynamic modulus of elasticity were defined and compared with control samples. According to experimental results, it was seen that when the compressive strength and dynamic modulus of elasticity was decreased by addition of fibers to mortar, flexural strength and water absorption was slightly increased. According to Sohaib et al [14] concrete samples were produced using polypropylene fiber instead of cement at 0.5%, 1.5%, 2.5%, 3.5% and 4.5%. The compressive and tensile strengths of concrete samples were investigated. It was seen that the compressive strengths increased by 11% compared to the control samples and the tensile strengths increased by 17% compared to the control samples as 1.5% of cement contents; however, after 1.5%, the compressive and tensile strengths decreased.

As known, various fiber added materials are used to make the concrete more durable and more impermeable. One of them is polypropylene fiber. Also, the tensile strength of concrete is weak, various fibers are used to increase tensile strength. In this study; investigation of the effects of polypropylene fiber on the compressive and flexural strength of concrete and the effectiveness of polypropylene fibers in preventing the cracking of concrete due to tensile stresses on the surface in concretes with high surface area, such as airfield and road concretes.

## **2. Material and Methods**

### **2.1. Material**

In this study, 15 cement samples were produced at 10 cm x 10 cm x 10 cm sizes using 1%, 2% and 3% (polypropylene fiber) of cement weight, keeping amount of cement constant for C 30 concrete. The chemical properties of cement, normal aggregate and polypropylene fiber used are shown in Table 1 and the chemical and physical properties of the polypropylene fiber are shown in Table 2.

Table 1 Chemical Properties of Cement, Aggregate and Polypropylene Fiber Used in Concrete Mixtures

Composition	CEM I 42.5 R (%)	Normal Aggregate (%)	Polypropylene Fiber (%)
SiO <sub>2</sub>	20.02	2.75	0.38
Fe <sub>2</sub> O <sub>3</sub>	3.52	1.29	0.06
Al <sub>2</sub> O <sub>3</sub>	5.16	-	-
CaO	63.46	0.2	53.85
MgO	1.03	2.8	0.34
SO <sub>3</sub>	2.74	-	-
Loss of ignition	2.35	-	-

Table 2 Chemical and physical properties of polypropylene fiber

Appearance	Natural White Fibers
Purity	% 100 Pure
Specific Gravity	0.91 g/cm <sup>3</sup>
Module of Elasticity	3000-3500 N/mm <sup>2</sup> (MPa)
Tensile Strength	450/700 N/mm <sup>2</sup> (MPa)
Melting Point	162 °C
Ignition Point	593 °C
Length	6mm - 12 mm - 19 mm
Profile & Diameter	Circular 18µm - 40 µm

## 2.2 Methods

Production of concrete samples, physical and mechanical properties tests were carried out in the Construction Laboratory of Civil Engineering Department of Uşak University and Mechanical Engineering Laboratory of Faculty of Engineering of Ege University. In this study, concrete was produced in 4 different mixing ratios. The amount of cement and fiber dosage was kept constant in all mixtures. Mixing ratios of the produced samples are shown in Table 3. Natural spring water was used for mixing water. The concrete mixing process was carried out with the help of a vertical axis mixer. In order to determine the consistency of the samples, slump was measured with Abrams cone. For use in various experiments, the mortar was placed in three stages, 100 mm × 100 mm × 100 mm size cube molds on vibratory table unit. At each stage, the mortar was vibrated by the vibratory table tool for 10 seconds. For each series, 15 cube samples were produced. The samples were left in mold for 24 hours. At the end of this period, the samples were removed from the mold with the aid of rubber wedges. The samples were kept in the curing pool until the day of the experiment.

Table 3 Mixture ratios of the produced samples

Mix	Cement (% wt)	Polypropylene Fiber (%)
NB	100	-
NL1	99	1
NL2	98	2
NL3	97	3

TS EN 12350-2 (2002) standard has been adopted in many countries. In this experiment also called Abrams Cone; as shown in Fig. 2, the top of a 100 mm diameter, 200 mm lower diameter and 300 mm height is cut into three equal layers into a truncated conical metal mold and each layer is freshly squeezed 25 times with a special rod (diameter 16 mm, length 600 mm) concrete filled. Then the filled concrete was pulled up through the truncated cone mold before it was vibrated. The concrete has collapsed with its own weight and the slump value was measured [15].

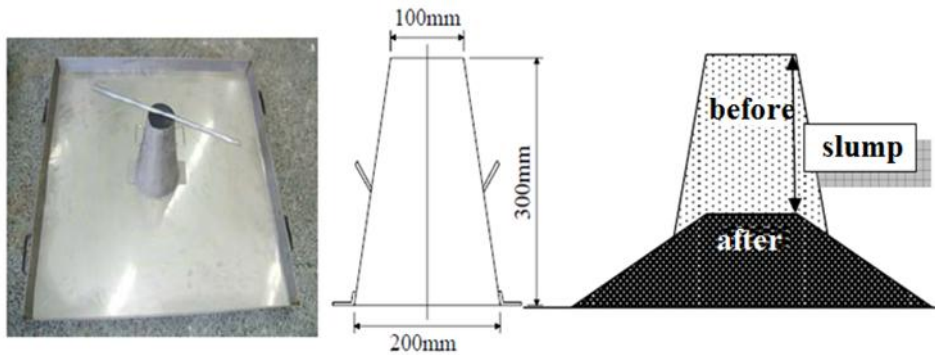


Fig 2. Tools used in the slump test and experimental procedure [7]

In the destructive test method, uniaxial pressure test and flexure test were performed. To measure ultrasonic pulse velocity, ultrasonic measuring instrument in the Construction Laboratory of Civil Engineering Department of Usak University was used (Fig. 3). The ultrasonic velocity measurement was performed with a 12-volt accumulator-equipped with a digital indicator ultrasonic measuring instrument. By spraying grease on both sides of the samples, gaps between the probes and the sample were prevented. By the experiment on the cube samples, transition time of sound waves were measured.

In evaluating ultrasound velocity test results, the ultrasonic pulse velocity time values (microsecond) were calculated in terms of km/s in ultrasonic velocity, formulated by Eq. (1);

$$V = \frac{L}{t} \quad (1)$$

where V is the ultrasonic velocity (km/s), L is sample size (km), and t is ultrasonic pulse time (s).



Fig. 3 Ultrasonic measuring instrument

In order to determine the thermal conductivity coefficient of the concrete specimens that are produced, the experiments were carried out on 80 x 40 x 10 mm samples at Mechanical Engineering Laboratory of Faculty of Engineering of Ege University (Fig. 4). When the difference between the two surface temperatures is 1 ° C under the conditions that have reached equilibrium, the amount of heat passing through "unit time, unit area and unit thickness in perpendicular direction" is the thermal conductivity of a homogeneous material. The measurement of the thermal conductivity of the structure and various thermal insulation materials are done by two methods, in steady state and transition state. The usual method is the heated plate method in steady state. The average thermal conductivity of the plate-shaped examination specimen, which is placed symmetrically on both sides of a heated plate, is found by this method. Measuring devices can detect the thermal conductivity of smaller materials in a shorter time during the transition [16].

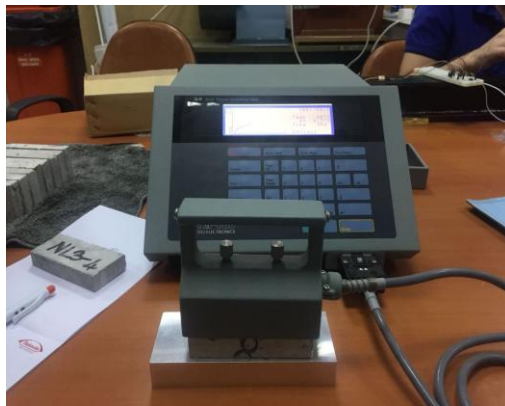


Fig. 4 Thermal conductivity measuring device

Three-point flexural test was performed in the destructive test method. For this experiment, the flexural device with 25 tons capacity was used in the Construction Laboratory of Civil Engineering Department of Usak University (Fig. 5). For this purpose, 3 of the previously prepared concrete samples were broken on the 7th day of the concrete casting and 5 of them were broken on the 28th day, and the readings at the time of breaking were used in the Eq. (2) [17]

$$f_{cf} = \frac{FL}{d_1 d_2^2} \quad (2)$$

where  $f_{cf}$  is the flexural strength (MPa),  $F$  is the maximum Load (N),  $L$  is the structural bearing effective span (mm), and  $d_1$  and  $d_2$  are the cross-sectional lengths of the sample (mm).



Fig. 5 Three-point flexural test

### 3. Result and Discussion

The results of the experiments on the concrete samples produced within the scope of this study are represented in Table 4-5. The results of the polypropylene fiber added concretes are shown in Figs. 6-12.

Table 4 Physical properties of polypropylene fiber added concrete samples

Mix	Dry Unit Weight (kg/m <sup>3</sup> )	Water Absorption (%)	Slump (mm)	Ultrasonic Velocity (km/s)	Thermal Conductivity Coefficient (W/mK)
NB	2.419	1.80	170	19.50	2.96
NL1	2.395	1.82	45	20.10	2.66
NL2	2.375	1.85	30	20.70	2.40
NL3	2.365	1.95	20	21.10	2.23

Table 5 Mechanical properties of polypropylene fiber added concrete samples

Mix	7 Days Compressive Strength (MPa)	28 Days Compressive Strength (MPa)	7 Days Flexural Strength (MPa)	28 Days Flexural Strength (MPa)
NB	40.70	49.76	7.95	9.68
NL1	38.50	45.88	7.12	9.78
NL2	38.38	45.17	7.30	10.15
NL3	38.12	44.19	7.52	10.45

### 3.1 Water Absorption Test Results

Based on standard TS EN 1097-6 the values obtained from the water absorption test results are given in the Fig. 6.

Fig. 6 shows that as the fiber dosage increases, the water absorption increases too. Notice that NL3 has the highest value but NB has the lowest value.

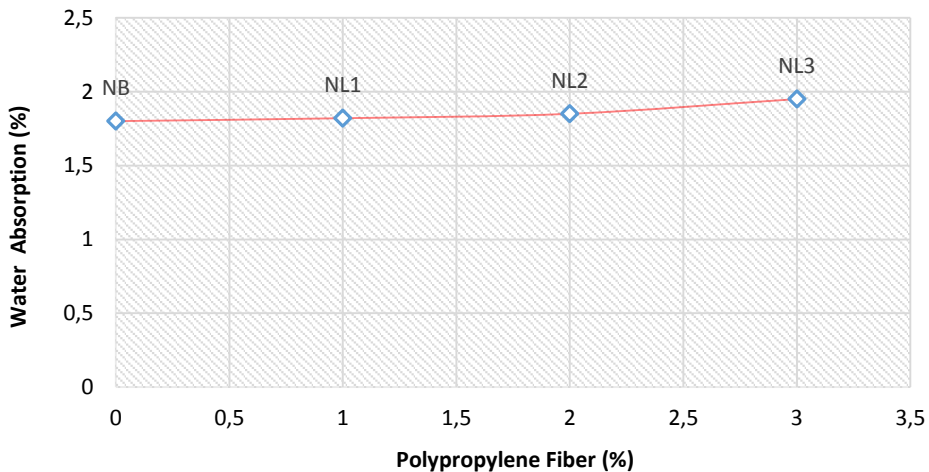


Fig. 6 Water absorption test results of polypropylene fiber added concrete samples (%)

### 3.2 Slump Test Results

Based on standard TS EN 12350-2 the values obtained from the slump test results are shown in the Fig. 7. This figure shows that as the fiber dosage increases, the slump decreases. Notice that NB has the highest value but NL3 has the lowest value.

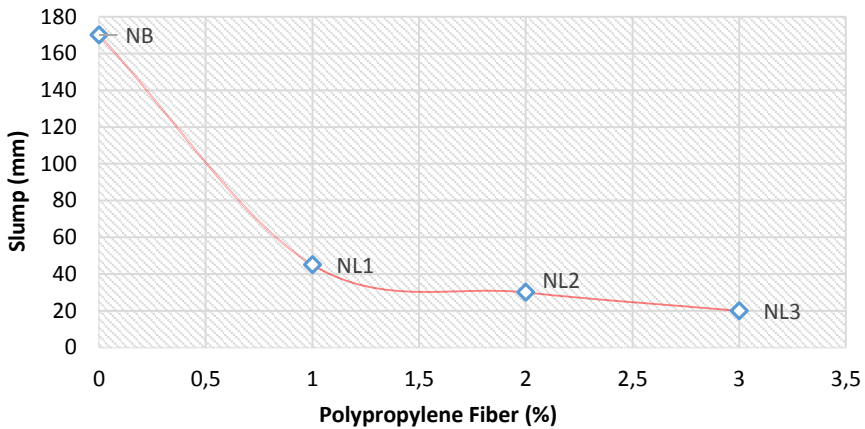


Fig. 7 Slump test results of polypropylene fiber added concrete samples (mm)

### 3.3 Ultrasonic Velocity Test Results

Based on standard TS 825 the values obtained from the ultrasonic velocity test results are represented in the Fig. 8. The results depicted at Fig. 8 show that as the fiber dosage increases,

the ultrasonic velocity increases. Notice that NL3 has the highest value but NB has the lowest value.

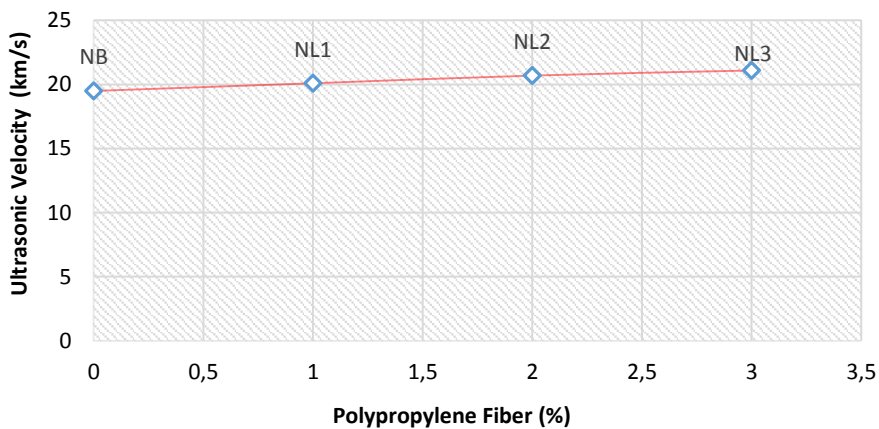


Fig. 8 Ultrasonic velocity test results of polypropylene fiber added concrete samples (km/s)

### 3.4 Compressive Strength Test Results

Based on standard TS EN 12390-4 the values obtained from the compressive strength test results are plotted in the Fig 9.

Fig. 9 shows that as the fiber dosage increases, the compressive strength decreases. Both 7 and 28 days, the highest value is NB, while the lowest value is NL3.

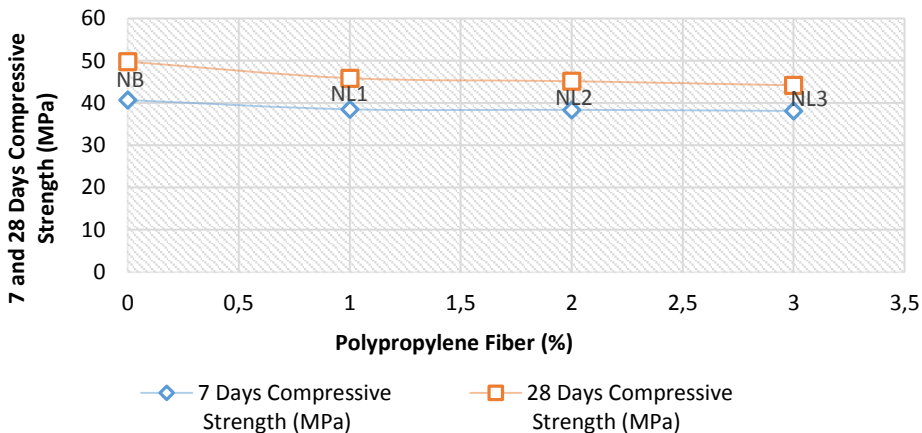


Fig. 9 7 and 28 days compressive strength test results of polypropylene fiber added concrete (MPa)

### 3.5 Flexural Strength Test Results

Based on standard TS EN 12390-4 the values obtained from the flexural strength test results are depicted in the Fig. 10.

Fig. 10 shows that as the fiber dosage increases, the flexural strength increases for 28 days, while it decreases for 7 days. For 7 days, the highest value is NB, while the lowest value is NL1. For 28 days, the highest value is NL3, while the lowest value is NB.

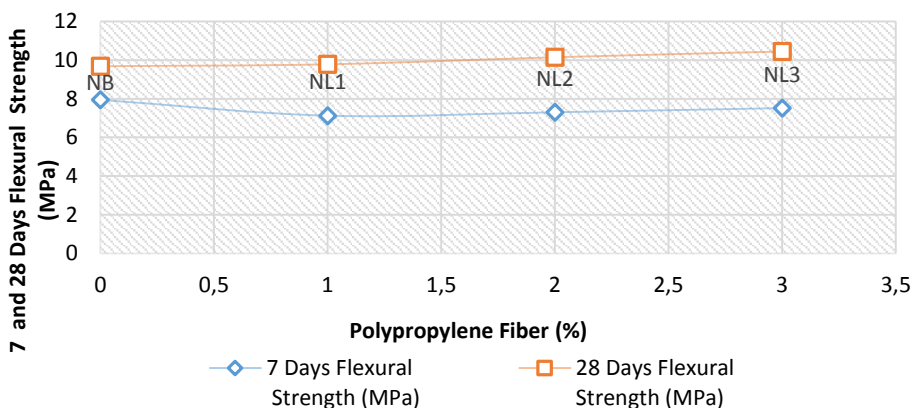


Fig. 10 7 and 28 days flexural strength test results of polypropylene fiber added concrete (MPa)

### 3.6 Thermal Conductivity Coefficient Test Results

Based on standard TS 825 the values obtained from the thermal conductivity coefficient test results are represented in the Fig. 11.

Fig. 11 shows that as the fiber dosage increases, thermal conductivity coefficient decreases. Notice that NB has the highest value, and NL3 has the lowest value.

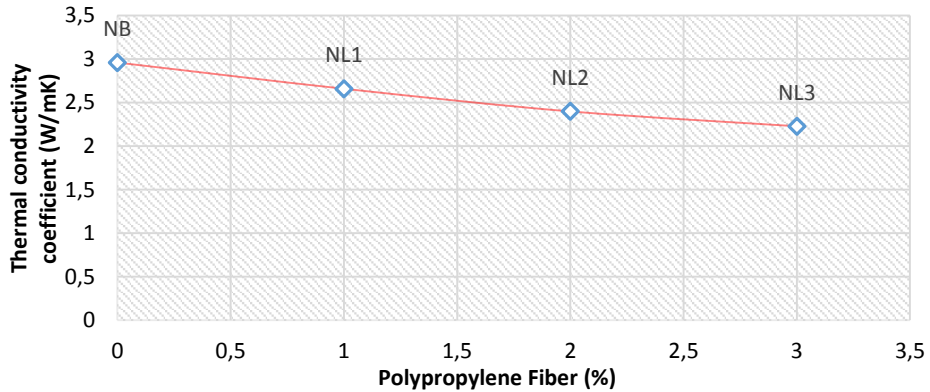


Fig. 11 Thermal conductivity coefficient test results of polypropylene fiber added concrete (W/mK)

#### 4. Conclusion

From the tests that we have performed we came to the following conclusions:

- Increasing fiber dosage in fluid concrete brings about a decrease slump. This is an important feature in terms of the cohesion of fresh concrete, even if it is seen as a negative effect on the workability.
- For 7 and 28 days compressive strength test, as the fiber ratio increased, the compressive strengths decreased by approximately 5%. However, it is observed that this decrease is within the standards of compressive strength.
- As a result of the 28 days flexural strength results, the increase in fiber ratio caused an increase in bending strength which is in agreement with Topcu et al [13] and Acikgenc et al [10].
- As the fiber dosage increased, the water absorption rate and the ultrasonic velocity increased, but the thermal conductivity coefficient decreased. It was thought that the increase of fiber dosage will contribute to thermal insulation by decreasing the thermal conductivity value.
- Generally, the use of polypropylene fiber added concretes does not technically cause a troublesome situation, but provides numerous benefits to the concrete.
- In parallel with the studies of Sumer and Saribiyik [11] it can be said that the use of polypropylene fiber added concretes can be used especially in concretes with high surface area, such as airfields and road concretes, which can provide improvement in plastic shrinkage cracks.
- Research for new types of concrete is required to satisfy the current needs in construction industry. Polypropylene fiber added to concrete will be a good substitute to meet these demands.

#### References

- [1] Sarıkaya H. Specified Concrete Production Containing Boron, Suleyman Demirel University, Institute of Science and Technology, Mining Engineering, PhD Thesis, Isparta, 2014.

- [2] Erdem E, Donat R, Cetisli H. Hydration and Mechanical Properties of Cement Containing Zeolite, 1. International Symposium on Mineral Admixtures in Cement, 6-9 November, Istanbul, Turkey. 1997; 216-220,
- [3] Neville AM. Properties of Concrete, Longman Scientific, New York, 1981; 843.
- [4] Ozel C. Determination of Rheological Properties of Additive Concrete According to Fresh Concrete Test Methods, Suleyman Demirel University, Institute of Science and Technology, Civil Engineering, PhD Thesis, Isparta, 2007
- [5] Neville, AM. Properties of Concrete, ISBN 0-582-23070-5, 3rd edition, London, 1993.
- [6] Baradan B. Building Material II, Dokuz Eylul University Faculty of Engineering Publications, İzmir, 1997.
- [7] Yardimci. MY. Investigation of Rheological, Mechanical, Refractive Parameters of Steel Fiber Self-Compacting Concrete and Optimum Design, Dokuz Eylul University, Institute of Science and Technology, PhD Thesis, Izmir, 2007.
- [8] Arazsu U. Fresh and Hardened Concrete Properties of Polypropylene Fibers, Firat University, Institute of Science and Technology, Master Thesis, 2012; 63s.
- [9] Bekaert. General Information Guide About Duomix, Belgium, 1998.
- [10] Acikgenc M, Arazsu U, Alyamac KE, Strength and Durability Properties of Polypropylene Fiber-Reinforced Concrete with Different Mixture Proportions, SDU International Journal of Technological Sciences, 2012; Vol. 4, No 3, 41-44.
- [11] Sumer B, Saribiyik M, Investigation of Polypropylene Fiber Effect to the Silica Fume Concrete, Sakarya University Journal of Science, 2013; Vol. 17, No 2, 217-224.
- [12] Salahaldeen A, Muhsen S, Influence of Polypropylene Fiber on Strength of Concrete, American Journal of Engineering Research, E-ISSN: 2320-0847 p-ISSN: 2320-0936, 2016; Vol. 5, No 7, 223-226.
- [13] Topcu IB, Demirel OE, Uygunoglu T, Physical and Mechanical Properties of Polypropylene Fiber Reinforced Mortars, Journal of Polytechnic, 2017; 20 (1), 91-96.
- [14] Sohaib N, Seemab F, Sana G, Mamoon R, Using Polypropylene Fibers in Concrete to Achieve Maximum Strength, Proc. of the Eighth International Conference on Advances in Civil and Structural Engineering, ISBN: 978-1-63248-145-0, 2018; 36-42. <https://doi.org/10.15224/978-1-63248-145-0-36>
- [15] TS EN 12350-2, Concrete - Fresh Concrete Experiments - Part 2: Slump Test, Turkish Standards Institution, Ankara, Turkey, 2002.
- [16] TS 825, Determination of Thermal Insulation in Buildings, Turkish Standards Institution, Ankara, December, 1978.
- [17] TS 310, Three Point Flexural Strength, Turkish Standards Institution, Ankara, December, 1999.



*Research Article*

## **Exact radial free vibration frequencies of a thick-walled sphere made of an isotropic and homogeneous material – A case study with a carbon nanofiller reinforced aluminum hollow sphere**

Vebil Yıldırım<sup>a</sup>

*Çukurova University Department of Mechanical Engineering, Adana, Turkey*

### **Article Info**

*Article history:*

*Received 08 June 2017*

*Revised 19 June 2018*

*Accepted 17 July 2018*

**Keywords:**

Exact free vibration,  
Natural frequency,  
Thick-walled sphere,  
Spherical Bessel's,  
Metal-matrix  
composites (MMCs)

### **Abstract**

In this study exact free vibration analysis is performed for thick-walled hollow spheres made of an isotropic and homogeneous linear elastic material. Equation of motion in terms of Lamé constants is derived from the field equations of elasticity, and then solved analytically with the help of spherical Bessel's functions. This existing solution technique is extended to several boundary conditions. For each classical boundary condition, the characteristic free vibration equation is presented in closed forms. After verifying the present results with the available literature, variation of the dimensionless natural frequencies with respect to the boundary conditions and the sphere aspect ratio (outer radius/inner radius) are examined. To show the direct use of the present results, some of which are originals, a case study for a metal-matrix composite is originally studied. This composite material is formed by a perfect dispersion of either single-walled carbon-nanotubes (SWCNT) or multi-walled carbon-nanotubes (MWCNT) within an Aluminum (AL) metal matrix so that the resulting composite is still to have both isotropy and homogeneity properties. Elastic properties of the composite are computed by using the simple mixture rule and Halpin-Tsai equations.

© 2018 MIM Research Group. All rights reserved

## **1. Introduction**

Vibration of thick-walled spheres is of great importance in many engineering applications. Pioneering studies date back 1880s [1-2]. As easily guessed, in the first works in this realm, spheres are assumed to be made of traditional materials having both isotropy and homogeneity properties [3-9]. Among those, Sato and Usami [3-4] presented a basic study on the oscillation of homogeneous elastic sphere. Shah et al. [5-6] examined analytically and numerically the elastic waves in a hollow sphere based on the three dimensional shell theory. Seide [7] derived the frequency equation in radial direction for hollow thin spheres. Fixed boundary conditions for the free vibration analysis of elastic spheres were studied by Scafbuch et. al. [8]. Gosh and Agrawal [9] worked analytically on the free and forced radial vibrations of spheres by employing Bessel's functions as in the present study. Explicit expressions were presented for the natural frequencies and dynamic stresses for various time-varying internal pressures in Gosh and Agrawal' work [9]. Abbas [10] presented an analytical solution for the free vibration of a thermo-elastic hollow sphere.

\*Corresponding author: [vebil@cu.edu.tr](mailto:vebil@cu.edu.tr)

<sup>a</sup>orcid.org/ 0000-0001-9955-8423

DOI: <http://dx.doi.org/10.17515/resm2017.24me0608>

Res. Eng. Struct. Mat. Vol. 5 Iss. 1 (2019) 13-32

Sharma and Sharma [11] and Sharma [12] also studied free vibration of thermoelastic solid and hollow spheres, respectively.

Numerous studies have been continued up to now by employing advanced materials with thermal, magnetic and whatnot effects. Among them, vibration analysis of spheres made of anisotropic materials occupy a great deal of space in the open literature [13-29]. Eason [14] firstly examined the pure radial free vibration of transversely isotropic spheres. Grigorenko and Kilina [18] handled 2-D and 3-D formulation of the problem at stake. Jiang et al. [20] investigated free vibration of layered hollow spheres using three-dimensional elasticity. After Eason [14], Stavsky and Greenberg [26], Ding and Wang [27], and Keles [29] have addressed purely radial free vibrations for anisotropic spheres. Chen et al. [30] dealt with free vibrations of a piezoceramic fluid-filled hollow sphere. Chiroiu and Munteanu [31] omitted fluid effects on the free vibration of a piezoceramic sphere. Lately free vibrations of spheres made of functionally graded materials have been gained an attention [32-38].

This study deals with only purely radial free vibration of hollow spheres made of both isotropic and homogeneous material. The principal aim of the present study is to present a detailed source for engineers and young scientists. To this end, as a very fundamental problem, the exact free vibration analysis of a thick-walled hollow sphere with the inner radius  $a$  and the outer radius  $b$  have been reconsidered (Fig. 1) [9]. The ratio  $(b/a)$  is defined as an aspect ratio of the sphere. When doing this, the solution method proposed by Gosh and Agarwal [9] are step-by-step extended to additional boundary conditions. The effects of the aspect ratio on the exact dimensionless radial natural frequencies are also examined. These results, some of which are original, may also be served as a comparison means. Those natural frequencies may also be used directly to study the exact dynamic response of such structures as in References [9, 36].

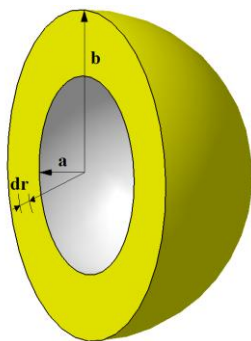


Fig. 1 Geometry of a sphere

Besides, to consider a kind of emerging state of the art technological materials [39-41], a very simple example, which may be solved by direct application of the present formulation to the free vibration of a hollow sphere made of a carbon nanotube reinforced metal, is to be examined.

It is also worth noting that the present formulation may easily be extended to the radial free vibration of spheres, cylinders, or disks made of either ordinary orthotropic or functionally graded materials as in References [36, 38, 42-43].

## 2. Formulation

The strain-displacement relations under axisymmetric conditions are given in spherical coordinates,  $(r, \theta, \phi)$ , by (Fig. 1)

$$\begin{aligned}\varepsilon_r &= \frac{du_r}{dr} \\ \varepsilon_\theta &= \varepsilon_\phi = \frac{u_r}{r}\end{aligned}\tag{1}$$

where  $\varepsilon_r$  is the radial unit strain,  $\varepsilon_\theta$  is the tangential unit strain and  $u_r$  is the radial displacement. Denoting the radial stress by  $\sigma_r$ , and the hoop stress by  $\sigma_\theta$ , Hooke's law for spheres is written as follows

$$\begin{aligned}\sigma_r &= C_{11} \varepsilon_r + C_{12} \varepsilon_\theta \\ \sigma_\theta &= C_{21} \varepsilon_r + C_{22} \varepsilon_\theta\end{aligned}\tag{2}$$

where the stiffness terms may be defined by Lamé's constants for an isotropic and homogeneous linear elastic material as

$$\begin{aligned}C_{11} &= \lambda + 2\mu \quad ; C_{12} = 2\lambda \\ C_{21} &= \lambda \quad ; C_{22} = 2\lambda + 2\mu\end{aligned}\tag{3}$$

Representing Poisson's ratio by  $\nu$ , and elasticity modulus by  $E$ , Lamé's constants are defined as

$$\begin{aligned}\lambda &= \frac{\nu E}{(1 + \nu)(1 - 2\nu)} \\ \mu &= \frac{E}{2(1 + \nu)}\end{aligned}\tag{4}$$

In the absence of the body forces, equation of motion in the radial direction is given by

$$\frac{1}{r^2} \frac{\partial}{\partial r} (r^2 \sigma_r) - \frac{2\sigma_\theta}{r} = \frac{\partial \sigma_r}{\partial r} + \frac{2(\sigma_r - \sigma_\theta)}{r} = \rho \frac{\partial^2 u_r}{\partial t^2}\tag{5}$$

where  $\rho$  is the material density and  $t$  is the time. Substituting strain-displacement relations and Hooke's law in the equation of motion, and taking the first derivative of the radial stress with respect to the radial coordinate we obtain

$$\frac{\partial^2 u_r}{\partial r^2} + \frac{2}{r} \frac{\partial u_r}{\partial r} - \frac{2}{r^2} u_r = \frac{\rho}{C_{11}} \frac{\partial^2 u_r}{\partial t^2}\tag{6}$$

By assuming the following harmonic motion with an angular velocity  $\omega$  (rad/s)

$$u_r(r,t) = u_r^*(r) e^{i\omega t} \tag{7}$$

Eq. (6) turns into Bessel's differential equations as follows [44-47]

$$\left(-\frac{2}{r^2} + \frac{\rho}{\lambda + 2\mu} \omega^2\right) u_r^* + \frac{2}{r} \frac{du_r^*}{dr} + \frac{d^2 u_r^*}{dr^2} = 0 \tag{8}$$

The solutions to this equation will be in terms of the first and second kinds spherical Bessel's functions,  $j_n(x)$  and  $y_n(x)$  [44-47].

$$u_r^*(r) = C_1 j_1(r\Omega) + C_2 y_1(r\Omega) \tag{9}$$

where

$$\Omega^2 = \frac{\rho}{\lambda + 2\mu} \omega^2 \tag{10}$$

The first derivative of the solution of the radial displacement,  $u_r^*$ , and the radial stress,  $\sigma_r^*$ , may be obtained in terms of integration constants,  $C_1$  and  $C_2$ , as follows [44-47]

$$\begin{aligned} \frac{du_r^*}{dr} = & C_1 \Omega \left( \frac{1}{2} (j_0(r\Omega) - j_2(r\Omega)) - \frac{j_1(r\Omega)}{2r\Omega} \right) \\ & + C_2 \Omega \left( \frac{1}{2} (y_0(r\Omega) - y_2(r\Omega)) - \frac{y_1(r\Omega)}{2r\Omega} \right) \end{aligned} \tag{11}$$

$$\begin{aligned} \sigma_r^* = & \frac{1}{r^3 \Omega^2} \left( \sin(r\Omega) (-4C_1 \mu + C_1 r^2 \Omega^2 (\lambda + 2\mu) + 4C_2 \mu r \Omega) \right. \\ & \left. + \cos(r\Omega) (4C_1 \mu r \Omega + 4C_2 \mu - C_2 r^2 \Omega^2 (\lambda + 2\mu)) \right) \end{aligned}$$

Boundary conditions considered in this study is presented in Table 1. If one applies these constraints, the following may be obtained for free-free ends.

$$\mathbf{A}_{Free-Free} \begin{Bmatrix} C_1 \\ C_2 \end{Bmatrix} = \begin{bmatrix} a_{11} & a_{12} \\ a_{21} & a_{22} \end{bmatrix} \begin{Bmatrix} C_1 \\ C_2 \end{Bmatrix} = \begin{Bmatrix} 0 \\ 0 \end{Bmatrix} \tag{12}$$

In the above

$$\begin{aligned} a_{11} = & \frac{a^2 \lambda \sin(a\Omega) \Omega^2 + 2a^2 \mu \sin(a\Omega) \Omega^2 + 4a\mu \cos(a\Omega) \Omega - 4\mu \sin(a\Omega)}{a^3 \Omega^2} \\ a_{12} = & \frac{-a^2 \lambda \cos(a\Omega) \Omega^2 - 2a^2 \mu \cos(a\Omega) \Omega^2 + 4a\mu \sin(a\Omega) \Omega + 4\mu \cos(a\Omega)}{a^3 \Omega^2} \\ a_{21} = & \frac{b^2 \lambda \sin(b\Omega) \Omega^2 + 2b^2 \mu \sin(b\Omega) \Omega^2 + 4b\mu \cos(b\Omega) \Omega - 4\mu \sin(b\Omega)}{b^3 \Omega^2} \\ a_{22} = & \frac{-b^2 \lambda \cos(b\Omega) \Omega^2 - 2b^2 \mu \cos(b\Omega) \Omega^2 + 4b\mu \sin(b\Omega) \Omega + 4\mu \cos(b\Omega)}{b^3 \Omega^2} \end{aligned} \tag{13}$$

For non-trivial natural frequencies, the determinant of  $\mathbf{A}_{Free-Free}$  must be equal to zero. This is called characteristic equation. For boundary conditions given in Table 1, characteristic equations for different boundary conditions are found as follows

$$\begin{aligned}
 |\mathbf{A}_{Free-Free}| &= 4\mu\Omega(a-b)\cos(\Omega(a-b))(ab\Omega^2(\lambda+2\mu)+4\mu) \\
 &\quad - \sin(\Omega(a-b))(a^2b^2\Omega^4(\lambda+2\mu)^2 \\
 &\quad - 4\mu\Omega^2(\lambda(a^2+b^2)+2\mu(a-b)^2)+16\mu^2) = 0
 \end{aligned}
 \tag{14a}$$

$$\begin{aligned}
 |\mathbf{A}_{Fixed-Free}| &= j_1(a\Omega)(4b\mu\Omega\sin(b\Omega) - \cos(b\Omega)(b^2\Omega^2(\lambda+2\mu) - 4\mu)) \\
 &\quad + y_1(a\Omega)(-\sin(b\Omega)(b^2\Omega^2(\lambda+2\mu) - 4\mu) \\
 &\quad - 4b\mu\Omega\cos(b\Omega)) = 0
 \end{aligned}$$

$$\begin{aligned}
 |\mathbf{A}_{Free-Fixed}| &= j_1(b\Omega)(\cos(a\Omega)(a^2\Omega^2(\lambda+2\mu) - 4\mu) - 4a\mu\Omega\sin(a\Omega)) \\
 &\quad + y_1(b\Omega)(\sin(a\Omega)(a^2\Omega^2(\lambda+2\mu) - 4\mu) \\
 &\quad + 4a\mu\Omega\cos(a\Omega)) = 0
 \end{aligned}
 \tag{14b}$$

$$|\mathbf{A}_{Fixed-Fixed}| = j_1(a\Omega)y_1(b\Omega) - y_1(a\Omega)j_1(b\Omega) = 0$$

Table 1 Boundary conditions considered in this study.

	Free-Free	Fixed-Free	Fixed-Fixed	Free-Fixed
at ( $r = a$ )	$\sigma_r^*(a) = 0$	$u_r^*(a) = 0$	$u_r^*(a) = 0$	$\sigma_r^*(a) = 0$
at ( $r = b$ )	$\sigma_r^*(b) = 0$	$\sigma_r^*(b) = 0$	$u_r^*(b) = 0$	$u_r^*(b) = 0$

Defining the dimensionless natural frequency as follows

$$\beta = \frac{a}{\sqrt{\frac{c_{11}}{\rho}}} \omega
 \tag{15}$$

variation of the determinants of the characteristic equation given in Eq. (14) with the dimensionless natural frequencies for different boundary conditions and aspect ratio of ( $b/a=1.02$ ) is graphically illustrated in Fig. 2. As seen from the graphs, dimensionless natural frequencies make the determinant zero. There are various numerical methods to find the roots of Eq. (14).

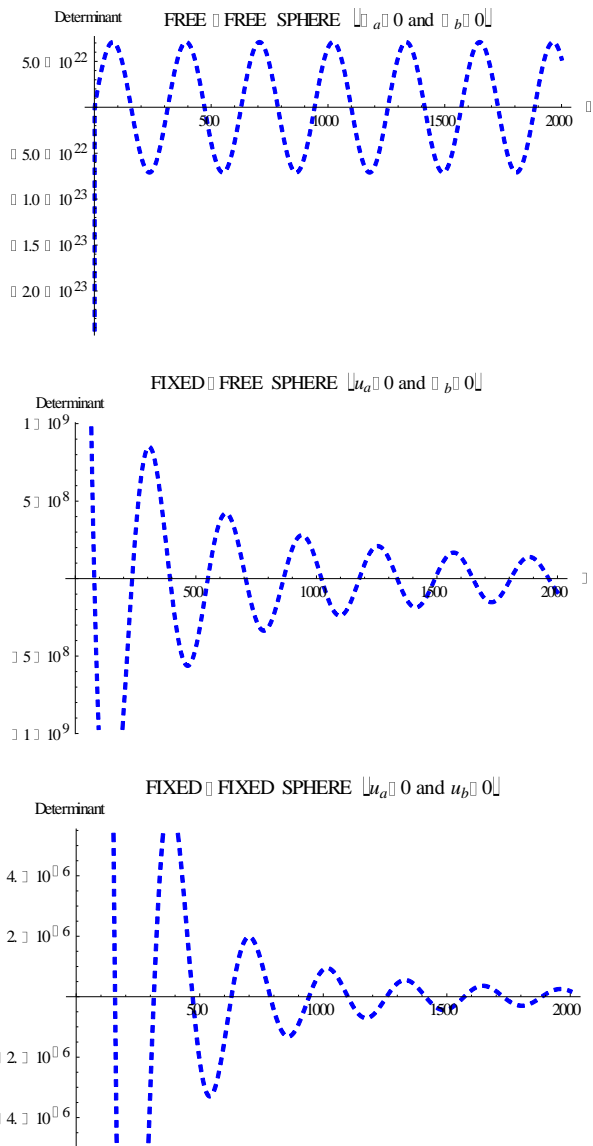


Fig. 2 Variation of the determinants of the characteristic equation given in (14) with the dimensionless natural frequencies for different boundary conditions and aspect ratio of ( $b/a=1.02$ ).

### 3. Verification of the Results

The present dimensionless results obtained with Eq. (14) are compared with the literature for free-free ends and the aspect ratio of 2 in Table 2. A good agreement is observed between the results.

Table 2 Comparisons of the present natural frequencies with the literature for free-free ends,  $\nu = 0.3$ , and  $b/a = 2$

$\beta_i$	Present	[36]	[37]
1	1.01034	1.01178	0.9781990865
2	3.33252	3.33527	3.296902510
3	6.37556	6.37694	6.358013920
4	9.48585	9.48676	9.474240635
5	12.612	12.61272	12.60335232
6	15.7444	15.74499	15.73750534
7	18.8799	18.88038	18.87415459
8	22.0172	22.01756	22.01222291
9	25.1555	25.15584	25.15117544
10	28.2946	28.29486	28.29071630

### 4. Variation of the Natural Frequencies with the Aspect Ratios and Boundary Conditions

Variation of the natural frequencies with the boundary conditions are presented for  $\nu = 0.3$ , and  $b/a = 1.02$  in a comparative manner in Table 3. The first twelve dimensionless natural frequencies are given in this table.

Table 3 Variation of the natural frequencies with the boundary conditions for  $b/a = 1.02$  and  $\nu = 0.3$

$\beta_i$	Free-Free	Fixed-Free	Fixed-Fixed	Free-Fixed
1	1.4425	78.4629	157.086	78.6432
2	157.087	235.594	314.162	235.654
3	314.163	392.684	471.241	392.72
4	471.241	549.768	628.32	549.793
5	628.32	706.85	785.399	706.87
6	785.4	863.931	942.479	863.947
7	942.479	1021.01	1099.56	1021.03
8	1099.56	1178.09	1256.64	1178.1
9	1256.64	1335.17	1413.72	1335.18
10	1413.72	1492.25	1570.8	1492.26
11	1570.8	1649.33	1727.88	1649.34
12	1727.88	1806.41	1884.96	1806.42

As expected, Table 3 suggests that increasing the total number of the degrees of freedom at both ends decreases significantly the frequencies. This is the most noticeable characteristic among the fundamental frequencies. That is, while  $\beta_1 = 1.4425$  for free-free ends, it reaches  $\beta_1 = 157.086$  for fixed-fixed ends.

Variation of the first twelve natural frequencies with aspect ratios from  $b/a = 1.03$  through  $b/a = 2$  for all boundary conditions and  $\nu = 0.3$  is presented in Table 4 in tabular form.

Table 4. Variation of the first twelve natural frequencies with aspect ratios and boundary conditions for  $\nu = 0.3$

$\beta_i$	$b/a$								
	1.03	1.04	1.05	1.075	1.10	1.25	1.50	1.75	2.00
FREE-FREE									
1				1.4049					1.0103
	1.43546	1.42852	1.42167	5	1.38876	1.30140	1.18376	1.08938	4
2				41.913					3.3325
	104.73	78.5538	62.8492	3	31.449	12.6395	6.40647	4.34971	2
3				83.788					6.3755
	209.445	157.087	125.672	5	62.8484	25.1692	12.6273	8.45626	6
4				125.67					9.4858
	314.163	235.624	188.501	2	94.2588	37.7234	18.8901	12.6186	5
5				167.55					
	418.882	314.163	251.332	8	125.672	50.2837	25.1631	16.7942	12.612
6				209.44					15.744
	523.601	392.702	314.163	5	157.086	62.8464	31.4402	20.9752	4
7				251.33					18.879
	628.32	471.241	376.994	2	188.501	75.4104	37.7193	25.1588	9
8				293.21					22.017
	733.04	549.781	439.825	9	219.916	87.975	43.9996	29.3438	2
9				335.10					25.155
	837.759	628.32	502.657	6	251.332	100.54	50.2806	33.5298	5
10				376.99					28.294
	942.479	706.86	565.489	4	282.747	113.105	56.5621	37.7164	6
11				418.88					31.434
	1047.2	785.4	628.32	2	314.163	125.671	62.844	41.9035	1
12				460.76					34.574
	1151.92	863.939	691.152	9	345.578	138.237	69.1261	46.0909	1
FIXED-FIXED									
1				41.910					3.2860
	104.729	78.5521	62.847	1	31.4448	12.6294	6.38581	4.31683	1
2				83.786					6.3606
	209.444	157.086	125.671	9	62.8463	25.1645	12.619	8.44465	8
3				125.67					
	314.162	235.624	188.501	1	94.2574	37.7203	18.8848	12.6115	9.4772
4				167.55					12.605
	418.881	314.162	251.331	7	125.671	50.2814	25.1592	16.7891	9
5				209.44					15.739
	523.601	392.702	314.162	4	157.085	62.8446	31.4371	20.9712	7
6				251.33					
	628.32	471.241	376.994	1	188.5	75.4088	37.7168	25.1554	18.876
7				293.21					22.013
	733.04	549.78	439.825	8	219.916	87.9737	43.9974	29.341	8
8				335.10					25.152
	837.759	628.32	502.657	6	251.331	100.539	50.2787	33.5274	6
9				376.99					
	942.479	706.86	565.488	4	282.747	113.104	56.5605	37.7143	28.292
10				418.88					31.431
	1047.2	785.399	628.32	1	314.162	125.67	62.8425	41.9015	8
11				460.76					
	1151.92	863.939	691.152	9	345.578	138.236	69.1247	46.0891	34.572
12				502.65					37.712
	1256.64	942.479	753.983	7	376.994	150.802	75.4071	50.2768	4
FREE-FIXED									
1									2.0004
	52.4694	39.3855	31.5374	21.08	15.858	6.50815	3.46102	2.47932	2

2	157.116	117.848	94.2882	62.877	47.1735	18.9226	9.52685	6.40655	4.8523
3	261.821	196.373	157.104	104.74	78.5696	31.4596	15.7688	10.5452	7.9366
4	366.535	274.906	219.929	146.62	109.977	44.0135	22.0345	14.7129	11.054
5	471.251	353.442	282.757	188.51	141.388	56.5729	28.3081	18.8901	14.182
6	575.969	431.979	345.586	230.39	172.801	69.1349	34.5851	23.0715	17.316
7	680.687	510.518	408.416	272.28	204.215	81.6982	40.864	27.2551	20.451
8	785.405	589.056	471.247	314.16	235.629	94.2623	47.1441	31.4402	23.589
9	890.124	667.595	534.078	356.05	267.044	106.827	53.4249	35.6261	26.727
10	994.843	746.134	596.909	397.94	298.459	119.392	59.7062	39.8127	29.866
11	1099.56	824.674	659.74	439.82	329.874	131.957	65.9879	43.9996	33.006
12	1204.28	903.213	722.572	481.71	361.29	144.523	72.2698	48.1869	36.146
<b>FIXED-FREE</b>									
1	52.2898	39.2064	31.3589	20.902	15.6807	6.32563	3.25556	2.24722	1.7444
2	157.056	117.789	94.229	62.818	47.1155	18.8673	9.4737	6.3535	4.7978
3	261.785	196.337	157.068	104.71	78.5348	31.4267	15.7379	10.5154	7.9073
4	366.509	274.88	219.903	146.60	109.952	43.9901	22.0127	14.692	11.034
5	471.231	353.422	282.737	188.49	141.369	56.5547	28.2911	18.874	14.167
6	575.952	431.963	345.57	230.38	172.785	69.12	34.5713	23.0584	17.303
7	680.673	510.504	408.403	272.26	204.202	81.6856	40.8523	27.2441	20.441
8	785.394	589.044	471.235	314.15	235.618	94.2514	47.134	31.4306	23.580
9	890.114	667.585	534.067	356.04	267.034	106.817	53.416	35.6177	26.719
10	994.834	746.125	596.90	397.93	298.45	119.383	59.6982	39.8051	29.859
11	1099.55	824.665	659.732	439.82	329.866	131.949	65.9807	43.9928	32.999
12	1204.27	903.205	722.564	481.70	361.282	144.516	72.2632	48.1807	36.140

Variation of the first six natural frequencies of free-free sphere is also illustrated graphically in Figs. 3-5.

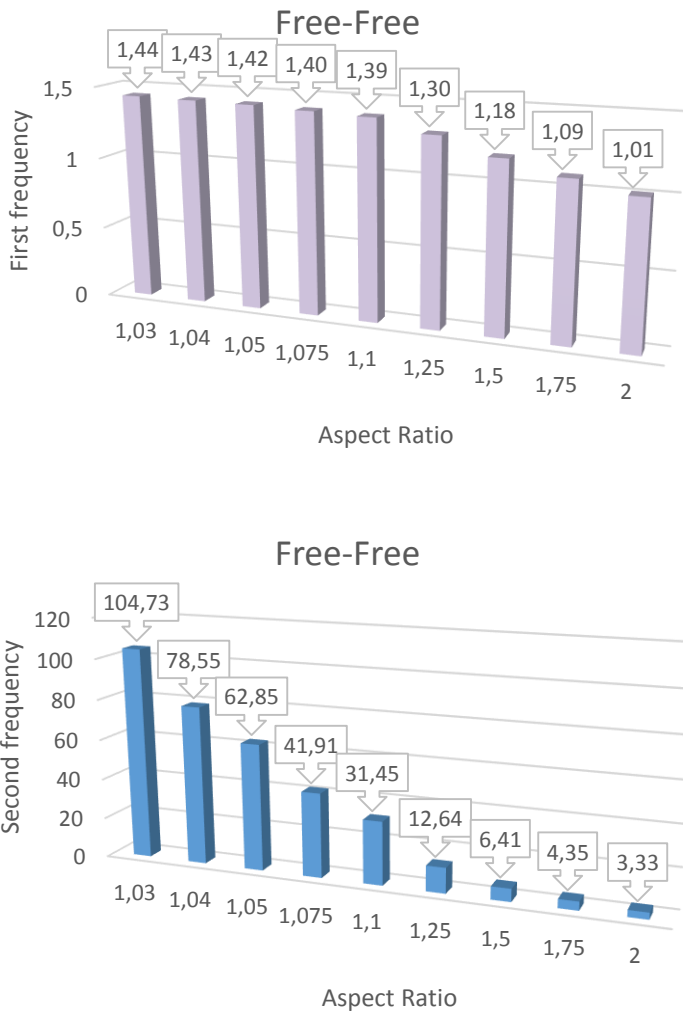


Fig. 3 Variation of the first and second natural frequencies of the sphere with the aspect ratios ( $\nu = 0.3$ )

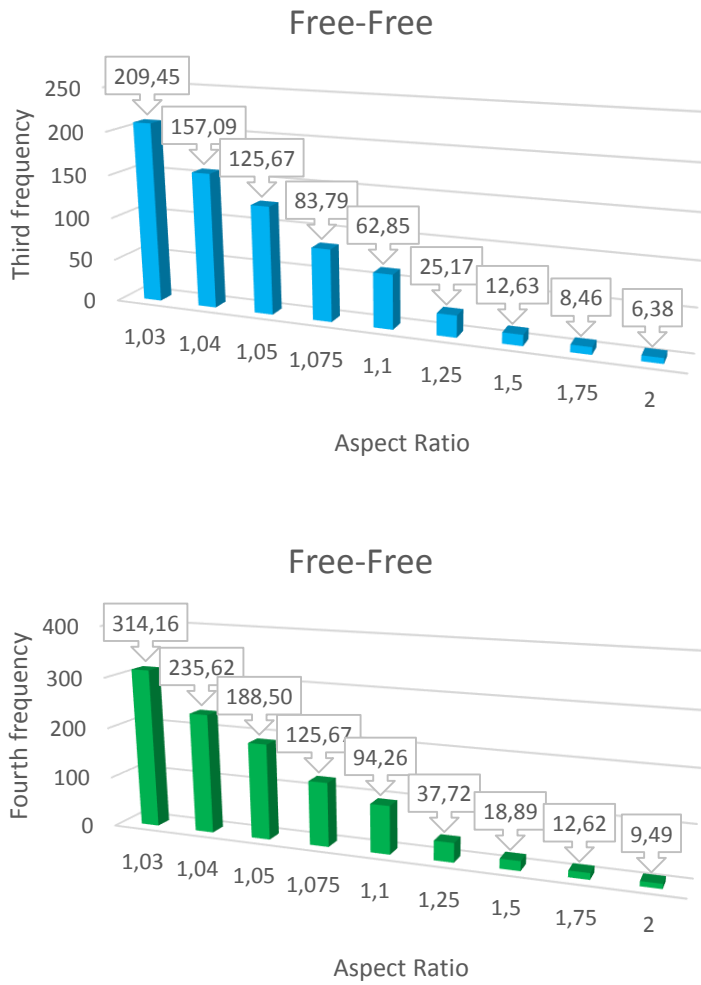


Fig. 4 Variation of the third and fourth natural frequencies of the sphere with the aspect ratios ( $\nu = 0.3$ )



Fig. 5 Variation of the fifth and sixth natural frequencies of the sphere with the aspect ratios. ( $\nu = 0.3$ )

From Table 4 and Figs. 3 and 4, it is seen that when the thickness of the sphere increases, the dimensionless natural frequencies become smaller. Higher dimensionless natural frequencies are observed for thin-walled spheres. There are minor differences in frequencies under fixed-free and free-fixed boundary conditions. Natural frequencies of the sphere with fixed-free surfaces are slightly lesser than the one with free-fixed boundaries.

### 5. Case Study

Today's works have focused on research to further improve composite material properties. Metal-matrix composites (MMCs) is a group of advanced materials. The interest in carbon nanotubes (CNTs) as reinforcements for aluminium (Al) has been growing considerably. Neubauer et al. [41] presented an overview and summarized the activities related to carbon nanotubes and nanofibers used as a reinforcement in metallic matrix materials. They also discussed the main challenges and the potential with respect to material properties.

In this section, a case study with a hollow sphere made of a metal-matrix composite is to be originally conducted to show the direct application of the present results. The composite material is formed by the perfect uniform dispersion of carbon nanotubes (CNTs) into Aluminium (Al) metal matrix. Two types of CNTs are considered, namely single-walled carbon-nanotubes (SWCNT) and multi-walled carbon-nanotubes (MWCNT). To get a homogeneous and isotropic composite material, up to 5 wt.%CNT is dispersed in Al matrix. Otherwise, the resulting composite is to show anisotropic material characteristics. CNT properties have been taken from Costa et al.'s study [48]: Material properties of a metallic matrix are

$$E_m = E_{Al} = 70 \text{ GPa}, \quad \nu_m = \nu_{Al} = 0.3, \quad \rho_m = \rho_{Al} = 2700 \text{ k/m}^3$$

Material and geometrical properties of SWCNTs are [48]

$$E_{SWCNT} = 640 \text{ GPa}, \quad \nu_{SWCNT} = 0.33, \quad \rho_{SWCNT} = 1350 \text{ k/m}^3$$

$$l_{SWCNT} = 25 (\mu\text{m}), \quad d_{SWCNT} = 1.4(\text{nm}), \quad t_{SWCNT} = 0.34(\text{nm})$$

Material and geometrical properties of MWCNTs are [48]

$$E_{MWCNT} = 400 \text{ GPa}, \quad \nu_{MWCNT} = 0.33, \quad \rho_{MWCNT} = 1350 \text{ k/m}^3$$

$$l_{MWCNT} = 50 (\mu\text{m}), \quad d_{MWCNT} = 20(\text{nm}), \quad t_{MWCNT} = 0.34(\text{nm})$$

In the above  $d$ ,  $t$ , and  $l$  are the diameter, thickness, and length of a CNT, respectively. Poisson's ratio and the density of the resulting composite are computed by using a simple mixture rule as follows

where  $V_{CNT}$  denotes the volume fraction of CNTs and it is calculated by using CNTs weight fraction,  $w_{CNT}$ .

$$V_{CNT} = \frac{w_{CNT}}{w_{CNT} + \left(\frac{\rho_{CNT}}{\rho_m}\right) - \left(\frac{\rho_{CNT}}{\rho_m}\right)w_{CNT}} \tag{17}$$

It may be noted that both the length efficiency and the orientation efficiency factors are taken as unit in Eq. (16) due to the present assumptions. Young's modulus of the composite is to be estimated through Halpin-Tsai equations [48-49].

$$E_{m-CNT} = \frac{E_m}{8} \left( 5 \left( \frac{1 + 2\beta_{dd}V_{CNT}}{1 - \beta_{dd}V_{CNT}} \right) + 3 \left( \frac{1 + 2 \left( \frac{l_{CNT}}{d_{CNT}} \right) \beta_{dl}V_{CNT}}{1 - \beta_{dl}V_{CNT}} \right) \right) \tag{18}$$

where

$$\beta_{dl} = \frac{\left(\frac{E_{CNT}}{E_m}\right) - \left(\frac{d_{CNT}}{4t_{CNT}}\right)}{\left(\frac{E_{CNT}}{E_m}\right) + \left(\frac{l_{CNT}}{2t_{CNT}}\right)}, \quad \beta_{dd} = \frac{\left(\frac{E_{CNT}}{E_m}\right) - \left(\frac{d_{CNT}}{4t_{CNT}}\right)}{\left(\frac{E_{CNT}}{E_m}\right) + \left(\frac{d_{CNT}}{2t_{CNT}}\right)} \quad (19)$$

Variation of the effective properties of the composite with CNTs weight fraction up to 5 wt.%CNT is seen in Fig. 6. As can be seen from the figure that Poisson’s ratio of the composite formed either SWCNT or MWCNT increase with increasing weight fraction while the density of the composite decrease with increasing weight fraction. It is revealed that both SWCNT and MWCNT make the same difference in values of Poisson’s ratio and the density. However, there is a significant difference in the values of Young’s modulus. When SWCNTs enhance elasticity modulus of the composite with increasing weight fractions, MWCNTs make the opposite.

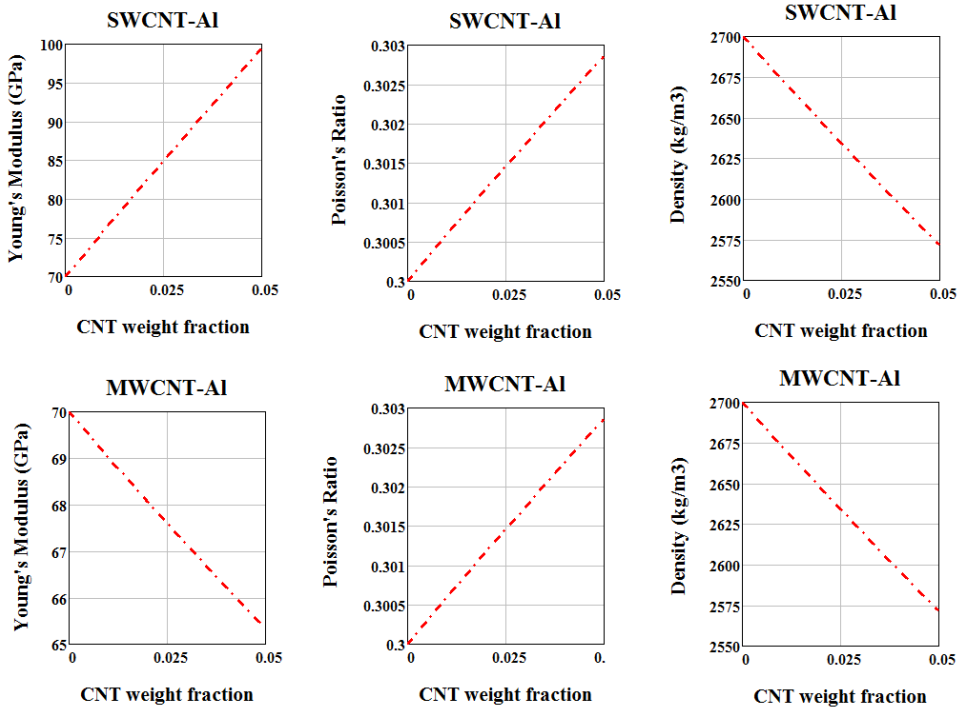


Fig. 6 Variation of the effective properties of the composite with CNTs weight fraction

In the present study three numerical values of CNTs weight fraction are chosen. Material properties of the resulting composite are tabulated in Table 5 with respect to the chosen CNTs weight fraction values.

Table 5. Material properties of the resulting composite

$w_{SWCNT}$	$E_{m-SWCNT}$ (GPa)	$\nu_{m-SWCNT}$	$\rho_{m-SWCNT}$ (kg/m <sup>3</sup> )
0.0	70.0	0.3	2700
0.01	76.01	0.301	2673
0.025	84.9	0.301	2634
0.05	99.42	0.303	2571
$w_{MWCNT}$	$E_{m-MWCNT}$ (GPa)	$\nu_{m-MWCNT}$	$\rho_{m-MWCNT}$ (kg/m <sup>3</sup> )
0.0	70.0	0.3	2700
0.01	69.02	0.301	2673
0.025	67.60	0.301	2634
0.05	65.35	0.303	2571

Let's write the dimensionless natural frequency in Eq. (15) in a more explicit form as follows

$$\beta = \frac{a}{\sqrt{\frac{c_{11}}{\rho}}} \omega = \frac{a}{\sqrt{\frac{\lambda+2\mu}{\rho}}} \omega = \frac{a}{\sqrt{\frac{E(1-\nu)}{\rho(1+\nu)(1-2\nu)}}} \omega \tag{20}$$

The relationship between the natural frequencies and the ratio of ( $\beta/a$ ) are presented in Table 6. Table 6 also comprises the percentage relative increase/decrease compared to a sphere made of a pure aluminum.

Table 6. Natural frequencies in terms of ( $\beta/a$ )

$w_{SWCNT}$	$\omega$ (rad/s)	$\omega$ (kHz)	$\left  \frac{\omega_m - \omega_{m-SWCNT}}{\omega_m} \right  100$
0.0	5907.646308( $\beta/a$ )	0.940231( $\beta/a$ )	0
0.01	6191.731479( $\beta/a$ )	0.985445( $\beta/a$ )	4.81
0.025	6600.404350( $\beta/a$ )	1.050487( $\beta/a$ )	11.73
0.05	7243.810673( $\beta/a$ )	1.152888( $\beta/a$ )	22.62
$w_{MWCNT}$	$\omega$ (rad/s)	$\omega$ (kHz)	$\left  \frac{\omega_m - \omega_{m-MWCNT}}{\omega_m} \right  100$
0.0	5907.646308( $\beta/a$ )	0.939067( $\beta/a$ )	0
0.01	5900.334574( $\beta/a$ )	0.937371( $\beta/a$ )	0.12
0.025	5889.673752( $\beta/a$ )	0.934663( $\beta/a$ )	0.30
0.05	5872.658190( $\beta/a$ )	0.939067( $\beta/a$ )	0.59

It can be seen from Table 6 that 1wt.%SWCNT dispersion escalates the natural frequencies by approximately 5%, 2.5wt.%SWCNT dispersion makes an increase approximately 12%, and 5 wt.%SWCNT dispersion buildups the frequencies by approximately 23%. MWCNT dispersion into Al matrix makes almost no significant differences in natural frequencies. In other words, approximately the same natural frequencies may be obtained by dispersing MWCNT into Al matrix by obtaining 5% lighter material. SWCNT inclusion into Al matrix affects both the weight of the material and natural frequencies. In the design and optimization of the structures, it is requested to have larger natural frequencies for the same weight of structure.

As a numerical example let's consider a hollow sphere made of either a steel or an aluminium. For this materials, the wave velocity having been a wave property may be computed numerically as

$$\left( \sqrt{\frac{\lambda + 2\mu}{\rho}} \right)_{Steel} = 5875.097045 \text{ m/s } (E = 200GPa, \rho = 7800 \text{ kg/m}^3, \nu = 0.3)$$

$$\left( \sqrt{\frac{\lambda + 2\mu}{\rho}} \right)_{Aluminium} = 5907.646308 \text{ m/s } (E = 70GPa, \rho = 2700 \text{ kg/m}^3, \nu = 0.3)$$

From Eq. (20) the following is obtained for the natural frequency in kHz.

$$\omega = \sqrt{\frac{\lambda + 2\mu}{\rho}} \frac{(\beta/a)}{2\pi} \frac{1}{1000} \text{ (kHz)}$$

Let's assume  $a = 1\text{cm}$  and  $b = 2\text{cm}$ . For the ratio of  $b/a = 2$  and for a sphere under free-free boundary conditions, the dimensionless fundamental natural frequency is read as  $\beta = 1.01034$  from Table 4. The dimensional natural frequency is, accordingly, found as

$$\omega_{Steel} = (5875.097045) \frac{(1.01034)}{(0.01)} \frac{1}{2\pi} \frac{1}{1000} = 94.47 \text{ kHz}$$

$$\omega_{Aluminium} = (5907.646308) \frac{(1.01034)}{(0.01)} \frac{1}{2\pi} \frac{1}{1000} = 94.995 \text{ kHz}$$

As a final example, let's consider Kim et al.'s example sphere under free-free surfaces [50]:  $E = 53.2GPa, \rho = 7700 \text{ kg/m}^3, \nu = 0.261, b/a = 10\text{mm}/8\text{mm} = 1.25$ . Since Table 4 has been prepared for  $\nu = 0.3$ , the dimensionless fundamental frequency needs to be recalculated by using Eq. (14a). Yıldırım [38] has given this value as  $\beta = 1.32553$ . By using this data, the following results are obtained:

$$\sqrt{\frac{\lambda + 2\mu}{\rho}} = 2910.456959 \text{ m/s}$$

$$\omega_{Present} = (2910.456959) \frac{(1.32553)}{(0.008)} \frac{1}{2\pi} \frac{1}{1000} = 76.75044234 \text{ kHz}$$

This results overlaps with the open literature:

$$\omega_{Kim \text{ et al.}[50]} = 76.7 \text{ kHz}$$

$$\omega_{Yıldırım [38]} = 76.75044 \text{ kHz}$$

## 6. Conclusions

In this work the exact one-dimensional axisymmetric radial free vibration analysis of a thick-walled sphere was handled systematically. Frequency equations in terms of spherical Bessel functions were presented in closed form for four possible classical boundary conditions. The numerical results were verified with the available literature.

Besides, a parametric study for the investigation of natural frequencies with both the sphere aspect ratios and boundary conditions was conducted for the isotropic and homogeneous linear elastic materials having Poisson ratio of  $\nu = 0.3$ . The following distinctive features were observed:

- i. Increasing the total number of the degrees of freedom at both ends decreases significantly the frequencies. This is the most noticeable characteristic among the fundamental frequencies. As a consequence of this, free-free ends offer the smallest natural frequency. The converse is true for fixed-fixed ends.
- ii. There is no such a significant difference between the natural frequencies of fixed-free and free-fixed boundary conditions for  $1.02 \leq b/a \leq 2$  and  $\nu = 0.3$ . Those differences, however, become more obvious towards  $b/a = 2$ .
- iii. An increase in the thickness of the sphere makes the dimensionless natural frequencies small. Thin-walled spheres have higher dimensionless natural frequencies than thick-walled ones.

Since the interest in CNT-reinforced aluminum composites has been growing considerably, a case study with an aluminum matrix dispersed by either SWCNT or MWCNT was carried out. Enhancements of up to 23% in natural frequencies compared to pure aluminium were observed for the inclusion of 5 wt.%SWCNT into *Al* matrix. It was also revealed that MWCNT inclusion into *Al* matrix makes almost does not a contribution on the natural frequencies.

In conclusion, it was seen that the given closed-form characteristic equations and some numerical results in the present work may readily be used for hollow spheres made of any kind of isotropic and homogeneous linear elastic material even for some kind of CNT reinforced composites.

**Acknowledgement:** I thank to the referees for the effort and time spent together with their constructive feedback.

## References

- [1] Horace Lamb MA. On the vibrations of an elastic sphere. Proceedings of the London Mathematical Society, 1881; 1-13 (1): 189–212.
- [2] Horace Lamb MA. On the vibrations of a spherical shell. Proceedings of the London Mathematical Society, 1882; 14(1): 50-56. <https://doi.org/10.1112/plms/s1-14.1.50>
- [3] Sato Y, Usami T. Basic study on the oscillation of homogeneous elastic sphere-part I. Frequency of the free oscillations. Geophysics Magazine, 1962; 31(1): 15-24.
- [4] Sato, Y, Usami T. Basic study on the oscillation of homogeneous elastics sphere-part II. Distribution of displacement", Geophysics Magazine, 1962; 31(1): 25-47.
- [5] Shah H, Ramkrishana CV, Datta SK. Three dimensional and shell theory analysis of elastic waves in a hollow sphere-part I. Analytical foundation. ASME, Journal of Applied Mechanics, 1969; 36(3): 431-439. <https://doi.org/10.1115/1.3564698>
- [6] Shah H, Ramkrishana CV, Datta SK. Three dimensional and shell theory analysis of elastic waves in a hollow sphere-part II. Numerical results. ASME, Journal of Applied Mechanics, 1969; 36(3): 440-444. <https://doi.org/10.1115/1.3564699>
- [7] Seide P. Radial vibrations of spherical shells. J. Appl. Mech, 1970; 37(2): 528-530. <https://doi.org/10.1115/1.3408540>
- [8] Scaffbuch PJ, Rizzo FJ, Thomson RB. Eigen frequencies of an elastic sphere with fixed boundary conditions. J. Appl. Mech., 1992; 59(2): 458–459. <https://doi.org/10.1115/1.2899545>
- [9] Gosh AK, Agrawal MK. Radial vibrations of spheres. Journal of Sound and Vibration, 1994; 171(3): 315–322. <https://doi.org/10.1006/jsvi.1994.1123>

- [10] Abbas I. Analytical solution for a free vibration of a thermoelastic hollow sphere. *Mechanics Based Design of Structures and Machines*, 2015; 43(3): 265-276. <https://doi.org/10.1080/15397734.2014.956244>
- [11] Sharma JN, Sharma N. Free vibration analysis of homogeneous thermoelastic solid sphere. *Journal of Applied Mechanics, ASME*, 2010; 77(2): 021004. <https://doi.org/10.1115/1.3172141>
- [12] Sharma N. Modeling and analysis of free vibrations in thermoelastic hollow spheres. *Multidiscipline modeling in materials and structures*, 2015; 11(2): 134-159. <https://doi.org/10.1108/MMMS-05-2014-0033>
- [13] Hoppmann II WH, Baker WE. Extensional vibrations of elastic orthotropic spherical shells. *Journal of Applied Mechanics*, 1961; 28: 229-237. <https://doi.org/10.1115/1.3641659>
- [14] Eason G. On the vibration of anisotropic cylinders and spheres. *Applied Scientific Research, Section A*, 1963; 12: 81-85. <https://doi.org/10.1007/BF03184751>
- [15] Cohen H, Shah AH. Free vibrations of a spherically isotropic hollow sphere. *Acustica*, 1972; 26: 329-333.
- [16] Nelson RB. Natural vibrations of laminated orthotropic spheres. *International Journal of Solids and Structures*, 1973; 9(3): 305-311. [https://doi.org/10.1016/0020-7683\(73\)90081-4](https://doi.org/10.1016/0020-7683(73)90081-4)
- [17] Shul'ga NA, Grigorenko AY, E'mova TL. Free non-axisymmetric oscillations of a thick-walled, nonhomogeneous, transversely isotropic, hollow sphere. *Soviet Applied Mechanics*, 1988; 24: 439-444. <https://doi.org/10.1007/BF00883063>
- [18] Grigorenko YM, Kilina TN. Analysis of the frequencies and modes of natural vibration of laminated hollow spheres in three-dimensional and two-dimensional formulations. *Soviet Applied Mechanics*, 1989; 25: 1165-1171. <https://doi.org/10.1007/BF00887140>
- [19] Heyliger PR, Jilani A. The free vibrations of inhomogeneous elastic cylinders and spheres. *International Journal of Solids and Structures*, 1992; 29(22): 2689-2708. [https://doi.org/10.1016/0020-7683\(92\)90112-7](https://doi.org/10.1016/0020-7683(92)90112-7)
- [20] Jiang H, Young PG, Dickinson SM. Natural frequencies of vibration of layered hollow spheres using three-dimensional elasticity equations. *Journal of Sound and Vibration*, 1996; 195(1): 155-162. <https://doi.org/10.1006/jsvi.1996.0412>
- [21] Ding HJ, Chen WQ. Nonaxisymmetric free vibrations of a spherically isotropic spherical shell embedded in an elastic medium. *International Journal of Solids and Structures*, 1996; 33: 2575-2590. [https://doi.org/10.1016/0020-7683\(95\)00171-9](https://doi.org/10.1016/0020-7683(95)00171-9)
- [22] Ding HJ, Chen WQ. Natural frequencies of an elastic spherically isotropic hollow sphere submerged in a compressible fluid medium. *Journal of Sound and Vibration*, 1996; 192(1): 173-198. <https://doi.org/10.1006/jsvi.1996.0182>
- [23] Chen WQ, Ding HJ. Natural frequencies of a fluid-filled anisotropic spherical shell. *Journal of the Acoustical Society of America*, 1999; 105: 174-182. <https://doi.org/10.1121/1.424578>
- [24] Chen WQ, Cai JB, Ye GR, Ding HJ. On eigen frequencies of an anisotropic sphere. *ASME, Journal of Applied Mechanics*, 2000; 67(2): 422-424. <https://doi.org/10.1115/1.1303803>
- [25] Chen WQ, Ding HJ. Free vibration of multi-layered spherically isotropic hollow spheres. *International Journal of Mechanical Sciences*, 2001; 43(3): 667-680. [https://doi.org/10.1016/S0020-7403\(00\)00044-8](https://doi.org/10.1016/S0020-7403(00)00044-8)
- [26] Stavsky Y, Greenberg JB. Radial vibrations of orthotropic laminated hollow spheres. *J Acoust Soc Am*, 2003; 113: 847-851. <https://doi.org/10.1121/1.1536625>
- [27] Ding HJ, Wang HM. Discussions on "Radial vibrations of orthotropic laminated hollow spheres" [*J Acoust Soc Am*, 113, 847-851 (2003)]. *The Journal of the Acoustical Society of America*, 2004; 115: 1414. <https://doi.org/10.1121/1.1649911>
- [28] Sharma JN, Sharma N. Vibration analysis of homogeneous transversely isotropic generalized thermoelastic spheres. *Journal of Vibration and Acoustics, ASME*, 2011; 133(4): 041001. <https://doi.org/10.1115/1.4003396>

- [29] Keles İ. Novel approach to forced vibration behavior of anisotropic thick-walled spheres. AIAA Journal, 2016; 54(4): 1438-1442. <https://doi.org/10.2514/1.J054322>
- [30] Chen WQ, Ding HJ, Xu RQ. Three-dimensional free vibration analysis of a fluid-filled piezoceramic hollow sphere. Computers and Structures, 2001; 79(6): 653-663. [https://doi.org/10.1016/S0045-7949\(00\)00166-8](https://doi.org/10.1016/S0045-7949(00)00166-8)
- [31] Chiroiu V, Munteanu L. On the free vibrations of a piezoceramic hollow sphere. Mechanics Research Communications, 2007; 34: 123-129. <https://doi.org/10.1016/j.mechrescom.2006.06.011>
- [32] Chen WQ, Wang X, Ding, HJ. Free vibration of a fluid-filled hollow sphere of a functionally graded material with spherical isotropy. Journal of the Acoustical Society of America, 1999; 106: 2588-2594. <https://doi.org/10.1121/1.428090>
- [33] Chen WQ, Wang LZ, Lu Y. Free vibrations of functionally graded piezoceramic hollow spheres with radial polarization. Journal of Sound and Vibration, 2002; 251(1): 103-114. <https://doi.org/10.1006/jsvi.2001.3973>
- [34] Ding HJ, Wang HM, Chen WQ. Dynamic responses of a functionally graded pyroelectric hollow sphere for spherically symmetric problems. Int J Mech Sci, 2003; 45: 1029-1051. <https://doi.org/10.1016/j.ijmecsci.2003.09.005>
- [35] Kanoria M, Ghosh MK. Study of dynamic response in a functionally graded spherically isotropic hollow sphere with temperature dependent elastic parameters. J Thermal Stresses, 2010; 33: 459-484. <https://doi.org/10.1080/01495731003738440>
- [36] Keleş İ, Tütüncü N. Exact analysis of axisymmetric dynamic response of functionally graded cylinders (or disks) and spheres. Journal of Applied Mechanics; 78 (6), 061014, 2011 (7 pages).
- [37] Sharma PK, Mishra, KC. Analysis of thermoelastic response in functionally graded hollow sphere without load. Journal of Thermal Stresses, 2017; 40(2), 185-197. <https://doi.org/10.1080/01495739.2016.1231024>
- [38] Yıldırım, V. Exact radial free vibration frequencies of power-law graded spheres. Journal of Applied and Computational Mechanics, 2018; 4(3): 175-186. doi: [10.22055/JACM.2017.22987.1145](https://doi.org/10.22055/JACM.2017.22987.1145)
- [39] Esawi AMK, Morsi K, Sayed A, Abdel Gawad A, Borah P. Fabrication and properties of dispersed carbon nanotube-aluminium composites. Mater Sci Eng A, 2009; 508(1-2): 167-173. <https://doi.org/10.1016/j.msea.2009.01.002>
- [40] Esawi AMK, Morsi K, Sayed A, Taher M, Lanka S. Effect of carbon nanotube (CNT) content on the mechanical properties of CNT-reinforced aluminium composites. Composites Science and Technology, 2010; 70(16): 2237-2241. <https://doi.org/10.1016/j.compscitech.2010.05.004>
- [41] Neubauer E, Kitzmantel M, Hulman M, Angerer P. Potential and challenges of metal-matrix-composites reinforced with carbon nanofibers and carbon nanotubes. Composites Science and Technology, 2010; 70: 2228-2236. <https://doi.org/10.1016/j.compscitech.2010.09.003>
- [42] Yıldırım, V. Exact radial natural frequencies of functionally graded hollow long cylinders. International Journal of Engineering & Applied Sciences (IJEAS), 2017; 9(4): 28-41. <https://doi.org/10.24107/ijeas.336621>
- [43] Yıldırım, V. Exact in-plane natural frequencies in purely radial modes and corresponding critical speeds of functionally graded (FG) non-uniform disks, American Journal of Modern Physics and Application, 2018; 5(1): 9-23.
- [44] Watson GN. A Treatise on the Theory of Bessel Functions. Cambridge University Press, 1922.
- [45] Bowman F. Introduction to Bessel functions, New York: Dover, 1958.
- [46] Hildebrand FB. Advanced Calculus for Applications. Prentice-Hall, Inc. Englewood Cliffs, New Jersey, 1962.
- [47] Abramowitz M, Stegun, IA (Eds.). §9.1.1 in Handbook of Mathematical Functions with Formulas, Graphs, and Mathematical Tables, 9th printing, New York, Dover, 1972.

- [48] Costa DMS, Loja MAR. On the characterization of the free vibrations behavior of multiscale composite plates. *Research on Engineering Structures and Materials (RESM)*, 2017; 3(1): 27-44. <https://doi.org/10.17515/resm2016.43st0602>
- [49] Halpin, JC, Kardos, JL. The Halpin-Tsai Equations: A Review. *Polymer Engineering and Science*, 1976; 344:352, 16(5).
- [50] Kim JO, Lee JG, Chun HY. Radial vibration characteristics of spherical piezoelectric transducers, *Ultrasonics*, 2005; 43: 531–537. <https://doi.org/10.1016/j.ultras.2005.01.004>



ResearchArticle

## Inclusion compound formation between hazelnut oil and gamma cyclodextrin

Zeynep Ömeroğulları Başyığıt<sup>a</sup>

*Department of Textile Engineering, Faculty of Engineering, Usak University, Usak, Turkey*

### Article Info

### Abstract

#### Article history:

Received 26 Dec 2018

Revised 16 Jan 2019

Accepted 22 Jan 2019

#### Keywords:

Cyclodextrin;

Gamma;

Hazelnut oil;

Inclusion compound

Research in macromolecular self-assembly has been progressively developed since the 1970s and in recent years, more factors and concepts in supramolecular chemistry have been introduced into studies of the self-assembly of polymers. In this respect, inclusion complexation based on cyclodextrins plays a significant role. Hazelnut oil has been used in food and pharmaceutical industry due to its unique properties. Due to its high vitamin-E content, hazelnut oil can slow down the oxidation process; therefore, hazelnut oil can be used as an effective antioxidant. In this study, inclusion complexation between cyclodextrin and hazelnut oil was investigated in detail. In order to form an inclusion compound excess amount of cyclodextrin (CD) and hazelnut oil (H-oil) was used in the experimental part and it was successfully demonstrated that hazelnut oil formed an inclusion compound with gamma cyclodextrin. This inclusion compound could be used either in food products or specific applications used with textile materials since the components performed in this research were both biodegradable and bioabsorbable. Cyclodextrin, inclusion compound, physical mixture of it and hazelnut oil pure state were characterized by FTIR-ATR (Fourier Transform Infrared Spectroscopy-Attenuated Total Reflection), TGA (Thermal Gravimetric Analysis) and XRD (X-Ray Diffraction) analyses. According to the results, hazelnut oil as a guest material was successfully encapsulated in the cavities of host gamma cyclodextrin (g-CD) and FTIR studies indicated that both guest and host molecules were present in the precipitated inclusion complexes (ICs).

© 2018 MIM Research Group. All rights reserved

## 1. Introduction

Macromolecular self-assembly includes two major fields, i.e. supramolecular polymers, which are formed from small molecules driven by non-covalent interactions, and self-assembly of multicomponent systems in which macromolecules serve as at least one of the components. Inclusion complexation, normally involves the interactions of two components, so called “host” and “guest” molecules. It is not generally recognized as one kind of the basic non-covalent interactions, because of its combination nature of several elemental supramolecular interactions. The inclusion complexation between CDs and various guests has been extensively investigated in supramolecular chemistry resulting in a broad scope of guest molecules available under different conditions [1].

Cyclodextrins are truncated cone structures composed of 1, 4 linked alpha glucose units. Number of glucose units determines the diameter of inner cavity of cyclodextrins. Since

<sup>a</sup>Corresponding author: [zeynep.omerogullari@usak.edu.tr](mailto:zeynep.omerogullari@usak.edu.tr)

<sup>o</sup>[orcid.org/0000-0002-1526-8662](https://orcid.org/0000-0002-1526-8662)

DOI: <http://dx.doi.org/10.17515/resm2018.84ma1226>

Res. Eng. Struct. Mat. Vol. 5 Iss. 1 (2019) 33-41

alpha cyclodextrin compose of 6 glucose units, it has the smallest cavity with a diameter of 0,49 nm. Beta cyclodextrin and gamma cyclodextrins compose of 7 and 8 glucose units and their cavity sizes are 0.62 and 0.79 nm, respectively [2]. Cavity size is the most critical parameter on inclusion compound formation because it determines the maximum possible size of the guest molecule that can be host inside the cyclodextrin molecule. Basic structure of gamma CD and mode of complexation with guest compounds are schematically indicated in Fig.1. Hydrophobicity of the molecule is another factor playing a role in the inclusion compound formation. Hydroxyl groups of cyclodextrins are located on the outer surface of the molecules, resulting a hydrophilic surface and hydrophobic inner cavity. Thus, hydrophobic molecules, such as oil molecules, can conveniently form inclusion compounds with cyclodextrins. Hydrophobic guest molecules are thermodynamically more stable inside the cavity of cyclodextrin rather than in aqueous solution and therefore they form a non-covalently bonded complex, called an inclusion complex (IC) [3]. There are several studies on inclusion compound formation between cyclodextrin and essential oils such as *Ocimum basilicum* [4], garlic [5], lemon [6], cinnamon [7,8], citronella [9], crude [10], thyme [11], *Lippiasidoides Cham* [12], *Litsea cubeba* [13], soybean, sweet almond [14], eucalyptus [15], black pepper [16], yarrow [17], fish, tarragon, mustard, peppermint, marjoram [18], tea tree [19] oils.

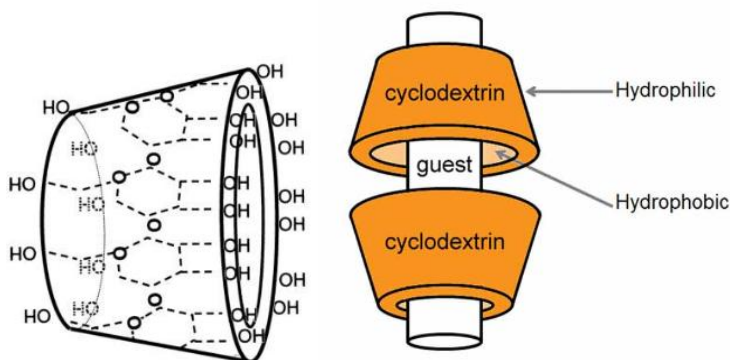
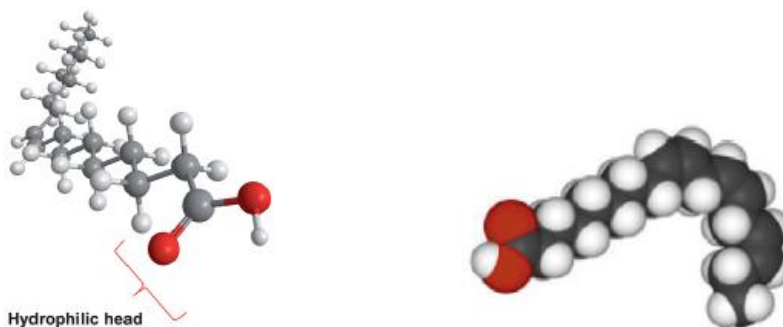


Fig. 1 Basic structure of a g-cyclodextrin and mode of complexation with guest compounds [20]

Hazelnuts (*Corylus avellana L.*) are mainly cultivated in Turkey and Italy which belong to the *Betulaceae* family and they are particularly valuable for their lipids, which account for 60% of the hazelnut kernel. Recently, hazelnut oil (H-oil) has been gaining recognition as a high-quality food product because of its fatty acid composition, which includes oleic and linoleic acids as well as vitamin E (a-tocopherol) and sterols. Monounsaturated and polyunsaturated fatty acids, as well as minor lipid components, play an important role in human nutrition and health such as lowering cholesterol levels [21,22]. It is also a good source of vitamin-E which is fat soluble and an antioxidant material in the human body that protects against free radical damage [23]. Turkey is the world's largest hazelnut producer, contributing approximately 70 % to the total global production. [24,25].

In hazelnut oil chemical structure, oleic acid (Fig.2.a) is the dominant fatty acid (74.2–82.8%) in all varieties while linoleic acid (Fig. 2.b) is the second most abundant fatty acid in the samples and its range is between 9.82% and 18.7%. Palmitic, stearic and palmitoleic acids follows this [26].



a) Chemical structure of oleic acid b) Chemical structure of linoleic acid

Fig. 2 Chemical structure of oleic acid (a) [27] and linoleic acid (b) [28]

Due to its high vitamin-E content, hazelnut oil can slow down the oxidation process. Moreover, most of its oil content composes of unsaturated oil, which also minimize the oil oxidation. Because of these aforementioned properties, hazelnut oil is an effective antioxidant [29].

According to the best knowledge we have, hazelnut oil/ $\gamma$ -cyclodextrin inclusion compound formation has not been studied. In this study, hazelnut oil was employed as a guest molecule while  $\alpha$ ,  $\beta$ , and  $\gamma$  cyclodextrins acted as host molecules. Our results indicated that only  $\gamma$  cyclodextrin molecules were able to form inclusion compound with the hazelnut oil. While inclusion compound formation process between  $\alpha$  and  $\beta$  cyclodextrin and hazelnut oil resulted in phase separated transparent solutions,  $\gamma$  cyclodextrin and hazelnut oil formed a homogenous white colored solution and then precipitated down. This precipitation was characterized with FTIR, Wide Angle X-Ray, and Thermogravimetric Analyzer to confirm the inclusion compound formation.

## 2. Experimental: Co-precipitation method

$\gamma$  cyclodextrin was obtained from Cerestar, USA. Hazelnut oil was purchased from Zade Vital, Turkey. All chemicals were used without further purification. Cyclodextrin was dissolved in deionized water. In order to form a stoichiometric inclusion compound excess amount of cyclodextrin dissolved in water and due to the 15:1 host/guest material ratio, guest material was added drop by drop, first they were sonicated in an ultrasonic bath for 10 mins and then stirred on a hot plate for 2 hours in a flask. After this process, samples were left undisturbed two hours and then filtered using a vacuum pump and filter paper. Precipitated inclusion compound were oven dried for 24 hours at 50 °C before conducting any instrumental characterization.

FTIR-ATR (Fourier Transform Infrared Spectroscopy-Attenuated Total Reflection), spectrum of samples was collected using a Nicolet 510P in the range of 4000-400  $\text{cm}^{-1}$ . Each sample was scanned 64 times and analyzed by using the Omnic software.

Thermal decomposition of samples was analyzed using Perkin Elmer (TGA) Thermogravimetric analyzer. During these experiments nitrogen gas was used to purge the furnace. Samples were heated from 25 to 900 °C.

Crystal structures of samples were characterized via using a Siemens type-F X-Ray Diffractometer (XRD) equipped with a Ni-FILTERED CuK<sub>α</sub> radiation source ( $k=1.54 \text{ \AA}$ ). The supplied current and voltage were 30 kV and 20 mA, respectively, and diffraction intensities were collected every  $0.1^\circ$  from  $2\theta=5^\circ$  to  $30^\circ$  at a rate of  $2\theta=3^\circ/\text{min}$ .

### 3. Results and Discussions

According to the test results, gamma cyclodextrin (g-CD) molecules were able to form inclusion compound with the hazelnut oil. Therefore, further characterization was conducted only for the hazelnut oil and gamma CD inclusion compound which was coded as hazelnut oil-g-CD (H-g-IC). While inclusion compound formation process between alpha and beta cyclodextrin and hazelnut oil resulted in phase separated transparent solutions, gamma cyclodextrin and hazelnut oil formed a homogenous white colored solution and then precipitated down. It was explained in the literature [2] that the first indication of inclusion complex formation was the columnar crystal structure of cyclodextrin and columnar structures improved when CDs stacked on top of one another and produced endless channels in which guest molecules resided. These channels were stabilized by guest molecules and hydrogen bonds between the hydroxyl groups of cyclodextrin yielding a head to head or head to tail arrangement.

As seen in Fig. 3, Wide-angle X-ray diffraction (WAXD) scattering patterns substantially differed after the inclusion of guest hazelnut oil molecules. The reported WAXD pattern for neat cage g-CD had characteristic diffraction peaks at  $2\theta = 12.4^\circ, 16.5^\circ, 18.8^\circ$  and  $23.4^\circ$  and as reported in Fig. 3, these peaks were also observed in as-received g-CD. After the formation of H-g-IC, a new peak appeared at  $2\theta = 7.5^\circ$ , seen in Fig. 4, which corresponded to (200) planes of the hydrated crystals [2]. XRD scattering of physical mixture of hazelnut oil and gamma CD (H-g-mix) was clearly seen in Fig. 5 which had footprints of g-CD in some parts of scattering patterns due to the fact that physical mixture of two compounds did not indicate an inclusion compound.

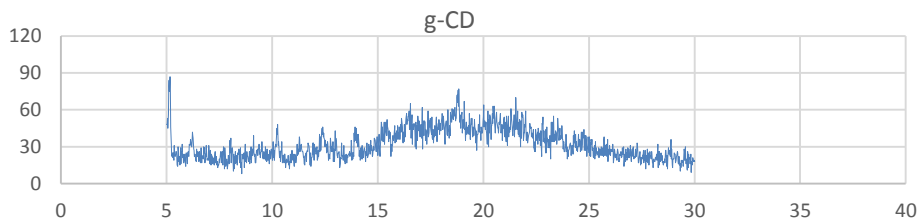


Fig. 3 XRD scattering of gamma CD (g-CD)

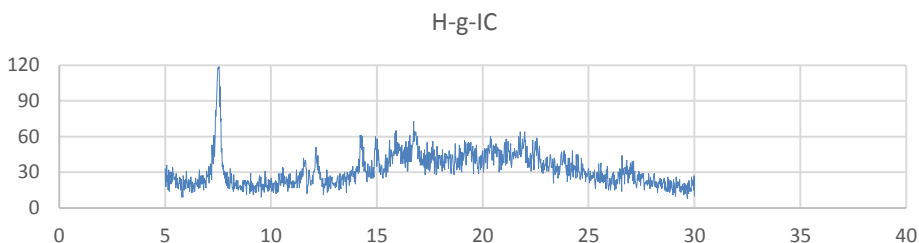


Fig. 4 XRD scattering of hazelnut oil and gamma CD inclusion compound (H-g-IC)

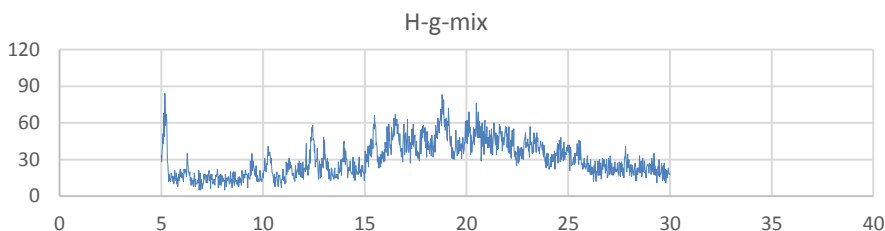


Fig. 5 XRD scattering of physical mixture of hazelnut oil and gamma CD (H-g-mix)

Another proof of successful encapsulation of hazelnut oil molecules in g-cyclodextrin was obtained from FTIR-ATR analysis. In Fig. 6, FTIR-ATR analysis between  $4000-700\text{ cm}^{-1}$  of a) H-g-IC b) H-oil and c) g-CD were showed, respectively. The FTIR spectra of gamma CD showed characteristic bands at  $3388$  and  $2926\text{ cm}^{-1}$  which corresponded to O-H and C-H stretching, respectively. However, in H-oil FTIR spectra, strong characteristic peaks could be clearly seen at  $2922$ ,  $2852$  and  $1743\text{ cm}^{-1}$ , including the fingerprint region. When the spectra of H-g-IC was examined, it could be determined that these characteristic strong peaks that belonged to H-oil, showed themselves within weaker peaks for H-oil appear at  $2918$ ,  $2850$  and  $1740\text{ cm}^{-1}$  which attributed to the formation of inclusion compound of H-oil and gamma CD. Therefore the coexistence of P and CD was confirmed in FTIR-ATR analysis of H-g-IC. The fact that the guest H-oil peaks were very weak when compared to CD vibrational bands in the IC was not surprising considering the expected weight ratio of guest/host molecules was around 1:15.

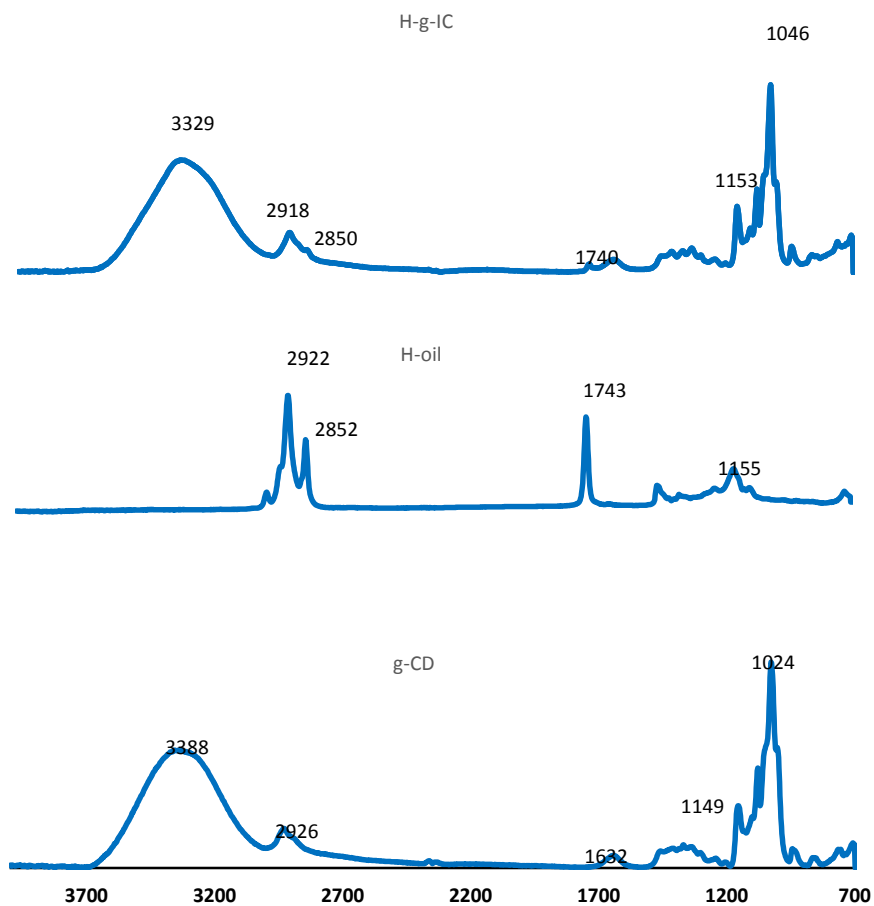
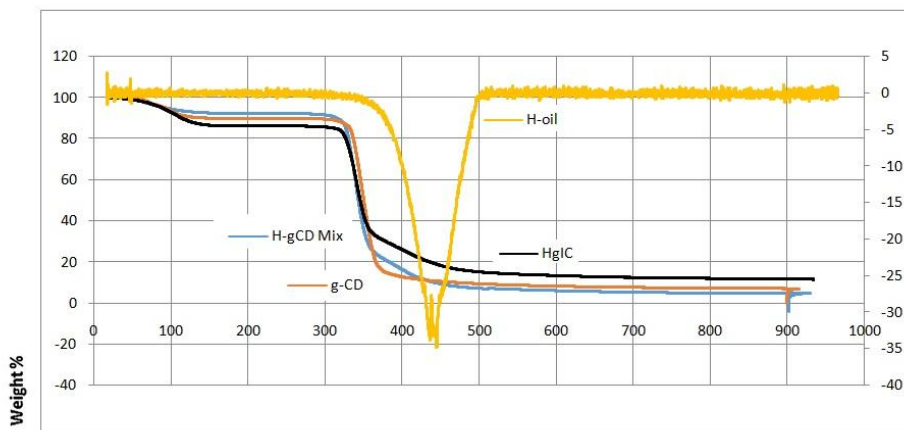


Fig. 6 FTIR-ATR analysis between 4000-700  $\text{cm}^{-1}$  of a) H-g-IC b) H-oil c) g-CD, respectively

In Fig. 7, thermogravimetric analyses of gamma CD, H-oil, their physical mixture H-g-Mix and their inclusion compound H-g-IC could be seen clearly. Decomposition experiments were performed by TGA using  $\text{N}_2$  as an inert carrier gas with heating rate of  $10\text{ }^\circ\text{C}/\text{min}$ , from 25 to  $900\text{ }^\circ\text{C}$ . According to TGA results seen in Fig. 7, hazelnut oil showed that it was thermally stable up to  $300\text{ }^\circ\text{C}$  and the decomposition range of hazelnut oil was  $302\text{-}445\text{ }^\circ\text{C}$ . The stability could be attributed to an expressive quantity of unsaturated fatty acids in the hazelnut oil, because it was reported in the literature that oil with high concentrations of unsaturated fatty acids was more susceptible to thermal deterioration however it was also explained that several other vegetable oils that contained a high concentration of unsaturated fatty acids possessed stability equivalent to other oils with lesser instauration showing that there were other factors which influence the thermal stability of vegetable oils. Moreover, it was also indicated that the presence of antioxidants also improved oil stability which attributed to the antioxidant material especially to the  $\alpha$ -tocopherol existing in hazelnut oil [30]. It was

considered that all these parameters could provide a high thermal stability of H-oil. When thermograph of g-CD was examined, it could be seen that the main weight loss due to degradation occurred between 300 and 350°C. Successful encapsulation of hazelnut oil in g-cyclodextrin could be obtained from H-g-IC thermographs which showed a gradual weight loss between 291-341°C. Since there was a physical mixture in H-g-Mix, not a synthesized compound, TGA thermograph of its physical mixture showed a two-step weight loss, between 258-340 °C and 366-404 °C.



**Fig. 7.** TGA thermograph of g-CD, H-oil, their physical mixture H-g-CD Mix and their inclusion compound H-g-IC

#### 4. Conclusion

Hazelnut oil was used as a high-quality food product because of its fatty acid composition, which included oleic and linoleic acids as well as vitamin E (α-tocopherol). In this study, differently from the literature, hazelnut oil as a guest material was encapsulated in the cavities of host gamma CD-IC. XRD patterns scattering patterns substantially differed after the inclusion of guest hazelnut oil molecules. FTIR studies also indicated that both guest and host molecules were present in the precipitated inclusion compounds. As a result of thermogravimetric analyses, decomposition range of hazelnut oil was indicated as 302-445°C and it was determined that it had a high thermal stability because of expressive quantity of unsaturated fatty acids and antioxidants such as α-tocopherol existing in the structure of it. It was considered that this successfully performed inclusion compound could be used either in food products or specific applications used with textile materials such as cosmetotextiles in further studies.

#### References

- [1] Chen, Guosong, and Ming Jiang. Cyclodextrin-based inclusion complexation bridging supramolecular chemistry and macromolecular self-assembly. *Chemical Society Reviews* 2011; 40.5; 2254-2266. <https://doi.org/10.1039/c0cs00153h>

- [2] Gurarслан, A., Shen, J., Caydamli, Y., & Tonelli, A. E. Pyriproxyfen cyclodextrin inclusion compounds. *Journal of Inclusion Phenomena and Macrocyclic Chemistry* 2015; 82(3-4); 489-496. <https://doi.org/10.1007/s10847-015-0526-7>
- [3] Tonelli, A. E. Molecular processing of polymers with cyclodextrins. In *Inclusion Polymers* 2009 (pp. 55-77). Springer Berlin Heidelberg. [https://doi.org/10.1007/12\\_2008\\_2](https://doi.org/10.1007/12_2008_2)
- [4] Rodrigues, L. B., Martins, A. O. B. P. B., Ribeiro-Filho, J., Cesário, F. R. A. S., e Castro, F. F., de Albuquerque, T. R., dos Passos Menezes, P. Anti-inflammatory activity of the essential oil obtained from *Ocimum basilicum* complexed with  $\beta$ -cyclodextrin ( $\beta$ -CD) in mice. *Food and Chemical Toxicology*, 2017; 109;836-846. <https://doi.org/10.1016/j.fct.2017.02.027>
- [5] Wang, J., Cao, Y., Sun, B., & Wang, C. Physicochemical and release characterisation of garlic oil- $\beta$ -cyclodextrin inclusion complexes. *Food chemistry* 2011; 127(4);1680-1685. <https://doi.org/10.1016/j.foodchem.2011.02.036>
- [6] Bhandari, B. R., D'Arc, B. R., & Padukka, I. Encapsulation of lemon oil by paste method using  $\beta$ -cyclodextrin: encapsulation efficiency and profile of oil volatiles. *Journal of Agricultural and Food Chemistry* 1999; 47(12); 5194-5197. <https://doi.org/10.1021/jf9902503>
- [7] Petrović, G. M., Stojanović, G. S., & Radulović, N. S. Encapsulation of cinnamon oil in  $\beta$ -cyclodextrin. *Journal of medicinal plants research* 2013; 4(14); 1382-1390.
- [8] Ayala-Zavala, J. F., Soto-Valdez, H., González-León, A., Álvarez-Parrilla, E., Martin-Belloso, O., & González-Aguilar, G. A. Microencapsulation of cinnamon leaf (*Cinnamomum zeylanicum*) and garlic (*Allium sativum*) oils in  $\beta$ -cyclodextrin. *Journal of Inclusion Phenomena and Macrocyclic Chemistry* 2008; 60(3-4); 359-368. <https://doi.org/10.1007/s10847-007-9385-1>
- [9] Songkro, S., Hayook, N., Jaisawang, J., Maneenuan, D., Chuchome, T., & Kaewnopparat, N. Investigation of inclusion complexes of citronella oil, citronella and citronellol with  $\beta$ -cyclodextrin for mosquito repellent. *Journal of Inclusion Phenomena and Macrocyclic Chemistry* 2012; 72(3-4); 339-355. <https://doi.org/10.1007/s10847-011-9985-7>
- [10] Serio N, Levine M. Efficient extraction and detection of aromatic toxicants from crude oil and tar balls using multiple cyclodextrin derivatives. *Marine pollution bulletin* 2015; 95(1); 242-247. <https://doi.org/10.1016/j.marpolbul.2015.04.008>
- [11] Del Toro-Sánchez, C. L., Ayala-Zavala, J. F., Machi, L., Santacruz, H., Villegas-Ochoa, M. A., Alvarez-Parrilla, E., & González-Aguilar, G. A. Controlled release of antifungal volatiles of thyme essential oil from  $\beta$ -cyclodextrin capsules. *Journal of inclusion phenomena and macrocyclic chemistry* 2010; 67(3-4); 431-441. <https://doi.org/10.1007/s10847-009-9726-3>
- [12] Fernandes, L. P., Éhen, Z., Moura, T. F., Novák, C., & Sztatisz, J. Characterization of Lippia sidoides oil extract- $\beta$ -cyclodextrin complexes using combined thermoanalytical techniques. *Journal of thermal analysis and calorimetry* 2004; 78(2); 557-573. <https://doi.org/10.1023/B:JTAN.0000046119.33278.9f>
- [13] Wang, Y., Jiang, Z. T., & Li, R. Complexation and molecular microcapsules of Litsea cubeba essential oil with  $\beta$ -cyclodextrin and its derivatives. *European Food Research and Technology* 2009; 228(6); 865-873. <https://doi.org/10.1007/s00217-008-0999-3>
- [14] Hamoudi, M. C., & Bochot, A. Oil-cyclodextrin based beads for oral delivery of poorly-soluble drugs. *Current topics in medicinal chemistry* 2014; 14(4); 510-517. <https://doi.org/10.2174/1568026613666131219124539>
- [15] Kringel, D. H., Antunes, M. D., Klein, B., Crizel, R. L., Wagner, R., Oliveira, R. P. & Zavareze, E. D. R. Production, Characterization, and Stability of Orange or Eucalyptus Essential Oil/ $\beta$ -Cyclodextrin Inclusion Complex. *Journal of food science* 2017; 82(11); 2598-2605. <https://doi.org/10.1111/1750-3841.13923>
- [16] Rakmai, J., Cheirsilp, B., Mejuto, J. C., Torrado-Agrasar, A., & Simal-Gándara, J. Physico-chemical characterization and evaluation of bio-efficacies of black pepper essential oil

- encapsulated in hydroxypropyl-beta-cyclodextrin. *Food hydrocolloids* 2017; 65; 157-164. <https://doi.org/10.1016/j.foodhyd.2016.11.014>
- [17] Rakmai, J., Cheirsilp, B., Torrado-Agrasar, A., Simal-Gándara, J., & Mejuto, J. C. Encapsulation of yarrow essential oil in hydroxypropyl-beta-cyclodextrin: physiochemical characterization and evaluation of bio-efficacies. *CyTA-Journal of Food* 2017; 15(3); 409-417. <https://doi.org/10.1080/19476337.2017.1286523>
- [18] Wadhwa, G., Kumar, S., Chhabra, L., Mahant, S., & Rao, R. Essential oil-cyclodextrin complexes: an updated review. *Journal of Inclusion Phenomena and Macrocyclic Chemistry* 2017; 89(1-2); 39-58. <https://doi.org/10.1007/s10847-017-0744-2>
- [19] Shrestha, M., Ho, T. M., & Bhandari, B. R. Encapsulation of tea tree oil by amorphous beta-cyclodextrin powder. *Food chemistry* 2017; 221; 1474-1483. <https://doi.org/10.1016/j.foodchem.2016.11.003>
- [20] Crumling, M. A., King, K. A., & Duncan, R. K. Cyclodextrins and Iatrogenic Hearing Loss: New Drugs with Significant Risk. *Frontiers in cellular neuroscience* 2017, 11. <https://doi.org/10.3389/fncel.2017.00355>
- [21] Karabulut, I., Topcu, A., Yorulmaz, A., Tekin, A., & Ozay, D. S. Effects of the industrial refining process on some properties of hazelnut oil. *European journal of lipid science and technology* 2005; 107(7-8); 476-480. <https://doi.org/10.1002/ejlt.200501147>
- [22] Ozen, B. F., & Mauer, L. J. Detection of hazelnut oil adulteration using FT-IR spectroscopy. *Journal of agricultural and food chemistry* 2002; 50(14); 3898-3901. <https://doi.org/10.1021/jf0201834>
- [23] Azzi, A., & Stocker, A. Vitamin E: non-antioxidant roles. *Progress in lipid research* 2000; 39(3);231-255. [https://doi.org/10.1016/S0163-7827\(00\)00006-0](https://doi.org/10.1016/S0163-7827(00)00006-0)
- [24] Tatar, F., Tunç, M. T., & Kahyaoglu, T. Turkish Tombul hazelnut (*Corylus avellana* L.) protein concentrates: functional and rheological properties. *Journal of food science and technology* 2015; 52(2); 1024-1031. <https://doi.org/10.1007/s13197-013-1110-z>
- [25] Yalcin, H., Ozturk, I., Karaman, S., Kisi, O., Sagdic, O., & Kayacier, A. Prediction of Effect of Natural Antioxidant Compounds on Hazelnut Oil Oxidation by Adaptive Neuro-Fuzzy Inference System and Artificial Neural Network. *Journal of food science* 2011, 76(4). <https://doi.org/10.1111/j.1750-3841.2011.02139.x>
- [26] Köksal, A. İ., Artık, N., Şimşek, A., & Güneş, N. Nutrient composition of hazelnut (*Corylus avellana* L.) varieties cultivated in Turkey. *Food Chemistry* 2006; 99(3); 509-515. <https://doi.org/10.1016/j.foodchem.2005.08.013>
- [27] Nikiforidis, C. V., Gilbert, E. P., & Scholten, E. Organogel formation via supramolecular assembly of oleic acid and sodium oleate. *Rsc Advances* 2015; 5(59); 47466-47475. <https://doi.org/10.1039/C5RA05336F>
- [28] Miranda, J., Arias, N., Fernández-Quintela, A., & del Puy Portillo, M. Are conjugated linolenic acid isomers an alternative to conjugated linoleic acid isomers in obesity prevention?. *Endocrinología y Nutrición (English Edition)* 2014; 61(4); 209-219. <https://doi.org/10.1016/j.endonu.2013.04.016>
- [29] Liu, C., Ren, D., Li, J., Fang, L., Wang, J., Liu, J., & Min, W. Cytoprotective effect and purification of novel antioxidant peptides from hazelnut (*C. heterophylla* Fisch) protein hydrolysates. *Journal of Functional Foods* 2018; 42; 203-215. <https://doi.org/10.1016/j.jff.2017.12.00>
- [30] Ullah, Z., Bustam, M. A., & Man, Z. Characterization of waste palm cooking oil for biodiesel production. *International Journal of Chemical Engineering and Applications* 2014; 5(2); 134. <https://doi.org/10.7763/IJCEA.2014.V5.366>

Blank Page



Research Article

## Finite element analysis of transient thermal performance of a convective-radiative cooling fin: effects of fin tip conditions and magnetic field

M. G. Sobamowo<sup>a</sup>

*Department of Mechanical Engineering, University of Lagos, Akoka, Lagos, Nigeria.*

### Article Info

#### Article history:

Received 25 Jun 2018

Revised 02 Oct 2018

Accepted 25 Oct 2018

#### Keywords:

*Transient analysis;*

*Fin tip conditions;*

*Finite element method;*

*Magnetic field;*

### Abstract

The wide range of applications of cooling fins are evident in heat transfer enhancements for various thermal systems and also, for the control and prevention of thermal damages in mechanical and electronic equipment. In this work, nonlinear thermal behaviour of convective-radiative cooling fin with convective tip and subjected to magnetic field is analyzed using Galerkin finite element method. The numerical solutions are verified by the exact analytical solution of the linearized models using Laplace transforms method. Based on the numerical investigations, it is established that increase in Biot number, convective, radiative and magnetic parameters increase the rate of heat transfer from the fin and consequently improve the efficiency of the cooling fin. Also, the study shows that for a relatively short cooling fin operating for prolonged periods of time or steady state, the adiabatic/hypothetical condition (or negligible heat transfer) at the tip can be assumed without any significant loss in accuracy or equality as compared to the convective condition at the tip. However, for a long cooling fin of finite length operating in a transient state, especially for short period of time, the assumption of insulated tip produces significant different results as compared to the results of the convective tip. Therefore, for transient thermal studies of fins, the assumption that no heat transfer takes place at the fin tip should be taken with caution for a long cooling fin of finite length operating within a relatively short period of time. It is hope that the present study will enhance the understanding of transient thermal response of the solid fin under various factors and fin tip conditions.

© 2018 MIM Research Group. All rights reserved.

## 1. Introduction

The increasing demands for high performance thermal equipment require the development of enhanced heat transfer devices. Also, the generation of excessive heat that leads to thermal-induced failure in various thermal systems calls for the production of effective heat dissipating devices that will enhance the rate of heat transfer from the thermal equipment. In order to meet these needs, extended surfaces such as fins and spines have been applied in various thermal and electronic equipment. Consequently, the applications of the extended surfaces in the thermal systems such as air conditioning, refrigeration, super heaters, automobile, power plants, heat exchangers, convectional furnaces, economizers, gas turbines, chemical processing equipment, oil carrying pipelines, computer processors, electrical chips, electronic and microelectronics components, high-power semi-conductor devices, high-power lasers, light emitting diodes (LEDs), computer cooling, sensitive devices etc. have attracted various research interests in few past decades. The thermal analysis of the extended surfaces involves the development of thermal models for various operating conditions. Different analytical

<sup>\*</sup>Corresponding author: [mikegbeminiyi@gmail.com](mailto:mikegbeminiyi@gmail.com)

<sup>a</sup>orcid.org/0000-0003-2402-1423

DOI: <http://dx.doi.org/10.17515/resm2018.52me0526>

Res. Eng. Struct. Mat. Vol. 5 Iss. 1 (2019) 43-74

(exact and approximate) and numerical methods have been employed by various researchers to analyze the developed thermal models of the extended surfaces. Exact analytical methods such as methods of superposition and separation of variables were employed by Wang *et al.* [1] while Moitsheki and Harley [2], Mhlongo and Moitsheki [3], Ali *et al.* [4] and Kader *et al.* [5] adopted Lie point symmetry method for the thermal analysis of fins. Kirchoff's transformation method was adopted by Moitsheki and Rowjee [6]. In an earlier work, Cole *et al.* [7] made use of Green's functions (GF) in the form of infinite series to present analytical solutions to the differential equations governing the thermal behaviour of fins.

The above reviewed works provided exact analytical solutions to the thermal models governing the thermal behaviours of the fins under various operating conditions. However, most of the developed exact analytical solutions are based on the assumptions of constant thermal properties. Indubitably, the idealization of a constant or uniform heat transfer coefficient is not realistic. This is because in practice, heat transfer coefficients has significantly greater values at the fin tip more than the fin base. Additionally, the heat transfer coefficients vary with temperature. Such variation of the heat transfer coefficient as a function of temperature is often governed by a power law. Moreover, the thermal conductivity of the fin is temperature-dependent. Under these circumstances, the differential equations governing the thermal responses of the fin under various conditions become strictly nonlinear. Therefore, large numbers of the past studies have applied various approximate analytical methods to solve the nonlinear thermal models under various geometrical, internal and external conditions. In past few decades, Jordan *et al.* [8] utilized optimal linearization method while Kundu and Das [9] adopted Frobenius expanding series for the nonlinear fin problems. Homotopy analysis method was used by Khani *et al.* [10] and Amirkolaei and Ganji [11]. Aziz and Bouaziz [12] employed method of least squares while Sobamowo [13], Ganji *et al.* [14] and Sobamowo *et al.* [15] applied Galerkin method of weighted residual to analyze the thermal behaviour of the extended surfaces. In recent times, double decomposition and variation of parameter methods were employed by Sobamowo [16] and Sobamowo *et al.* [17], respectively to investigate the heat transfer characteristics of fins. In some other works, Moradi and Ahmadikia [18], Sadri *et al.* [19], Ndlovu and Moitsheki [20], Mosayebidarchech *et al.* [21], Ghasemi *et al.* [22] and Ganji and Dogonchi [23] adopted differential transformation method to determine the temperature distribution in fins. Applications of homotopy perturbation method to the fin problem was presented by Sobamowo *et al.* [24], Arslanturk [25], Ganji *et al.* [26] and Hoshyar *et al.* [27].

The developed series solutions for the thermal analyses of fins using different approximate analytical methods involve large number of terms. In practice, such expressions involving large number of terms are not convenient for use by designers and engineers [13]. Therefore, over the years, various numerical methods have been explored to analyze the thermal behavior of various extended surfaces. In an earlier work on numerical analysis of determination of temperature distribution in fins, Singh *et al.* [28] adopted meshless element free Galerkin method. Few years later, Basri *et al.* [29] presented a study on the applications of efficient finite element and differential quadrature methods to the heat transfer problems. Singh *et al.* [30] and Sao and Banjare [31] used quasi- steady theory while in the same year, Lotfi and Belkacem [32] and Al- Rashed *et al.* [33] utilized finite volume method for the thermal analysis of fins. In another study, Taler and Taler [34] presented the coupling of finite volume finite element methods to the heat transfer problem. Incremented differential quadrature method was used by Malekzadeh and Rahideh [35]. Reddy *et al.* [36] adopted B- spline based finite element method while Sun *et al.* [37] applied collocation spectral method to the fin problem. Rajul *et al.* [38] examined the thermal response of the fin using Meshless Local Petrov-Galerkin (MLPG). In the

preceding year, Wei *et al.* [39] investigated the thermal behaviour of fin through field synergy principle optimization analysis. Hajabdollahi *et al.* [40] presented genetic algorithm while symbolic programming was used by Fatoorehchi and Abolghasemi [41]. Three years later, Latif *et al.* [42] successfully applied symmetry reduction method to address nonlinear heat transfer problems of fins. In the same year, Mahmoudi and Mejrri [43] used to Lattice Boltzmann method to investigate the effect of variable thermal conductivity and variable refractive index on transient conduction and radiation heat transfer. In some recent studies, Sobamowo [44] and Sobamowo *et al.* [45] applied finite difference and finite volume method, respectively for thermal analysis of longitudinal fin with temperature-dependent thermal conductivity and internal heat generation. Also, Sobamowo *et al.* [46] and Sobamowo [47] adopted Legendre wavelet collocation method to investigate the effects of magnetic field on the thermal performance of convective-radiative fin and also to study heat transfer in porous fin with temperature-dependent thermal conductivity and internal heat generation. Sobamowo and Kamiyo [48] studied multi-boiling heat transfer behavior of a convective straight fin with temperature-dependent thermal properties and internal heat generation using finite volume method. In another study, Chebychev spectral collocation method was used by Sobamowo [49] to examine the heat transfer in porous fin with temperature-dependent thermal conductivity and internal heat generation.

It should be noted that most of the above reviewed studies are based on steady state analysis of fin. However, in many engineering practices and devices such as in automobiles, study of heat transfer in building, industrial applications, transient analysis is very important. In fact, an accurate transient analysis provides insight into the design of fins that would fail in steady-state operations but are sufficient for desired operating periods. Consequently, there have been comparatively few studies on the transient analysis of the fin. In some earlier works, transient closed form solutions were developed for fin with assumed constant thermal properties. Chapman [50] studied the transient behavior of an annular fin of uniform thickness subjected to a sudden step change in the base temperature. Few years later, Donaldson and Shouman [51] presented a study on the transient temperature distribution in a straight fin for a step change in base temperature and a step change in base heat flow rate. Also, in a subsequent works, Suryanarayana [52,53] investigated the transient response of straight fins of constant cross-sectional area. Mao and Rooke [54] utilized Laplace transform method to analyze straight fins for different cases of a step change in base temperature, a step change in base heat flux and a step change in fluid temperature. Method of Green's functions was adopted by Beck *et al.* [55] to study transient behavior of fins of constant cross-section area. In an earlier work, Kim [56] developed an approximate solution to the transient heat transfer in straight fins of constant cross-sectional area and constant physical and thermal properties. Three years later, Aziz and Na [57] examined the transient response of a semi-infinite fin of uniform thickness, initially at the ambient temperature, subjected to a step change in temperature at its base, with fin cooling governed by a power-law type dependence on temperature difference. In another work, Aziz and Kraus [58] presented a variety of analytical results for transient fins, developed by separation of variable and Laplace transform techniques. Campo and Salazar [59] explored the analogy between the transient conduction in a planar slab for short times and the steady state conduction in a straight fin of uniform cross-section. Saha and Acharya [60] submitted a detailed parametric analysis of the unsteady three-dimensional flow and heat transfer in a pin-fin heat exchanger. Furthermore, several numerical studies of transient fins combined with complicating factors, such as natural convection [61, 62], spatial arrays of fins [63, 64] and phase change materials [65] have been presented. Mutlu and Al-Shemmeri [66] studied a longitudinal array of straight fins suddenly heated at the base.

In the above reviewed studies, heat dissipation from the fin tip has been assumed negligible. Therefore, the analyses of the reviewed works were based on fins with insulated tips or negligible heat transfer at the tips. However, effects of fin tip on the thermal response and performance of the fin have been pointed out in some few studies in literature. In such studies, Irej [67], Laor and Kalman [68], Lau and Tau [69] and Ünal [70] examined fins that dissipate heat also by their tips with constant or various temperature-dependence heat coefficients under steady state conditions.

Sequel to the above, there have been various studies on the thermal analysis of fin. However, there are limited studies in literatures on the applications of finite element methods for transient heat transfer analysis of fin with convective tip and under the influence of magnetic field. Therefore, in this present study, Galerkin finite element method is used to study the transient thermal behavior of convective-radiative fin with convective tip and under the influence of magnetic field. The inherent advantages, wide range of applications and high level of accuracy of the method justify the consideration of the method for the problem under consideration. FEM is geometrically flexible and it enjoys an advantage in memory use and speed for large problems. It can handle Neumann boundary condition as readily as the Dirichlet boundary condition as demonstrated in the present study. Of all the numerical methods developed so far, the finite-element method has been found to be the most general method, not only to solve the problems of heat transfer but also to solve various problems in different areas of engineering and science. Finite element method provides superior versatility to other numerical methods and is generally very stable with excellent convergence characteristics. To the best of the authors' knowledge, the transient analysis of heat transfers in convective-radiative cooling fin with convective tip and subjected to magnetic field using finite element method has not been studied in open literature. As part of the aims of the present paper, a step-by-step finite element analysis is presented in this work. The numerical solutions are used to investigate the effects of convective, radiative, magnetic and convective tip parameters on the transient thermal performance of the cooling fin. Also, effect the thermal stability values for the various multi-boiling heat transfer modes are established.

## 2. Problem formulation

Consider a straight fin of length  $L$  and thickness  $t$  which is exposed on both faces to a convective-radiative environment at temperature  $T_{\infty}$  and subjected to a uniform magnetic field as shown in Fig.1. In order to develop the mathematical model governing the thermal behavior, the following assumptions are made:

- I. The fin material is homogeneous and isotropic and with constant physical properties.
- II. The thermal properties of the fin, surrounding medium and the magnetic field vary with temperature according to power-law. The temperature of the surrounding fluid is uniform.
- III. The heat flow to or from the fin surface at any point is directly proportional to the temperature difference between the surface at that point and the surrounding fluid.
- IV. The fin thickness is so small compared to its height and length that temperature gradients normal to the surface (across the fin thickness) may be neglected. Therefore, the temperature variation inside the fin is one-dimensional i.e. temperature varies along the fin length only. heat loss through the fin edges is negligible compared to that which passes through the sides.
- V. There is no contact resistance where the base of the fin joins the prime surface. Also, the temperature of the base of the fin is uniform

VI. There are no heat sources or internal heat generation within the fin.

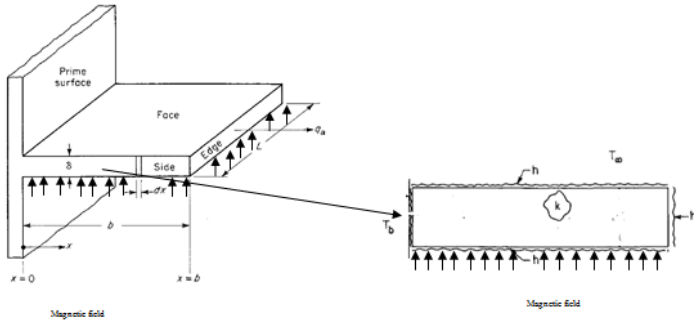


Fig. 1 (a) Schematic of longitudinal fin subjected to magnetic field (b) Computational domain of the fin

Based on following the above assumptions, the thermal energy balance could be expressed

$$q_x - \left( q_x + \frac{\delta q}{\delta x} dx \right) = h(T)P(T - T_\infty)dx + \sigma \varepsilon(T)P(T^4 - T_\infty^4)dx + \frac{J_c \times J_c}{\sigma} dx + \rho A_{cr} c_p \frac{\partial T}{\partial t} dx \quad (1)$$

Where;

$$J_c = \sigma(E + V \times B) \quad (2)$$

As  $dx \rightarrow 0$ , Eq. (1) reduces

$$-\frac{dq}{dx} = h(T)P(T - T_a) + \sigma \varepsilon(T)P(T^4 - T_a^4) + \frac{J_c \times J_c}{\sigma} + \rho A_{cr} c_p \frac{\partial T}{\partial t} \quad (3)$$

From Fourier's law of heat conduction, the rate of heat conduction in the fin is given by

$$q = -kA_{cr} \frac{dT}{dx} \quad (4)$$

Following, the radiation heat transfer rate is

$$q = -kA_{cr} \frac{dT}{dx} \quad (4)$$

$$q = -\frac{4\sigma A_{cr}}{3\beta_R} \frac{dT^4}{dx} \quad (5)$$

Therefore, the total rate of heat transfer is given by;

$$q = -kA_{cr} \frac{dT}{dx} - \frac{4\sigma A_{cr}}{3\beta_R} \frac{dT^4}{dx} \quad (6)$$

On substituting Eq. (6) into Eq. (3), one gets

$$\frac{d}{dx} \left( kA_{cr} \frac{dT}{dx} + \frac{4\sigma A_{cr}}{3\beta_R} \frac{dT^4}{dx} \right) = h(T)P(T - T_\infty) + \sigma(T)\varepsilon P(T^4 - T_\infty^4) + \frac{J_c \times J_c}{\sigma} + \rho A_{cr} c_p \frac{\partial T}{\partial t} \tag{7}$$

Further simplification of Eq. (7) gives the governing differential equation for the fin as

$$\frac{d^2T}{dx^2} + \frac{4\sigma}{3\beta_R k} \frac{d}{dx} \left( \frac{dT^4}{dx} \right) - \frac{h(T)P}{kA_{cr}} (T - T_\infty) - \frac{\sigma\varepsilon(T)P}{kA_{cr}} (T^4 - T_\infty^4) - \frac{J_c \times J_c}{\sigma k A_{cr}} = \frac{\rho c_p}{k} \frac{\partial T}{\partial t} \tag{8}$$

The initial and boundary conditions are

$$\begin{aligned} t = 0, \quad 0 < x < b, \quad T = T_b, \\ t > 0, \quad x = 0, \quad T = T_b, \\ t > 0, \quad x = b, \quad -k \frac{dT}{dx} = h(T - T_\infty) \end{aligned} \tag{9a}$$

However, if the tip of the fin is assumed insulated or a negligible rate of heat transfer from it, we have

$$t > 0, \quad x = b, \quad \frac{dT}{dx} = 0 \tag{9b}$$

It should be noted that

$$\frac{J_c \times J_c}{\sigma} = \sigma_m B_o^2 u^2 \tag{10}$$

After substitution of Eq. (10) into Eq. (8),

$$\frac{d^2T}{dx^2} + \frac{4\sigma}{3\beta_R k} \frac{d}{dx} \left( \frac{dT^4}{dx} \right) - \frac{h(T)P}{kA_{cr}} (T - T_\infty) - \frac{\sigma\varepsilon(T)P}{kA_{cr}} (T^4 - T_\infty^4) - \frac{\sigma_m(T)B_o^2 u^2}{kA_{cr}} (T - T_\infty) = \frac{\rho c_p}{k} \frac{\partial T}{\partial t} \tag{11}$$

The first case that is considered in this work is a situation where small temperature difference exists within the fin material during the heat flow. This actually necessitated the use of temperature-invariant physical and thermal properties of the fin. Also, it has been established that under such scenario, the term  $T^4$  can be expressed as a linear function of temperature. Therefore, we have

$$T^4 = T_\infty^4 + 4T_\infty^3(T - T_\infty) + 6T_\infty^2(T - T_\infty)^2 + \dots \cong 4T_\infty^3 T - 3T_\infty^4 \tag{12}$$

Also, using Rosseland's approximation

$$\frac{4\sigma}{3\beta_R k} \frac{\partial T^4}{\partial x} \cong \frac{16\sigma T_\infty^3}{3\beta_R k} \frac{\partial T}{\partial x} \tag{13}$$

On substituting Eqs. (15) and (16) into Eq. (14), we arrived at

$$\frac{d^2T}{dx^2} + \frac{16\sigma}{3\beta_R k} \frac{dT}{dx} - \frac{h(T)P}{kA_{cr}} (T - T_\infty) - \frac{4\sigma P \varepsilon(T) T_\infty^3}{kA_{cr}} (T - T_\infty) - \frac{\sigma_m(T)B_o^2 u^2}{kA_{cr}} (T - T_\infty) = \frac{\rho c_p}{k} \frac{\partial T}{\partial t} \tag{14}$$

However, for most industrial applications the heat transfer coefficient may be given as the power law [2,19], where the exponent  $p$  and  $h_o$  are constants. The constant  $p$  may vary

between -6.6 and 5. However, in most practical applications it lies between -3 and 3 [19]. So, the power temperature-dependent thermal properties of the surrounding fluid and the magnetic field are defined as

$$h(T) = h_o \left( \frac{T - T_\infty}{T_b - T_\infty} \right)^p \tag{15}$$

Extending the same power temperature-dependent relationship to the fin emissivity and the magnetic field, we have

$$\varepsilon(T) = \varepsilon_o \left( \frac{T - T_\infty}{T_b - T_\infty} \right)^q \tag{16}$$

$$\sigma_m(T) = (\sigma_m)_o \left( \frac{T - T_\infty}{T_b - T_\infty} \right)^r \tag{17}$$

The exponent  $p$  on the heat transfer coefficient represents laminar film boiling or condensation when  $p = -1/4$ , laminar natural convection when  $p = 1/4$ , turbulent natural convection when  $p = 1/3$ , nucleate boiling when  $p = 2$ , radiation when  $p = 3$ .  $p = 0$  implies a constant heat transfer coefficient.

Substitution of Eq. (16) - (17) gives

$$\frac{d^2T}{dx^2} + \frac{16\sigma}{3\beta_R k} \frac{d^2T}{dx^2} - \frac{h_o P (T - T_\infty)^{p+1}}{k A_{cr} (T_b - T_\infty)^p} - \frac{4\sigma \varepsilon_o P T_\infty^3 (T - T_\infty)^{q+1}}{k A_{cr} (T_b - T_\infty)^q} - \frac{\sigma_{m,o} B_o^2 u^2 (T - T_\infty)^{r+1}}{k A_{cr} (T_b - T_\infty)^r} = \frac{\rho c_p}{k} \frac{\partial T}{\partial t} \tag{18}$$

For constant thermal properties of the surrounding fluid and the magnetic field, we have a linear equation of the form

$$\frac{d^2T}{dx^2} + \frac{16\sigma}{3\beta_R k} \frac{d^2T}{dx^2} - \frac{hP(T - T_\infty)}{k A_{cr}} - \frac{4\sigma \varepsilon P T_\infty^3 (T - T_\infty)}{k A_{cr}} - \frac{\sigma_m B_o^2 u^2 (T - T_\infty)}{k A_{cr}} = \frac{\rho c_p}{k} \frac{\partial T}{\partial t} \tag{19}$$

It should be noted that the above Eq. (19) can be solved analytically. Using Laplace transform, it can easily be shown that the exact analytical solution of the equation based on the boundary conditions in Eq. (9) is given as;

$$T = T_\infty + (T_b - T_\infty) \left\{ \frac{\left( \frac{(hP+4\sigma \varepsilon T_\infty^3 P + \sigma_m B_o^2 u^2)L}{A_{cr} \left( k + \frac{16\sigma}{3\beta_R} \right)} \right) \cosh \left( \frac{(hP+4\sigma \varepsilon T_\infty^3 P + \sigma_m B_o^2 u^2)L}{A_{cr} \left( k + \frac{16\sigma}{3\beta_R} \right)} \right) (L-x) + \left( \frac{hL}{k} \right) \sinh \left( \frac{(hP+4\sigma \varepsilon T_\infty^3 P + \sigma_m B_o^2 u^2)L}{A_{cr} \left( k + \frac{16\sigma}{3\beta_R} \right)} \right) (L-x)}{\left( \frac{(hP+4\sigma \varepsilon T_\infty^3 P + \sigma_m B_o^2 u^2)L}{A_{cr} \left( k + \frac{16\sigma}{3\beta_R} \right)} \right) \cosh \left( \frac{(hP+4\sigma \varepsilon T_\infty^3 P + \sigma_m B_o^2 u^2)L}{A_{cr} \left( k + \frac{16\sigma}{3\beta_R} \right)} \right) + \left( \frac{hL}{k} \right) \sinh \left( \frac{(hP+4\sigma \varepsilon T_\infty^3 P + \sigma_m B_o^2 u^2)L}{A_{cr} \left( k + \frac{16\sigma}{3\beta_R} \right)} \right)} \right\} - 2 \sum_{n=1}^{\infty} \left\{ \frac{\lambda_n^3 \sin \left( \frac{\lambda_n x}{L} \right) \left\{ \exp - \left[ \lambda_n^2 + \left( \frac{(hP+4\sigma \varepsilon T_\infty^3 P + \sigma_m B_o^2 u^2)L}{A_{cr} \left( k + \frac{16\sigma}{3\beta_R} \right)} \right)^2 \right] \left( \frac{\left( k + \frac{16\sigma}{3\beta_R} \right) t}{\rho c_p L^2} \right) \right\}}{\left( \lambda_n^2 + \left( \frac{(hP+4\sigma \varepsilon T_\infty^3 P + \sigma_m B_o^2 u^2)L}{A_{cr} \left( k + \frac{16\sigma}{3\beta_R} \right)} \right)^2 \right) \left( \left( \frac{hL}{k} \right)^2 + \left( \frac{(hP+4\sigma \varepsilon T_\infty^3 P + \sigma_m B_o^2 u^2)L}{A_{cr} \left( k + \frac{16\sigma}{3\beta_R} \right)} \right)^2 \right) + \frac{hL}{k} \sin^2 \lambda_n} \right\} \tag{20a}$$

For the insulated tip, we have

$$T = T_\infty + (T_b - T_\infty) \left\{ \frac{\left( \frac{(hP+4\sigma\varepsilon T_\infty^3 P + \sigma_m B_0^2 u^2)L}{A_{cr} \left(k + \frac{16\sigma}{3\beta_R}\right)} \right) \cosh\left( \frac{(hP+4\sigma\varepsilon T_\infty^3 P + \sigma_m B_0^2 u^2)L}{A_{cr} \left(k + \frac{16\sigma}{3\beta_R}\right)} \right) (L-x)}{\left( \frac{(hP+4\sigma\varepsilon T_\infty^3 P + \sigma_m B_0^2 u^2)L}{A_{cr} \left(k + \frac{16\sigma}{3\beta_R}\right)} \right) \cosh\left( \frac{(hP+4\sigma\varepsilon T_\infty^3 P + \sigma_m B_0^2 u^2)L}{A_{cr} \left(k + \frac{16\sigma}{3\beta_R}\right)} \right)} - 2 \sum_{n=1}^{\infty} \frac{\left\{ \lambda_n^3 \sin\left(\frac{\lambda_n x}{L}\right) \exp\left[-\left(\lambda_n^2 + \left(\frac{(hP+4\sigma\varepsilon T_\infty^3 P + \sigma_m B_0^2 u^2)L}{A_{cr} \left(k + \frac{16\sigma}{3\beta_R}\right)}\right)^2\right) \left(\frac{k + \frac{16\sigma}{3\beta_R}}{\rho c_p L^2}\right) t\right]\right\}}{\left(\lambda_n^2 + \left(\frac{(hP+4\sigma\varepsilon T_\infty^3 P + \sigma_m B_0^2 u^2)L}{A_{cr} \left(k + \frac{16\sigma}{3\beta_R}\right)}\right)^2\right) \left(\frac{(hP+4\sigma\varepsilon T_\infty^3 P + \sigma_m B_0^2 u^2)L}{A_{cr} \left(k + \frac{16\sigma}{3\beta_R}\right)}\right)^2} \sin^2 \lambda_n \right\} \quad (20b)$$

where  $\lambda_n$  are the positive roots of the characteristic's equation

$$\lambda_n \cos \lambda_n + \left(\frac{hL}{k}\right) \sin \lambda_n = 0 \quad (21a)$$

It should be noted that a steady state is attained when  $t \rightarrow \infty$

For the sake of convenience in subsequent analysis, it should be noted that “ $b$ ” has been replaced with “ $L$ ” in the above analytical solution.

### 3. Finite Element Method for the Transient Analysis

It is very difficult to develop exact analytical solution to the nonlinear equation in Eq. (14) or Eq. (18). Therefore, Galerkin finite element method is used in this work to solve the nonlinear equation. The procedures of the numerical method are outlined as follows:

- I. **Finite element discretization:** The whole domain is divided into a finite number of sub-domains, designated as the discretization of the domain. Each sub-domain is called an element. The collection of elements comprises the finite-element mesh.
- II. **Generation of the element equations:** From the mesh, a typical element is isolated and the variational formulation of the given problem over the typical element is constructed. An approximate solution of the variational problem is assumed and the element equations are generated by substituting the assumed solution in the formulation. The element matrix, which is called stiffness matrix, is constructed by using the element interpolation functions.
- III. **Assembly of element equations:** The algebraic equations obtained from the element matrix are assembled by imposing the inter-element continuity conditions. This yields a large number of algebraic equations known as the global finite element model, which governs the whole domain.
- IV. **Imposition of boundary conditions:** The essential and natural boundary conditions as given in the problem under consideration are imposed on the assembled equations.
- V. **Solution of assembled equation:** The assembled equations after the imposition of the boundary conditions are solved by any numerical technique that is developed for solving systems of linear equations. The numerical techniques are

Gaussian elimination method, Gauss-Jordan iterative method, Gauss-Jacobi iterative method, Gauss-Seidel iterative method, LU decomposition method, Choleski decomposition, Crout's method, Householder's technique, etc.

In order to demonstrate the application of the finite element method to the present nonlinear problem, a weak formulation of the nonlinear governing differential equation is derived using Galerkin finite element method. For the purpose of the finite element analysis, one can rewrite Eq. (14) as;

$$\left(k + \frac{16\sigma}{3\beta_R}\right) \frac{d^2T}{dx^2} - \left(\frac{(h(T)P + 4\sigma(T)P\varepsilon_o T_\infty^3 + \sigma_m(T)B_o^2 u^2)}{A_{cr}}\right) (T - T_\infty) - \rho c_p \frac{\partial T}{\partial t} = 0 \tag{21b}$$

where temperature-dependent thermal properties of the surrounding fluid and the magnetic field are defined in Eqs. (15) – (17). Using the shape/interpolating function on the governing equation and Integrating over the domain V of the control volume according to Galerkin finite element method, we have

$$\int_V W \left( \left(k + \frac{16\sigma}{3\beta_R}\right) \frac{d^2T}{dx^2} - \left(\frac{(h(T)P + 4\sigma(T)P\varepsilon_o T_\infty^3 + \sigma_m(T)B_o^2 u^2)}{A_{cr}}\right) (T - T_\infty) - \rho c_p \frac{\partial T}{\partial t} = 0 \right) dV = 0 \tag{22}$$

For the one-dimensional problem which the dependent variable varies only along x-axis and the boundary integrals turn to be a point value on the boundaries, one can replace,  $dV$  by  $A_{cr}dx$  in the Eq. (22). Here,  $A_{cr}$  is the uniform cross-sectional area of the fin and P is the perimeter of the fin from which convection takes place.

$$\int_L W \left( \left(k + \frac{16\sigma}{3\beta_R}\right) \frac{d^2T}{dx^2} - \left(\frac{(h(T)P + 4\sigma(T)P\varepsilon_o T_\infty^3 + \sigma_m(T)B_o^2 u^2)}{A_{cr}}\right) (T - T_\infty) - \rho c_p \frac{\partial T}{\partial t} = 0 \right) A_{cr} dx = 0 \tag{23}$$

After expansion, one arrives at

$$\int_L W \left( \left(k + \frac{16\sigma}{3\beta_R}\right) \frac{\partial^2 T}{\partial x^2} A_{cr} dx \right) - \int_L ((h(T)P + 4\sigma(T)\varepsilon_o T_\infty^3)P)(T - T_\infty) dx - \int_L \sigma_m(T)B_o^2 u^2 (T - T_\infty) dx - \int_L \rho c \frac{\partial T}{\partial t} A_{cr} dx = 0 \tag{24}$$

For the fin of length, L

$$\int_0^L W \left( \left(k + \frac{16\sigma}{3\beta_R}\right) A_{cr} \frac{\partial^2 T}{\partial x^2} - ((h(T)P + 4\sigma(T)\varepsilon_o T_\infty^3)P)(T - T_\infty) - \sigma_m(T)B_o^2 u^2 (T - T_\infty) - \rho c A_{cr} \frac{\partial T}{\partial t} \right) dx = 0 \tag{25}$$

The expansion of Eq. (24) gives

$$\underbrace{\int_0^L W \left(k + \frac{16\sigma}{3\beta_R}\right) A_{cr} \frac{\partial}{\partial x} \left[\frac{\partial T}{\partial x}\right] dx}_{(1)} - \underbrace{\left[ \int_0^L (h(T) + 4\sigma(T)\varepsilon_o T_\infty^3) P W T dx + \int_0^L \sigma_m(T) B_o^2 u^2 W T dx \right]}_2 - \underbrace{\left[ \int_0^L (h(T) + 4\sigma(T)\varepsilon_o T_\infty^3) P T_\infty W dx - \int_0^L \sigma_m(T) B_o^2 u^2 W T_\infty dx \right]}_2 = 0 \tag{26}$$

$$\underbrace{\int_0^L \rho c_p A_{cr} W \frac{\partial T}{\partial t} dx}_{3} = 0$$

For the term (1) in Eq. (26), one can write

$$\int_0^L W \left( k + \frac{16\sigma}{3\beta_R} \right) A_{cr} \frac{\partial}{\partial x} \left( \frac{\partial T}{\partial x} \right) dx = \left( k + \frac{16\sigma}{3\beta_R} \right) A_{cr} \int_0^L W \partial \left( \frac{\partial T}{\partial x} \right) \tag{27}$$

Applying integration by part  $\left( \int_0^L u \partial v = uv|_0^L - \int_0^L v \partial u \right)$  to Eq. (27), where;

$$= W \Rightarrow \frac{\partial u}{\partial x} = \frac{\partial W}{\partial x} \text{ and } \partial v = \partial \left( \frac{\partial T}{\partial x} \right) \Rightarrow v = \frac{\partial T}{\partial x} u \tag{28}$$

Applying Eq. (28) in Eq. (27), gives

$$\begin{aligned} \int_0^L \left( k + \frac{16\sigma}{3\beta_R} \right) A_{cr} W \frac{\partial}{\partial x} \left( \frac{\partial T}{\partial x} \right) dx &= \left( k + \frac{16\sigma}{3\beta_R} \right) A_{cr} \int_0^L W \partial \left( \frac{\partial T}{\partial x} \right) \\ &= \left( k + \frac{16\sigma}{3\beta_R} \right) A_{cr} \left\{ W \frac{\partial T}{\partial x} \Big|_0^L - \int_0^L \frac{\partial W}{\partial x} \frac{\partial T}{\partial x} dx \right\} \end{aligned} \tag{29}$$

Substituting Eq. (29) into Eq. (26), leads to

$$\begin{aligned} A_{cr} \left( k + \frac{16\sigma}{3\beta_R} \right) \frac{\partial T}{\partial x} \Big|_0^L W - \int_0^L \left( k + \frac{16\sigma}{3\beta_R} \right) A_{cr} \frac{\partial W}{\partial x} \frac{\partial T}{\partial x} dx \\ - \left[ \int_0^L (h(T) + 4\sigma(T)\epsilon_o T_\infty^3) PWT dx + \int_0^L \sigma_m(T) B_o^2 u^2 WT dx \right. \\ \left. - \int_0^L (h(T) + 4\sigma(T)\epsilon_o T_\infty^3) PT_\infty W dx - \int_0^L \sigma_m(T) B_o^2 u^2 WT_\infty dx \right] - \int_0^L \rho c_p A_{cr} W \frac{\partial T}{\partial t} dx = 0 \end{aligned} \tag{30}$$

Eq. (30) can be written as

$$\begin{aligned} \int_0^L \rho c_p A_{cr} W \frac{\partial T}{\partial t} dx + \int_0^L \left( k + \frac{16\sigma}{3\beta_R} \right) A_{cr} \frac{\partial W}{\partial x} \frac{\partial T}{\partial x} dx + \int_0^L (h(T) + 4\sigma(T)\epsilon_o T_\infty^3) PWT dx \\ + \int_0^L \sigma_m(T) B_o^2 u^2 WT dx \\ = \int_0^L (h(T) + 4\sigma(T)\epsilon_o T_\infty^3) PT_\infty W dx + \int_0^L \sigma_m(T) B_o^2 u^2 WT_\infty dx + A_{cr} \left( k + \frac{16\sigma}{3\beta_R} \right) \frac{\partial T}{\partial x} \Big|_0^L W \end{aligned} \tag{31}$$

The above Eq. (31) is a weak formulation of the nonlinear governing differential equation.

In order to carry out the finite element discretization as stated in the step 1 of the finite element analysis, the whole domain is divided into a finite number of sub-domains as shown in Fig. 2. For a one-dimensional problem, linear elements are used. The finite element discretization is done in a way such that the given length of the body is divided into number of divisions, say 'n' elements which consequently, gives (n + 1) nodes to represent the body as shown in Table 1.

Table 1. Element and node numbers of linear one-dimensional elements

Element No.	Node <i>i</i>	Node <i>j</i>
1	1	2
2	2	3
3	3	4
<i>e</i>	<i>i</i>	<i>j</i>
<i>n</i>	<i>n</i>	<i>n+1</i>

Table 2. Element and node numbers of linear one-dimensionalelements used in this study

Element No.	Node <i>i</i>	Node <i>j</i>
1	1	2
2	2	3
3	3	4
.	.	.
.	.	.
48	48	49
49	49	50
50	50	51

In the finite element analysis of the present problem (one-dimension transient state), 2-node linear elements are used and the given length of the fin is divided into 50 elements which give 51 nodes to represent the total length of the fin as shown in Table 2 and Fig. 2.

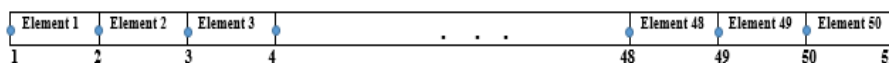


Fig. 2. Finite element

In order to construct a variational formulation of the given problem over an element, a typical element is isolated (Fig. 3) from the mesh shown in Fig. 2. The typical 2-node linear element with end nodes '*i*' and '*j*' having the corresponding temperature being denoted by *T<sub>i</sub>* and *T<sub>j</sub>*, respectively is shown in Fig. 3.

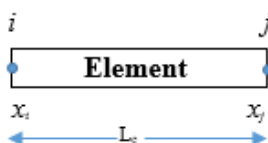


Fig. 3. A 2-node element

For the 2-node element, the following analysis for the variational formulation is carried out. Following Eq. (31), it could be stated that the weak form formulation of the governing Equation for an element of length "*L<sub>e</sub>*" is given as

$$\begin{aligned}
 & \int_0^{L_e} \rho c_p A_{cr} W \frac{\partial T}{\partial t} dx + \int_0^{L_e} \left( k + \frac{16\sigma}{3\beta_R} \right) A_{cr} \frac{\partial W}{\partial x} \frac{\partial T}{\partial x} dx + \int_0^{L_e} (h(T) + 4\sigma(T)\epsilon_o T_o^3) P W T dx \\
 & \quad + \int_0^{L_e} \sigma_m(T) B_o^2 u^2 W T dx \tag{32} \\
 & = \int_0^{L_e} (h(T) + 4\sigma(T)\epsilon_o T_o^3) P T_o W dx + \int_0^{L_e} \sigma_m(T) B_o^2 u^2 W T_o dx + A_{cr} \left( k + \frac{16\sigma}{3\beta_R} \right) \frac{\partial T}{\partial x} \Big|_0^{L_e} W
 \end{aligned}$$

The linear temperature variation in the element is represented by

$$T = \lambda_1 + \lambda_2 x \tag{33}$$

where  $T$  is the temperature at any location  $x$  and the parameters  $\lambda_1$  and  $\lambda_2$  are constants. Since there are two arbitrary constants in the linear representation, it requires only two nodes to determine the values of  $\lambda_1$  and  $\lambda_2$ . Thus, we have

$$T_i = \lambda_1 + \lambda_2 x_i \tag{34a}$$

$$T_j = \lambda_1 + \lambda_2 x_j \tag{34b}$$

On solving Eq. (34a) and (34b), we have

$$\lambda_1 = \frac{T_i x_j - T_j x_i}{x_j - x_i}, \quad \lambda_2 = \frac{T_j - T_i}{x_j - x_i} \tag{35}$$

After substituting the values of  $\lambda_1$  and  $\lambda_2$  in Eq. (35) into Equ. (33), one arrives at

$$T = T_i \left( \frac{x_j - x}{x_j - x_i} \right) + T_j \left( \frac{x - x_i}{x_j - x_i} \right) \tag{36}$$

The above Eq. (36) can be written as

$$T = T_i W_i + T_j W_j = [W_i \quad W_j] \begin{Bmatrix} T_i \\ T_j \end{Bmatrix} \tag{37}$$

Where

$$W_i = \frac{x_j - x}{x_j - x_i}, \quad W_j = \frac{x - x_i}{x_j - x_i} \tag{38}$$

$W_i$  and  $W_j$  are called shape/interpolation/test/basis functions. Furthermore, one can write Equ. (37) as;

$$T = [W] \{T\} \tag{39}$$

Where;

$$[W] = [W_i \quad W_j] \tag{40}$$

is the shape function matrix and

$$\{T\} = \begin{Bmatrix} T_i \\ T_j \end{Bmatrix} \tag{41}$$

is the vector of unknown temperatures taking

$$x_i = 0, \quad x_j = L_e, \quad \Rightarrow x_j - x_i = L_e \tag{42}$$

Substitute Eq. (42) into Eq. (38), we have the shape functions as;

$$W_i = 1 - \frac{x}{L_e}, \quad W_j = \frac{x}{L_e} \tag{43}$$

On substituting Eq. (43) into Eq. (37), we can see that the temperature at any point “ $x$ ” in the 2-node element is approximated by;

$$T = \left(1 - \frac{x}{L_e}\right) T_i + \left(\frac{x}{L_e}\right) T_j \Rightarrow T = T_i W_i + T_j W_j = [W_i \quad W_j] \begin{Bmatrix} T_i \\ T_j \end{Bmatrix} = [W] \{T\} \tag{44}$$

Therefore

$$\frac{\partial T}{\partial t} = \left(1 - \frac{x}{L_e}\right) \frac{\partial T_i}{\partial t} + \left(\frac{x}{L_e}\right) \frac{\partial T_j}{\partial t} \Rightarrow \frac{\partial T}{\partial t} = W_i \frac{\partial T_i}{\partial t} + W_j \frac{\partial T_j}{\partial t} = [W_i \quad W_j] \left\{ \begin{array}{c} \frac{\partial T_i}{\partial t} \\ \frac{\partial T_j}{\partial t} \end{array} \right\} = [\mathbf{W}] \left\{ \frac{\partial \mathbf{T}}{\partial t} \right\} \quad (45)$$

$$\frac{\partial T}{\partial x} = \frac{\partial T}{\partial x} = \frac{\partial W_i}{\partial x} T_i + \frac{\partial W_j}{\partial x} T_j = \left(-\frac{1}{L_e}\right) T_i + \left(\frac{1}{L_e}\right) T_j = \frac{1}{L_e} (T_j - T_i) \Rightarrow T = \left[ -\frac{1}{L_e} \quad \frac{1}{L_e} \right] \left\{ \begin{array}{c} T_i \\ T_j \end{array} \right\} = [\mathbf{B}] \{\mathbf{T}\} \quad (46)$$

Where;

$$[\mathbf{B}] = \left[ \begin{array}{cc} \frac{\partial W_i}{\partial x} & \frac{\partial W_j}{\partial x} \end{array} \right] \quad (47)$$

After substitution of Eq. (44), (45), (46) and (47) into Eq. (32), we have

$$\begin{aligned} & \int_0^{L_e} \rho c_p A_{cr} \left[ \begin{array}{c} W_i \\ W_j \end{array} \right] [W_i \quad W_j] \left\{ \begin{array}{c} \frac{\partial T_i}{\partial t} \\ \frac{\partial T_j}{\partial t} \end{array} \right\} dx + \int_0^{L_e} \left( k + \frac{16\sigma}{3\beta_R} \right) A_{cr} \left[ \begin{array}{c} \frac{\partial W_i}{\partial x} \\ \frac{\partial W_j}{\partial x} \end{array} \right] \left[ \frac{\partial W_i}{\partial x} \quad \frac{\partial W_j}{\partial x} \right] \left\{ \begin{array}{c} T_i \\ T_j \end{array} \right\} dx \\ & + \int_0^{L_e} (h(T) + 4\sigma(T)\varepsilon_o T_\infty^3) P \left[ \begin{array}{c} W_i \\ W_j \end{array} \right] [W_i \quad W_j] \left\{ \begin{array}{c} T_i \\ T_j \end{array} \right\} dx \\ & + \int_0^{L_e} \sigma_m(T) B_o^2 u^2 \left[ \begin{array}{c} W_i \\ W_j \end{array} \right] [W_i \quad W_j] \left\{ \begin{array}{c} T_i \\ T_j \end{array} \right\} dx \\ & = \int_0^{L_e} (h(T) + 4\sigma(T)\varepsilon_o T_\infty^3) P T_\infty \left[ \begin{array}{c} W_i \\ W_j \end{array} \right] dx + \int_0^{L_e} \sigma_m(T) B_o^2 u^2 T_\infty \left[ \begin{array}{c} W_i \\ W_j \end{array} \right] dx \\ & + A_{cr} \left( k + \frac{16\sigma}{3\beta_R} \right) \frac{\partial T}{\partial x} \Big|_0^{L_e} \left[ \begin{array}{c} W_i \\ W_j \end{array} \right] \end{aligned} \quad (48)$$

Eq. (48) can be written as

$$\begin{aligned} & \int_0^{L_e} \rho c_p A_{cr} \left[ \begin{array}{c} W_i \\ W_j \end{array} \right]^T [W_i \quad W_j] \left\{ \begin{array}{c} \frac{\partial T_i}{\partial t} \\ \frac{\partial T_j}{\partial t} \end{array} \right\} dx \\ & + \int_0^{L_e} \left( k + \frac{16\sigma}{3\beta_R} \right) A_{cr} \left[ \begin{array}{c} \frac{\partial W_i}{\partial x} \\ \frac{\partial W_j}{\partial x} \end{array} \right]^T \left[ \frac{\partial W_i}{\partial x} \quad \frac{\partial W_j}{\partial x} \right] \left\{ \begin{array}{c} T_i \\ T_j \end{array} \right\} dx \\ & + \int_0^{L_e} (h(T) + 4\sigma(T)\varepsilon_o T_\infty^3) P \left[ \begin{array}{c} W_i \\ W_j \end{array} \right]^T [W_i \quad W_j] \left\{ \begin{array}{c} T_i \\ T_j \end{array} \right\} dx \\ & + \int_0^{L_e} \sigma_m(T) B_o^2 u^2 \left[ \begin{array}{c} W_i \\ W_j \end{array} \right]^T [W_i \quad W_j] \left\{ \begin{array}{c} T_i \\ T_j \end{array} \right\} dx \\ & = \int_0^{L_e} (h(T) + 4\sigma(T)\varepsilon_o T_\infty^3) P T_\infty \left[ \begin{array}{c} W_i \\ W_j \end{array} \right]^T dx + \int_0^{L_e} \sigma_m(T) B_o^2 u^2 T_\infty \left[ \begin{array}{c} W_i \\ W_j \end{array} \right]^T dx \\ & + A_{cr} \left( k + \frac{16\sigma}{3\beta_R} \right) \frac{\partial T}{\partial x} \Big|_0^{L_e} \left[ \begin{array}{c} W_i \\ W_j \end{array} \right]^T \end{aligned} \quad (49)$$

For the  $i$  and  $j$  nodes of an element, Eq. (49) can be written in a convenient form as

$$[C_{ij}] \left\{ \begin{array}{c} \frac{\partial T_i}{\partial t} \\ \frac{\partial T_j}{\partial t} \end{array} \right\} + [K_{ij}(T)] \left\{ \begin{array}{c} T_i \\ T_j \end{array} \right\} = [f_{ij}(T)] \quad (50)$$

Where

$$[C_{ij}] = \int_0^{L_e} \rho c_p A_{cr} \left[ \begin{array}{c} W_i \\ W_j \end{array} \right]^T [W_i \quad W_j] dx \quad (51)$$

$$[K_{ij}(T)] = \int_0^{L_e} \left( k + \frac{16\sigma}{3\beta_R} \right) A_{cr} \left[ \begin{array}{c} \frac{\partial W_i}{\partial x} \\ \frac{\partial W_j}{\partial x} \end{array} \right]^T \left[ \frac{\partial W_i}{\partial x} \quad \frac{\partial W_j}{\partial x} \right] dx \quad (52)$$

$$\begin{aligned}
 & + \int_0^{L_e} \sigma_m(T) B_o^2 u^2 [W_i \quad W_j]^T [W_i \quad W_j] dx \\
 [f_{ij}(T)] = & \int_0^{L_e} (h(T) + 4\sigma(T)\varepsilon_o T_\infty^3) P T_\infty [W_i \quad W_j]^T dx \\
 & + \int_0^{L_e} \sigma_m(T) B_o^2 u^2 T_\infty [W_i \quad W_j]^T dx \\
 & + A_{cr} \left( k + \frac{16\sigma}{3\beta_R} \right) \frac{\partial T}{\partial x} \Big|_0^{L_e} [W_i \quad W_j]^T,
 \end{aligned} \tag{53}$$

Alternatively, using the relationships in Eqs. (44) - (46), one can write Eq. (49) in a compact matrix form of as;

$$\begin{aligned}
 & \int_0^{L_e} \rho c_p A_{cr} [\mathbf{W}]^T [\mathbf{W}] \left\{ \frac{\partial \mathbf{T}}{\partial t} \right\} dx + \int_0^{L_e} \left( k + \frac{16\sigma}{3\beta_R} \right) A_{cr} [\mathbf{B}]^T [\mathbf{B}] [\mathbf{T}] dx \\
 & + \int_0^{L_e} (h(T) + 4\sigma(T)\varepsilon_o T_\infty^3) P [\mathbf{W}]^T [\mathbf{W}] [\mathbf{T}] dx + \int_0^{L_e} \sigma_m(T) B_o^2 u^2 [\mathbf{W}]^T [\mathbf{W}] [\mathbf{T}] dx \\
 = & \int_0^{L_e} (h(T) + 4\sigma(T)\varepsilon_o T_\infty^3) P [\mathbf{W}]^T T_\infty dx + \left( A_{cr} \left( k + \frac{16\sigma}{3\beta_R} \right) \frac{\partial T}{\partial x} \right) \Big|_0^{L_e} [\mathbf{W}]^T
 \end{aligned} \tag{54}$$

Eq. (54) can be written form as;

$$[\mathbf{C}] \left\{ \frac{\partial \mathbf{T}}{\partial t} \right\} + [\mathbf{K}(T)] \{\mathbf{T}\} = [\mathbf{f}(T)] \tag{55}$$

Where

$$[\mathbf{C}] = \int_0^{L_e} \rho c_p A [\mathbf{W}]^T [\mathbf{W}] dx \tag{56}$$

$$\begin{aligned}
 [\mathbf{K}(T)] = & \int_0^{L_e} \left( k + \frac{16\sigma}{3\beta_R} \right) A_{cr} [\mathbf{B}]^T [\mathbf{B}] dx + \int_0^{L_e} (h(T) + 4\sigma(T)\varepsilon_o T_\infty^3) P [\mathbf{W}]^T [\mathbf{W}] dx \\
 & + \int_0^{L_e} \sigma_m(T) B_o^2 u^2 [\mathbf{W}]^T [\mathbf{W}] dx
 \end{aligned} \tag{57}$$

$$\begin{aligned}
 [\mathbf{f}(T)] = & \int_0^{L_e} (h(T) + 4\sigma(T)\varepsilon_o T_\infty^3) P T_\infty [\mathbf{W}]^T T_\infty dx + \int_0^{L_e} \sigma_m(T) B_o^2 u^2 T_\infty [\mathbf{W}]^T T_\infty dx \\
 & + A \left( \left( k + \frac{16\sigma}{3\beta_R} \right) \frac{\partial T}{\partial x} \right) \Big|_0^{L_e} [\mathbf{W}]^T
 \end{aligned} \tag{58}$$

In order to develop the matrix equation for the element, we need to expand Eq. (51) - (54) or the equivalent equations in Eq. (56) - (58). Therefore, the expansions are carried out as follows

$$[C_{ij}] = \int_0^{L_e} \rho c_p A_{cr} [W_i \quad W_j]^T [W_i \quad W_j] dx = \int_0^{L_e} \rho c_p A_{cr} \begin{bmatrix} W_i^2 & W_i W_j \\ W_i W_j & W_j^2 \end{bmatrix} dx, \tag{59}$$

$$\begin{aligned}
 [K_{ij}(T)] = & \int_0^{L_e} \left( k + \frac{16\sigma}{3\beta_R} \right) A_{cr} \begin{bmatrix} \left( \frac{\partial W_i}{\partial x} \right)^2 & \frac{\partial W_i}{\partial x} \frac{\partial W_j}{\partial x} \\ \frac{\partial W_i}{\partial x} \frac{\partial W_j}{\partial x} & \left( \frac{\partial W_j}{\partial x} \right)^2 \end{bmatrix} \begin{Bmatrix} T_i \\ T_j \end{Bmatrix} dx \\
 & + \int_0^{L_e} (h(T) + 4\sigma(T)\varepsilon_o T_\infty^3) P \begin{bmatrix} W_i^2 & W_i W_j \\ W_i W_j & W_j^2 \end{bmatrix} \begin{Bmatrix} T_i \\ T_j \end{Bmatrix} dx
 \end{aligned} \tag{60}$$

$$\begin{aligned}
 & + \int_0^{L_e} \sigma_m(T) B_o^2 u^2 \begin{bmatrix} W_i^2 & W_i W_j \\ W_i W_j & W_j^2 \end{bmatrix} \begin{Bmatrix} T_i \\ T_j \end{Bmatrix} dx \\
 [f_{ij}(T)] = & \int_0^{L_e} (h(T) + 4\sigma(T)\varepsilon_o T_\infty^3) P T_\infty \begin{bmatrix} W_i \\ W_j \end{bmatrix} dx
 \end{aligned} \tag{61}$$

$$+ \int_0^{L_e} \sigma_m(T) B_o^2 u^2 T_\infty \left[ \frac{W_i}{W_j} \right] dx + A_{cr} \left( k + \frac{16\sigma}{3\beta_R} \right) \frac{\partial T}{\partial x} \Big|_0^{L_e} \left[ \frac{W_i}{W_j} \right]$$

On substituting Eq. (43) into Eq. (46) into the above Eqs. (59) -(61), one arrives. For the global capacitance matrix, we have

$$[C_{ij}] = \int_0^{L_e} \rho c_p \begin{bmatrix} \left(1 - \frac{x}{L_e}\right)^2 & \left(1 - \frac{x}{L_e}\right) \left(\frac{x}{L_e}\right) \\ \left(1 - \frac{x}{L_e}\right) \left(\frac{x}{L_e}\right) & \left(\frac{x}{L_e}\right)^2 \end{bmatrix} dx \tag{62}$$

For the stiffness matrix;

$$\begin{aligned} [K_{ij}(T)] = & \int_0^{L_e} \left( k + \frac{16\sigma}{3\beta_R} \right) A_{cr} \begin{bmatrix} \left(-\frac{1}{L_e}\right)^2 & \left(-\frac{1}{L_e}\right) \left(\frac{1}{L_e}\right) \\ \left(-\frac{1}{L_e}\right) \left(\frac{1}{L_e}\right) & \left(\frac{1}{L_e}\right)^2 \end{bmatrix} dx \\ & + \int_0^{L_e} (h(T) + 4\sigma(T)\varepsilon_o T_\infty^3) P \begin{bmatrix} \left(1 - \frac{x}{L_e}\right)^2 & \left(1 - \frac{x}{L_e}\right) \left(\frac{x}{L_e}\right) \\ \left(1 - \frac{x}{L_e}\right) \left(\frac{x}{L_e}\right) & \left(\frac{x}{L_e}\right)^2 \end{bmatrix} dx \\ & + \int_0^{L_e} \sigma_m(T) B_o^2 u^2 \begin{bmatrix} \left(1 - \frac{x}{L_e}\right)^2 & \left(1 - \frac{x}{L_e}\right) \left(\frac{x}{L_e}\right) \\ \left(1 - \frac{x}{L_e}\right) \left(\frac{x}{L_e}\right) & \left(\frac{x}{L_e}\right)^2 \end{bmatrix} dx \end{aligned} \tag{63}$$

For the load vector

$$\begin{aligned} [f_i(T)] = & \int_0^{L_e} (h(T) + 4\sigma(T)\varepsilon_o T_\infty^3) P \begin{bmatrix} \left(1 - \frac{x}{L_e}\right) \\ \left(\frac{x}{L_e}\right) \end{bmatrix} T_\infty dx + \int_0^{L_e} \sigma_m(T) B_o^2 u^2 \begin{bmatrix} \left(1 - \frac{x}{L_e}\right) \\ \left(\frac{x}{L_e}\right) \end{bmatrix} T_\infty dx \\ & + A_{cr} \left( \left( k + \frac{16\sigma}{3\beta_R} \right) \frac{\partial T}{\partial x} \right) \Big|_0^{L_e} \begin{bmatrix} \left(1 - \frac{x}{L_e}\right) \\ \left(\frac{x}{L_e}\right) \end{bmatrix} \end{aligned} \tag{64}$$

After the integrations, we have the global capacitance matrix, stiffness matrix and the load vector as;

$$[C_{ij}] = \frac{\rho c_p A L_e}{6} \begin{bmatrix} 21 \\ 12 \end{bmatrix} \tag{65}$$

$$[K_{ij}(T)] = \left[ \frac{\left( k + \frac{16\sigma}{3\beta_R} \right) A_{cr}}{L_e} \begin{bmatrix} 1 & -1 \\ -1 & 1 \end{bmatrix} + \frac{(h(T) + 4\sigma(T)\varepsilon_o T_\infty^3) P L_e}{6} \begin{bmatrix} 21 \\ 12 \end{bmatrix} + \frac{\sigma_m(T) B_o^2 u^2 L_e}{6} \begin{bmatrix} 21 \\ 12 \end{bmatrix} \right] \tag{66}$$

$$[f_i(T)] = \frac{(h(T) + 4\sigma(T)\varepsilon_o T_\infty^3) P T_\infty L_e + \sigma_m(T) B_o^2 u^2 T_\infty L}{2} \begin{bmatrix} 1 \\ 1 \end{bmatrix} + \left( k + \frac{16\sigma}{3\beta_R} \right) A_{cr} \begin{bmatrix} -\frac{\partial T(0)}{\partial x} \\ \frac{\partial T(L_e)}{\partial x} \end{bmatrix} \tag{67}$$

Substitution Eq. (65) - (67) into Eq. (50), gives the characteristic equation over the space interval  $\Delta x$  as;

$$\frac{\rho c_p A L_e}{6} \begin{bmatrix} 21 \\ 12 \end{bmatrix} \left\{ \frac{\partial T_i}{\partial T} \right\} + \left[ \frac{\left( k + \frac{16\sigma}{3\beta_R} \right) A_{cr}}{L_e} \begin{bmatrix} 1 & -1 \\ -1 & 1 \end{bmatrix} + \frac{(h(T) + 4\sigma(T)\varepsilon_o T_\infty^3) P L_e}{6} \begin{bmatrix} 21 \\ 12 \end{bmatrix} \right] \tag{68}$$

$$= \frac{(h(T) + 4\sigma(T)\epsilon_o T_\infty^3)PT_\infty L_e}{2} \begin{bmatrix} 1 \\ 1 \end{bmatrix} + \frac{\sigma_m(T)B_o^2 u^2 T_\infty L_e}{2} \begin{bmatrix} 1 \\ 1 \end{bmatrix} + \left(k + \frac{16\sigma}{3\beta_R}\right) A_{cr} \begin{bmatrix} -\frac{\partial T(0)}{\partial x} \\ \frac{\partial T(L_e)}{\partial x} \end{bmatrix}$$

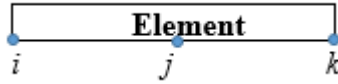


Fig. 4. A 3-node element

The steps above are general. Both the results and the analysis can be different if one uses 3-node element. Using a 3-node element, one arrives at

$$[C_{ij}] \begin{Bmatrix} \frac{\partial T_i}{\partial t} \\ \frac{\partial T_j}{\partial t} \\ \frac{\partial T_k}{\partial t} \end{Bmatrix} + [K_{ij}(T)] \begin{Bmatrix} T_i \\ T_j \\ T_k \end{Bmatrix} = [f_{ij}(T)] \tag{69}$$

Where;

$$[C_{ij}] = \frac{\rho c_p A_{cr} L_e}{6} \begin{bmatrix} 8 & 4 & -2 \\ 4 & 32 & 4 \\ -2 & 4 & 8 \end{bmatrix} \tag{70}$$

$$[K_{ij}(T)] = \left[ \frac{\left(k + \frac{16\sigma}{3\beta_R}\right) A_{cr}}{3L_e} \begin{bmatrix} 7 & -8 & 1 \\ -8 & 16 & -8 \\ 1 & -8 & 7 \end{bmatrix} \right. \tag{71}$$

$$\left. + (h(T)P + 4\sigma(T)\epsilon_o T_\infty^3 P + \sigma_m(T)B_o^2 u^2) \frac{L_e}{60} \begin{bmatrix} 8 & 4 & -2 \\ 4 & 32 & 4 \\ -2 & 4 & 8 \end{bmatrix} \right]$$

$$[f_i(T)] = (h(T)P + 4\sigma(T)\epsilon_o T_\infty^3 P + \sigma_m(T)B_o^2 u^2) \frac{T_\infty L_e}{6} \begin{bmatrix} 1 \\ 4 \\ 1 \end{bmatrix} + \left(k + \frac{16\sigma}{3\beta_R}\right) A_{cr} \begin{bmatrix} -\frac{\partial T(0)}{\partial x} \\ \frac{\partial T(M)}{\partial x} \\ \frac{\partial T(L)}{\partial x} \end{bmatrix} \tag{72}$$

After the substitution of Eqs. (69) - (72), we arrived at

$$\begin{aligned}
 & \frac{\rho c_p A_{cr} L_e}{6} \begin{bmatrix} 8 & 4 & -2 \\ 4 & 32 & 4 \\ -2 & 4 & 8 \end{bmatrix} \begin{Bmatrix} \frac{\partial T_i}{\partial t} \\ \frac{\partial T_j}{\partial t} \\ \frac{\partial T_k}{\partial t} \end{Bmatrix} \\
 & + \left[ \frac{\left(k + \frac{16\sigma}{3\beta_R}\right) A_{cr}}{3L_e} \begin{bmatrix} 7 & -8 & 1 \\ -8 & 16 & -8 \\ 1 & -8 & 7 \end{bmatrix} \right. \\
 & \left. + (h(T)P + 4\sigma(T)\varepsilon_o T_o^3 P + \sigma_m(T)B_o^2 u^2) \frac{L_e}{60} \begin{bmatrix} 8 & 4 & -2 \\ 4 & 32 & 4 \\ -2 & 4 & 8 \end{bmatrix} \right] \begin{Bmatrix} T_i \\ T_j \\ T_k \end{Bmatrix} \\
 & = (h(T)P + 4\sigma(T)\varepsilon_o T_o^3 P + \sigma_m(T)B_o^2 u^2) \frac{T_o L_e}{6} \begin{bmatrix} 1 \\ 4 \\ 1 \end{bmatrix} + \left(k + \frac{16\sigma}{3\beta_R}\right) A_{cr} \begin{bmatrix} -\frac{\partial T(0)}{\partial x} \\ \frac{\partial T(M)}{\partial x} \\ \frac{\partial T(L)}{\partial x} \end{bmatrix}
 \end{aligned} \tag{73}$$

### 3.1. Time discretization using the Finite Difference Method (FDM)

The above equation is a general representation of a one-dimensional problem with one linear element. All the terms are included irrespective of the boundary condition. Eq. (50) or (55) is semi-discrete as it is discretized only in space. The differential operator still contains the time-dependent term and it has to be discretized. We now require a method of discretizing the transient terms of the equation. The following subsections give the details of how the transient terms is discretized.

$$[C_{ij}] \left\{ \begin{array}{c} \frac{T_i^{m+1} - T_i^m}{\Delta t} \\ \frac{T_j^{m+1} - T_j^m}{\Delta t} \end{array} \right\} + [K_{ij}(T)] \left\{ \begin{array}{c} \theta T_i^{m+1} + (1-\theta)T_i^m \\ \theta T_j^{m+1} + (1-\theta)T_j^m \end{array} \right\} = \left\{ \begin{array}{c} \theta f_i^{m+1} + (1-\theta)f_i^m \\ \theta f_j^{m+1} + (1-\theta)f_j^m \end{array} \right\} \tag{74}$$

which can be compactly written as;

$$[C] \left\{ \frac{\mathbf{T}^{m+1} - \mathbf{T}^m}{\Delta t} \right\} + [K(T)] \{ \theta \mathbf{T}^{m+1} + (1-\theta)\mathbf{T}^m \} = \{ \theta \mathbf{f}^{m+1} + (1-\theta)\mathbf{f}^m \} \tag{75}$$

Therefore,

$$[[C] + \theta \Delta t [K(T)]] \mathbf{T}^{m+1} = [[C] - (1-\theta)\Delta t [K(T)]] \mathbf{T}^m + \Delta t \{ \theta \mathbf{f}^{m+1} + (1-\theta)\mathbf{f}^m \} \tag{76}$$

where, “m” denotes the time level.

Table 3. Different time-stepping schemes

$\theta$	Name of the Scheme	Comments
0.0	Fully explicit scheme	Forward different method
1.0	Fully implicit scheme	Backward difference method
0.5	Semi-implicit scheme	Crank-Nicolson method

Eq. (76) gives the nodal values of temperature at the  $m + 1$ , time level. These temperature values are calculated using the  $m$  time level values. However, both the  $m + 1$  and  $m$  time level values of the forcing vector  $\{\mathbf{f}\}$  must be known. By varying the parameter  $\theta$ , different transient schemes can be constructed, which are shown in Table 4 for varying values of  $\theta$ . Therefore, for the temporal discretization, two-level  $\theta$  method has been used for the analysis. This approach varies between explicit and implicit strategies and results in the algebraic systems of nonlinear equations.

It is very difficult to provide explicit solutions to the developed systems of nonlinear equations. Therefore, recourse is made to use an iterative predictor-corrector scheme, based on direct substitution iteration to handle nonlinearity in the present analysis. Based on the name, this scheme is an algorithm that proceeds in two steps, namely; the predictor step and then the corrector step. It calculates a rough approximation of the desired quantity in the predictor step and refines the approximation in the corrector step. This scheme combines the advantages associated with explicit and implicit time schemes and hence provides the stable solution to solve complex nonlinear problems (Lewis and Roberts [51]). The steps are shown as follows:

**Predictor**

$$\begin{aligned}
 & [[C(T^m)] + \theta \Delta t A(T^m)] T_*^{m+1} \\
 & = [[C(T^m)] - (1 - \theta) \Delta t A(T^m)] T^m + \Delta t \{ \theta B(T^m) f^{m+1} + B(T^m) (1 - \theta) f^m \}
 \end{aligned} \tag{77}$$

**Corrector**

$$\begin{aligned}
 & [[C(T_p^m)] + \theta \Delta t A(T_p^m)] T_p^{m+1} \\
 & = [[C(T_p^m)] - (1 - \theta) \Delta t A(T_p^m)] T^m + \Delta t \{ \theta B(T_p^m) f^{m+1} + B(T_p^m) (1 - \theta) f^m \}
 \end{aligned} \tag{78}$$

Where  $p = 0, 1, 2, 3 \dots$  up to convergence

$$T_p^m = w T_p^{m+1} + (1 - w) T^m \quad 0 \leq w \leq 1 \tag{79a}$$

$$T_0^{m+1} = T_*^{m+1} \tag{79b}$$

**3.2. Time discretization using the Finite Element Method**

Alternatively, the temporal term in the transient equation can be discretized by using finite element method to discretize Eq. (76) in the time domain. In Eq. (76), the temperature is now discretized in the time domain as in Fig. (4).

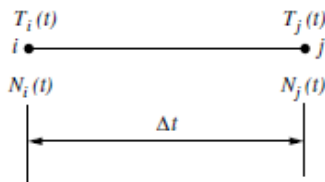


Fig. 5 Time discretization between  $n$ th ( $i$ ) and  $n + 1$ th ( $j$ ) time levels

$$T(t) = N_i(t) T_i(t) + N_j(t) T_j(t) = [N_i(t) \quad N_j(t)] \begin{Bmatrix} T_i(t) \\ T_j(t) \end{Bmatrix} \tag{80}$$

Following the similar procedure as done previously, we can derive the linear shape functions as

$$N_i(t) = 1 - \frac{t}{\Delta t}, N_j(t) = \frac{t}{\Delta t} \tag{81}$$

Therefore, the time derivative of the temperature is thus written as

$$\begin{aligned} \frac{\partial T(t)}{\partial t} &= \frac{\partial N_i(t)}{\partial t} T_i(t) + \frac{\partial N_j(t)}{\partial t} T_j(t) = \left(-\frac{1}{\Delta t}\right) T_i(t) + \left(\frac{1}{\Delta t}\right) T_j(t) = \frac{1}{\Delta t} (T_j(t) - T_i(t)) \\ &\Rightarrow \frac{\partial T(t)}{\partial t} = \begin{bmatrix} -\frac{1}{\Delta t} & \frac{1}{\Delta t} \end{bmatrix} \begin{Bmatrix} T_i(t) \\ T_j(t) \end{Bmatrix} \end{aligned} \tag{82}$$

Substituting Eqs. (77) and (79) into Equ. (54) and applying the weighted residual principle (Galerkin method), we obtain for a time interval of  $\Delta t$ ,

$$\int_{\Delta t} \left[ \begin{bmatrix} N_i(t) \\ N_j(t) \end{bmatrix} \left[ \mathbf{C} \begin{bmatrix} -\frac{1}{\Delta t} & \frac{1}{\Delta t} \end{bmatrix} \begin{Bmatrix} T_i(t) \\ T_j(t) \end{Bmatrix} + [\mathbf{K}(T)] \begin{bmatrix} N_i(t) & N_j(t) \end{bmatrix} \begin{Bmatrix} T_i(t) \\ T_j(t) \end{Bmatrix} - [\mathbf{f}(T)] \right] dt \tag{83}$$

After expansion, we have

$$\int_{\Delta t} \left[ \begin{bmatrix} \mathbf{C} \begin{bmatrix} N_i(t) \\ N_j(t) \end{bmatrix} \begin{bmatrix} -\frac{1}{\Delta t} & \frac{1}{\Delta t} \end{bmatrix} \begin{Bmatrix} T_i(t) \\ T_j(t) \end{Bmatrix} + [\mathbf{K}(T)] \begin{bmatrix} N_i(t) \\ N_j(t) \end{bmatrix} \begin{bmatrix} N_i(t) & N_j(t) \end{bmatrix} \begin{Bmatrix} T_i(t) \\ T_j(t) \end{Bmatrix} - \begin{bmatrix} N_i(t) \\ N_j(t) \end{bmatrix} [\mathbf{f}(T)] \right] dt \tag{84}$$

Substituting Equ. (78) into Equ. (81)

$$\int_{\Delta t} \left[ \begin{bmatrix} \mathbf{C} \begin{bmatrix} 1-\frac{t}{\Delta t} \\ \frac{t}{\Delta t} \end{bmatrix} \begin{bmatrix} -\frac{1}{\Delta t} & \frac{1}{\Delta t} \end{bmatrix} \begin{Bmatrix} T_i(t) \\ T_j(t) \end{Bmatrix} + [\mathbf{K}(T)] \begin{bmatrix} 1-\frac{t}{\Delta t} \\ \frac{t}{\Delta t} \end{bmatrix} \begin{bmatrix} 1-\frac{t}{\Delta t} & \frac{t}{\Delta t} \end{bmatrix} \begin{Bmatrix} T_i(t) \\ T_j(t) \end{Bmatrix} - \begin{bmatrix} 1-\frac{t}{\Delta t} \\ \frac{t}{\Delta t} \end{bmatrix} [\mathbf{f}(T)] \right] dt \tag{85}$$

Again, after expansion of Eq. (85), one arrives at

$$\int_{\Delta t} \left[ \begin{bmatrix} \mathbf{C} \begin{bmatrix} -\left(1-\frac{t}{\Delta t}\right)\left(\frac{1}{\Delta t}\right) & \left(1-\frac{t}{\Delta t}\right)\left(\frac{1}{\Delta t}\right) \\ -\left(\frac{t}{\Delta t}\right)\left(\frac{1}{\Delta t}\right) & \left(\frac{t}{\Delta t}\right)\left(\frac{1}{\Delta t}\right) \end{bmatrix} \begin{Bmatrix} T_i(t) \\ T_j(t) \end{Bmatrix} + [\mathbf{K}(T)] \begin{bmatrix} \left(1-\frac{t}{\Delta t}\right)^2 & \left(1-\frac{t}{\Delta t}\right)\left(\frac{t}{\Delta t}\right) \\ \left(1-\frac{t}{\Delta t}\right)\left(\frac{t}{\Delta t}\right) & \left(\frac{t}{\Delta t}\right)^2 \end{bmatrix} \begin{Bmatrix} T_i(t) \\ T_j(t) \end{Bmatrix} - \begin{bmatrix} 1-\frac{t}{\Delta t} \\ \frac{t}{\Delta t} \end{bmatrix} [\mathbf{f}(T)] \right] dt \tag{86}$$

After the evaluation of Eq. (86), we obtained the characteristic equation over the time interval  $\Delta t$  as

$$\frac{1}{2\Delta t} \left[ \mathbf{C} \begin{bmatrix} -1 & 1 \\ -1 & 1 \end{bmatrix} \begin{Bmatrix} T_i(t) \\ T_j(t) \end{Bmatrix} + \frac{1}{3} [\mathbf{K}(T)] \begin{bmatrix} 2 & 1 \\ 1 & 2 \end{bmatrix} \begin{Bmatrix} T_i(t) \\ T_j(t) \end{Bmatrix} = \frac{1}{2} \begin{bmatrix} 1 \\ 1 \end{bmatrix} \begin{Bmatrix} f_1 \\ f_2 \end{Bmatrix} \right] \tag{87}$$

The above equation involves the temperature values at the  $m$ th and  $(m + 1)$ th level. The quadratic variation of temperature with respect to time shown in Eq. (73) can be treated in a similar fashion.

The boundary conditions and the temperature-dependent parameters are incorporated in the computer program used to solve the system of differential equations. Although, a dimensionless form of the governing equation can be derived for the computer program,

so that the handling of physical quantities is simplified. It should be noted that the thermal properties are evaluated directly in each time step from the nodal temperatures. This eliminates any iteration within each time step for the evaluations of the temperature-dependent parameters.

The element equation/matrix has been derived as shown in the previous equations. It should be noted that the whole domain was divided into a set of 50line elements. Assembling all the elements equation/matrices, a global matrix or a system of equations was obtained. After applying the boundary conditions, the resulting systems of equations is solved numerically.

The convergence criterion of the numerical solution along with error estimation has been set to

$$\sum_i^N |\phi_i^i - \phi^{i-1}| \leq 10^{-4} \quad (88)$$

where  $\phi$  is the general dependent variable  $T$  and  $i$  is the number of iterations.

It should be noted that a steady state is attained when  $\frac{\partial T}{\partial t} = 0$  or  $t \rightarrow \infty$ .

Table 4: Thermo-geometric parameters used for the simulation

S/N	Parameter	Value of Parameter
1	Fin thickness ( $\delta$ )	0.005 m
2	Fin length (L)	0.10 m
3	Specific heat (C)	0.048 kJ/kg°C
4	Density of the fin material ( $\rho$ )	7800 kg/m <sup>3</sup>
5	Thermal conductivity (k)	12W/m°C
6	Heat transfer coefficient ( $h_o$ )	20 W/m <sup>2</sup> °C
7	Electrical conductivity ( $\sigma_m$ )	5x10 <sup>7</sup> S/m
8	Magnetic field intensity ( $B_o$ )	5 $\mu$ T
9	Axial velocity (u)	2.5 m/s
10	power-index, $p = q = r$	0.175
11	Fin base temperature ( $T_b$ )	200°C
12	Initial temperature ( $T_o$ )	200°C
13	Ambient temperature ( $T_\infty$ )	30°C
14	Time step ( $\Delta t$ )	10 sec

## 4. Results and Discussion

For the computational domain, numerical solutions are computed and the necessary convergence of the results is achieved with the desired degree of accuracy. Using the numerical solutions, parametric studies are carried out. Also, in order to define the validity of the results of thermal analysis of fin with assumed insulated tip and that of convective tip, effects of the fin tip conditions on the transient thermal response are investigated. The results with the discussion are illustrated through the Figs. 6-18 and Tables 5-6 to substantiate the applicability of the present analysis.

### 4.1 Verification of results

In order to verify the accuracy of the present numerical method, the numerical results are compared with results obtained by exact analytical method for the linear equation in Eq. (14) as shown in Table 5 and Fig. 6. It is inferred from the figure that there are excellent

agreements between the FEM results and the analytical results, which testifies to the validity of the FEM code. This validation boosts the confidence in the numerical outcomes of the present study. Moreover, it is observed that in the same domain by increasing the polynomial degree of approximation or the number of nodes in an element, one can achieve the desired accuracy with less DOF.

Table 5 shows the comparison of the results obtained by exact analytical and finite element methods for a conductive-convective fin with constant thermal and physical properties of fin having negligible radiation and magnetic field effects. Very good agreements are found between the exact analytical and finite element solutions. The average percentage error of the numerical solution is 0.133 %.

Table 5. Comparison of results

x(m)	Exact analytical Method (°C)	Finite Element Method (°C)	Error	% Error
0.000	200.000	200.000	0.000	0.000
0.020	148.133	148.184	0.051	0.034
0.040	113.895	114.031	0.136	0.119
0.060	92.169	92.339	0.170	0.184
0.080	79.725	79.912	0.187	0.235
0.100	74.710	74.880	0.170	0.228

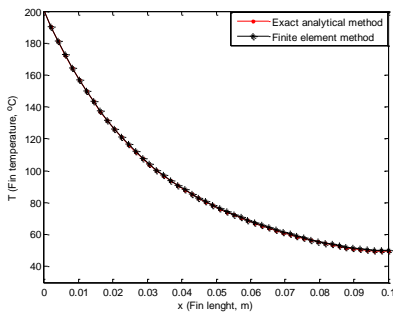


Fig. 6 Comparison of results

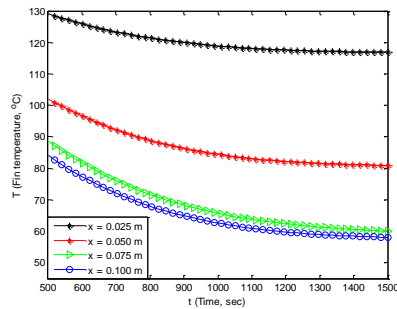


Fig. 7(a) Fin temperature profile at different location (convective tip)

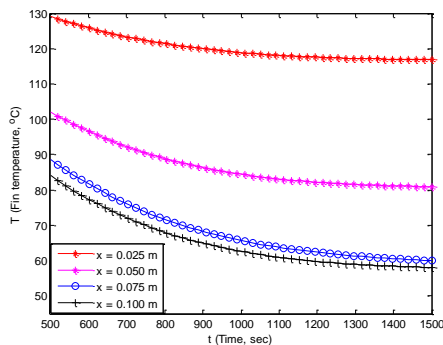


Fig. 8 Fin temperature profile at different location (insulated tip)

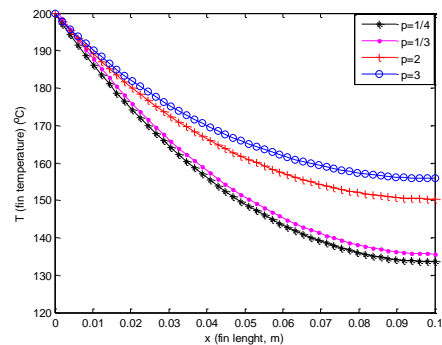


Fig. 7(b) Effects of multi-boiling parameter on the fin temperature distribution

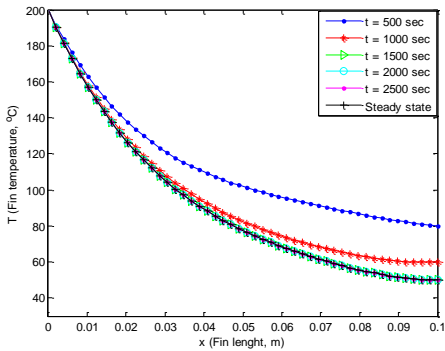


Fig. 9 Fin temperature profile at different time(convective tip)

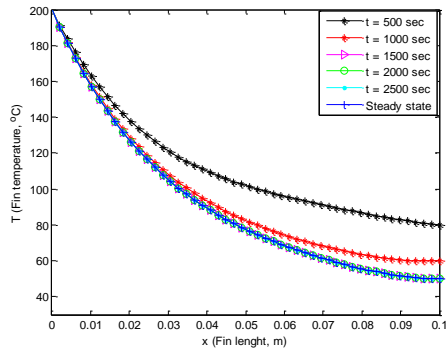


Fig. 10 Fin temperature profile at different time(insulated tip)

Figs. 7 and 8 depict temperature-time history at different four points (0.025 m, 0.050m, 0.075 m and 0.100 m) of the convective-radiative fin with convective and insulated tips, respectively while Fig. 9 and 10 show the temperature profiles of the fin at difference times. The temperature histories at the four points decrease at a faster rate initially, slows down thereafter and finally tending to reach a constant value showing to be near to steady state. Also, a marginal or slightly higher temperature differences are notice between the convective and insulated tip. However, this temperature differences become appreciable as the length of the fin increases and heat is transferred within a short period of time. It could be inferred from the figures and the preceding discussion that for a short fin that undergo heat transfer for a prolonged period of time, adiabatic/insulated condition at the tip can be assumed without any significant loss in accuracy.

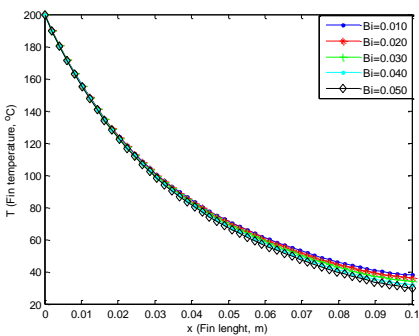


Fig. 11 Effects of Biot number on the fin temperature profile (convective-tip)

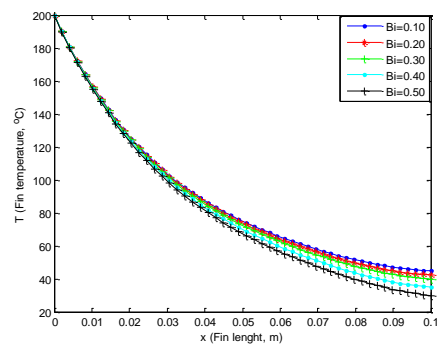


Fig. 12 Effects of Biot number on the fin temperature profile(insulated tip)

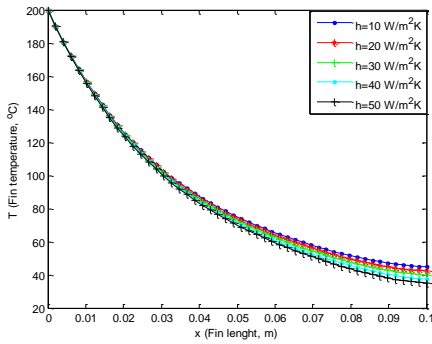


Fig. 13 Effects of heat transfer coefficient on the fin temperature profile

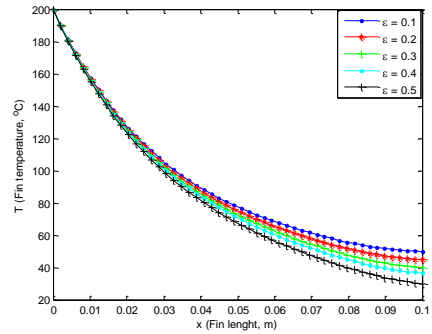


Fig. 14 Effects of emissivity on the fin temperature profile

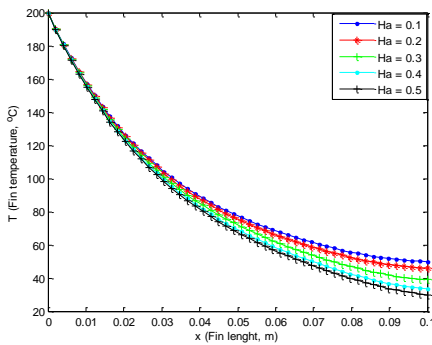


Fig. 15 Effects of magnetic parameter on the fin temperature profile

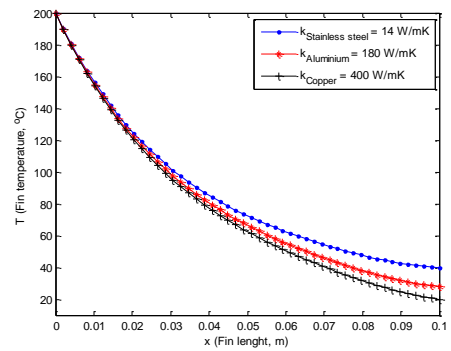


Fig. 16 Effects of thermal conductivity on the fin temperature profile

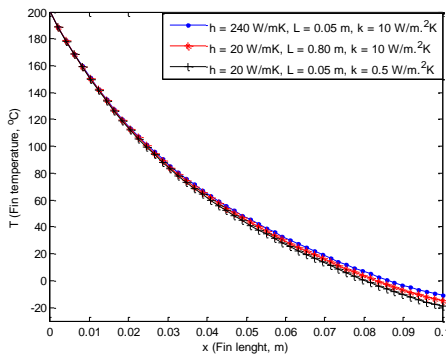


Fig. 17 Effects of thermo-geometric parameter on fin temperature profile

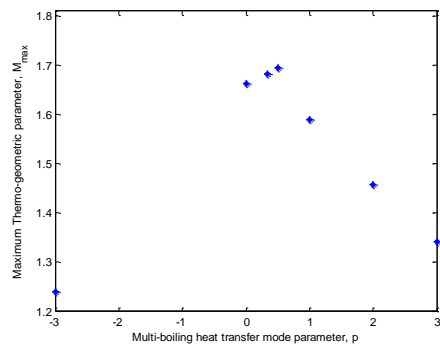


Fig. 18 Effects of multi-boiling parameter on thermal stability of the fin

It has been established that the criterion and errors due to one-dimensional heat transfer analysis is that fin base thickness Biot number should be much smaller than unity (precisely,  $Bi < 0.1$ ). To this end, a one-dimensional analysis has been carried out and simulated within  $0 < Bi < 0.1$ . In this case the error made in the determination of the rate of

heat transfer from the fin to the fluid surrounding it is less than 1% [67, 68]. However, when the Biot number is greater than 0.1 ( $Bi > 0.1$ ), two-dimensional analysis of the fin is recommended as one-dimensional analysis predicts unreliable results for such limit.

Figs. 11 and 12 show the effects of Biot number (conduction-convection parameter) on the temperature distribution in the fin with convective and insulated tips, respectively. From the figures, it is shown that as the Biot number increases, the rate of heat transfer through the fin increases as the temperature in the fin drops faster (becomes steeper reflecting high base heat flow rates) as depicted in the figures.

Effects of heat transfer coefficient on the temperature distribution in the fin is shown in Fig.13. It is shown that the temperature profiles for the various heat transfer coefficient coincide initially but part away as we move towards the tip of the fin. This is due to the fact that coefficient of heat transfer coefficient is a factor/multiplier of the temperature difference between the fin surface and surrounding medium ( $T-T_\infty$ ). It should be noted that the temperature difference between the fin surface and the surrounding decreases as we move away from the fin base to the fin tip even despite the increase in the heat transfer coefficient increases.

It should be noted that for the fin with heat transfer coefficient which varies according to power-law, the hypothetical boundary condition (that is, insulation) at the tip of the fin is taken into account. If the tip is not assumed to be insulated, then the problem becomes overdetermined [68]. This boundary condition is realized for sufficiently long fins. Also, it should be stated that the assumption that the heat transfer coefficient is constant yields incorrect.

Fig. 14 presents the impact of emissivity on the temperature distribution. The temperature of the fin decreases with increase of emissivity value. This is because of increase of emissive heat by radiation from the fin surface especially when the distance from the base increase. Therefore, heat transfer rate increases as the emissivity increases. The radiative heat transfer can be neglected if the base temperature of the fin is low and the emissivity of the fin surface is near zero. The important things in fins surface must be emissive because of high emissivity give a great amount of heat radiation transfer from the fin [38]. It is also established that by increasing the generation-conduction parameter and radiation-conduction parameter, the fin temperature will increase [71].

Fig.15 shows that effects of magnetic parameter, Hartman number on the temperature distribution in the porous fin. The figure depicts that the induced magnetic field in the fin can improve heat transfer through the fin. It is shown that increase in magnetic field on the fin increase the rate of heat transfer from the fin and consequently improve the efficiency of the fin. Fig. 16 shows the effect thermal conductivity of the fin materials on the thermal response of the fin. It could be inferred from the figure that more heat is transferred from fin made of copper material than the fins made of stainless steel and aluminum materials.

Effects of the thermal and geometric parameters on the temperature profile of the fin are shown in Fig. 17 while Fig. 18 shows the influence of thermo-geometric parameter ( $M=(hP/kA)^{0.5}$ ) on the thermal stability of the fin. It was established that the value of  $M$  produces physically unsound behavior for larger values of the thermo-geometric parameter. It is shown that for growing values of the thermo-geometric parameter the temperature tends to negative values at the tip of the fin which shows thermal instability, contradicting the assumption of Eq. 9. Following the assumptions made regarding the numerical solution of the problem, it was realized that these solutions are not only physically unsound but also point toward thermal instability. Therefore, in order for the solution to be physically sound the fin thermo-geometric parameter  $M_{max}$  must not exceed a specific value. By extension, in order to ensure stability and avoid numerical diffusion of

the solution by the Galerkin finite element method, the thermo-geometric parameter,  $M$  must not exceed a certain value.

Table 6a. Effects of convective and insulated tip on the fin temperature distribution

Time (sec.)	Fin Temperature (°C) at x=0.025 m			Fin Temperature (°C) at x=0.050 m		
	Convective tip	Insulated tip	Difference	Convective tip	Insulated tip	Difference
500	129.09	129.45	0.36	102.07	103.00	0.93
1000	118.86	119.16	0.30	84.41	85.08	0.67
1500	116.84	117.04	0.20	80.84	81.31	0.47
2000	116.41	116.58	0.17	80.10	80.49	0.39
2500	116.32	116.48	0.16	79.94	80.31	0.38
$\infty$	116.30	116.45	0.15	79.90	80.26	0.36

Table 6b. Effects of convective and insulated tip on the fin temperature distribution

Time (sec.)	Fin Temperature (°C) at x=0.075 m			Fin Temperature (°C) at x=0.100 m		
	Convective tip	Insulated tip	Difference	Convective tip	Insulated tip	Difference
500	90.01	91.95	1.94	84.06	87.60	3.93
1000	68.30	69.53	1.23	62.61	64.76	2.51
1500	63.85	64.74	0.89	58.23	59.84	1.61
2000	62.91	63.69	0.78	57.30	58.76	1.46
2500	62.71	63.46	0.75	57.10	58.53	1.43
$\infty$	62.66	63.39	0.74	57.05	58.46	1.41

It is established from the results in the Tables 6a and 6b, that for a relatively short fin operating for prolonged periods of time, the results indicate that the adiabatic/hypothetical condition (or negligible heat transfer) at the tip can be assumed without any significant loss in accuracy or equality as compared to the convective boundary at the tip. This is because, for the relatively short fin operating under a steady state, the assumption of insulated tip (or negligible heat transfer at the tip) predicted almost the same results as there is no significant difference between the results of the assumed insulated tip and convective tip. Moreover, for a sharp ended fin, its performance is the same as insulated tip fin. Under such scenario, the fin tip heat convection analysis becomes meaningless due to the infinitesimally small dissipating area. However, for a long cooling fin of finite length operating in a transient state, especially for short period of time, the assumption of insulated tip produces significant different results as compared to the results of the convective tip (Table 6b). It is therefore implied that if it is assumed that no heat transfer takes place at the fin tip, the results obtained for some ranges of thermal and geometric parameters indicate that the determination of temperature distribution and the rate of heat transfer from the fin to its surroundings includes a fairly large error for some conditions which are important for practical applications. Therefore, for transient thermal studies of fins, the assumption of no heat transfer takes place at the fin tip should be taken with caution in thermal analysis of a long cooling fin of finite length operating within a short period of time such as the fin operating under picosecond or nanosecond. Also, such an assumption should not be made when the convective heat transfer coefficient at the tip of the fin is very high or the thermal conductivity of the fin material is very low. It was established that the difference between the results of the insulated tip and convective tip increases as the tip Biot number is increased. In fact, the percentage error of the difference between the results of the insulated tip and convective tip for a very high value of heat transfer coefficient could be as high as 20 % [72].

## 5. Conclusion

In this work, transient thermal behavior of convective-radiative cooling fin with convective tip and subjected to magnetic field have been analyzed using Galerkin finite element method. The numerical solutions are verified by the exact solution developed using Laplace transform. The study revealed that increase in Biot number, convective, radiative and magnetic parameters increase the rate of heat transfer from the fin and consequently, improved the efficiency of the fin. Also, it was established that for a relatively short fin operating for prolonged periods of time or steady state, the adiabatic/hypothetical condition (or negligible heat transfer) at the tip can be assumed without any significant loss in accuracy or equality as compared to the convective condition at the tip. However, for a long cooling fin of finite length operating in a transient state, especially for short period of time, the assumption of insulated tip produces significant different results as compared to the results of the convective tip. Therefore, for transient thermal studies of fins, the assumption that no heat transfer takes place at the fin tip should be taken with caution for a long cooling fin of finite length operating within a relatively short period of time. It is hope that the present study will enhance the understanding of thermal response of solid fin under various factors and especially of practical significance in chemical and nuclear engineering.

## Nomenclature

- A cross sectional area of the fins,  $m^2$   
 $B_0$  Magnetic field intensity (T)  
Bi Biot number  
 $C_p$  specific heat ( $J\ kg^{-1}\ K^{-1}$ )  
 $H$  Heat transfer coefficient ( $Jm^{-2}\ K^{-1}$ )  
 $h_b$  heat transfer coefficient at the base of the fin, ( $Wm^{-2}k^{-1}$ )  
 $J$  Total current intensity (A)  
 $J_c$  Conduction current intensity (A)  
 $k$  thermal conductivity of the fin material, ( $Wm^{-1}k^{-1}$ )  
 $k_b$  thermal conductivity of the fin material at the base, ( $Wm^{-1}k^{-1}$ )  
 $L$  Length of the fin (m)  
 $M$  dimensionless thermo-geometric parameter  
 $P$  perimeter of the fin(m)  
 $q$  heat transfer rate W  
 $t$  time  
 $T$  fin temperature (K)  
 $T_\infty$  ambient temperature, K  
 $T_b$  Temperature at the base of the fin, K  
 $w$  width of the fin  
 $x$  axial length measured from fin base (m)  
 $w$  width of the fin

### Greek Symbols

$\varepsilon$  Emissivity

$\sigma$  Electric conductivity (A/m)

$\sigma_{st}$  Stefan–Boltzmann constant ( $Wm^2 K^4$ )

$\rho$  Density of the fluid ( $kgm^{-3}$ )

$\beta$  thermal conductivity parameter

$\delta$  thickness of the fin, m

### References

- [1] P. Y. Wang P.Y., G. C. Kuo, Y. H. Hu, W. L. Liaw. Transient temperature solutions of a cylindrical fin with lateral heat loss, *Wseas Transactions on Mathematics*, 11(10) (2012), 918-925.
- [2] R. J. Moitsheki, C. Harley. Transient heat transfer in longitudinal fins of various profiles with temperature-dependent thermal conductivity and heat transfer coefficient, *PRAMANA*, 77(3) (2011), 519–532. <https://doi.org/10.1007/s12043-011-0172-6>
- [3] M. D. Mhlongo, R. J. Moitsheki. Some exact solutions of nonlinear fin problem for steady heat transfer in longitudinal fin with different profiles, *Advances in Mathematical Physics*, 2014, 1-16. <https://doi.org/10.1155/2014/947160>
- [4] S. A. Ali, A. H. Bokhari, F. D. Zaman. A Lie symmetry classification of a nonlinear fin equation in cylindrical coordinates, *Abstract and Applied Analysis*, 2014, 1-10. <https://doi.org/10.1155/2014/527410>
- [5] A.H.A Kader, M.S.A. Latif and H. M. Nour. General exact solution of the fin problem with variable thermal conductivity, *Propulsion and Power Research*, 5(1)2016), 63-69.
- [6] R. J. Moitsheki and A. Rowjee. Steady heat transfer through a two- dimensional rectangular straight fin, *Mathematical Problems in Engineering*, 2011, 1-13. <https://doi.org/10.1155/2011/826819>
- [7] K.D. Cole, Computer programs for temperature in fins and slab bodies with the method of Green's functions, *Comput. Appl. Eng. Educ.* 12 (3) (2004) 189–197. <https://doi.org/10.1002/cae.20010>
- [8] A. Jordan, S. Khaldi, M. Benmouna, A. Borucki. Study of non-linear heat transfer problems, *Revue Phys. Appl.*, 22(1987),101-105. <https://doi.org/10.1051/rphysap:01987002201010100>
- [9] B. Kundu, P.K. Das. Performance analysis and optimization of straight taper fins with variable heat transfer coefficient, *International Journal of Heat and Mass Transfer*, 45(2002), 4739- 4751. [https://doi.org/10.1016/S0017-9310\(02\)00189-8](https://doi.org/10.1016/S0017-9310(02)00189-8)
- [10] F. Khani, M. A. Raji, H. H. Nejad. Analytical solutions and efficiency of the nonlinear fin problem with temperature-dependent thermal conductivity and heat transfer coefficient, *Commun Nonlinear Sci Numer Simulat*, 14(2009), 3327-3338. <https://doi.org/10.1016/j.cnsns.2009.01.012>
- [11] S. R. Amirkolei and D. D. Ganji D.D. Thermal performance of a trapezoidal and rectangular profiles fin with temperature-dependent heat transfer coefficient, thermal conductivity and emissivity, *Indian J. Sci. Res.*, 1(2)(2014), 223-229.

- [12] A. Aziz, M. N. Bouaziz. A least squares method for a longitudinal fin with temperature dependent internal heat generation and thermal conductivity, *Energy Conversion and Management*, 52(2011), 2876-2882. <https://doi.org/10.1016/j.enconman.2011.04.003>
- [13] M. G. Sobamowo. Thermal analysis of longitudinal fin with temperature dependent properties and internal heat generation using Galerkin's method of weighted residual, *Applied Thermal Engineering*, 99(2016), 1316-1330. <https://doi.org/10.1016/j.applthermaleng.2015.11.076>
- [14] D. D. Ganji, M. Raghoshay, M. Rahimi, M. Jafari. Numerical investigation of fin efficiency and temperature distribution of conductive, convective and radiative straight fins, *IJRRAS*, 2010, 230-237.
- [15] M. G. Sobamowo, O. M. Kamiyo and O. A. Adeleye. Thermal performance analysis of a natural convection porous fin with temperature-dependent thermal conductivity and internal heat generation. *Thermal Science and Engineering Progress*. 1(2017) 39-52. <https://doi.org/10.1016/j.tsep.2017.02.007>
- [16] M. G. Sobamowo. Thermal performance and optimum design analysis of fin with variable thermal conductivity using double decomposition method. *Journal of Mechanical Engineering and Technology*. Vol. 9(1), 1-32.
- [17] M. G. Sobamowo, L. O. Jayesimi and J. D. Femi-Oyetero (2017). Heat transfer study in a convective-radiative fin with temperature-dependent thermal conductivity and magnetic field using variation of parameter method. *Journal of Applied Mathematics and Computational Mechanics*, 16(3), 85-96. <https://doi.org/10.17512/jamcm.2017.3.08>
- [18] A. Moradi and H. Ahmadikia. Analytical solution for different profiles of fin with temperature dependent thermal conductivity, *Mathematical Problems in Engineering*, 2010, 1-15. <https://doi.org/10.1155/2010/568263>
- [19] S. Sadri, M. R. Raveshi and S. Amiri. Efficiency analysis of straight fin with variable heat transfer coefficient and thermal conductivity, *Journal of Mechanical Science and Technology*, 26(4)(2011), 1283-1290. <https://doi.org/10.1007/s12206-012-0202-4>
- [20] P. L. Ndlovu and R. J. Moitsheki. Analytical solutions for steady heat transfer in longitudinal fins with temperature dependent properties, *Mathematical Problems in Engineering*, 2013, 1-14. <https://doi.org/10.1155/2013/273052>
- [21] S. Mosayebidorcheh, D. D. Ganji, M. Farzinpoor. Approximate solution of the nonlinear heat transfer equation of a fin with the power-law temperature- dependent thermal conductivity and heat transfer coefficient, *Propulsion and Power Research*, 3(1)(2014), 41-47. <https://doi.org/10.1016/j.jprr.2014.01.005>
- [22] S. E. Ghasemi, M. Hatami, D. D. Ganji. Thermal analysis of convective fin with temperature-dependent thermal conductivity and heat generation, *Case Studies in Thermal Engineering*, 4(2014), 1-8. <https://doi.org/10.1016/j.csite.2014.05.002>
- [23] D. D. Ganji and A.S. Dogonchi. Analytical investigation of convective heat transfer of a longitudinal fin with temperature- dependent thermal conductivity, heat transfer coefficient and heat generation, *International Journal of Physical Sciences*, 9(21) (2014), 466-474.
- [24] M. G. Sobamowo, O. A. Adeleye and A. A. Yinusa. Analysis of convective-radiative porous fin with temperature-dependent internal heat generation and magnetic using homotopy perturbation method. *Journal of computational and Applied Mechanics*. Vol. 12(2)(2017), 127-145.

- [25] C. Arslanturk. Optimization of straight fins with step change in thickness and variable thermal conductivity by homotopy perturbation method, *J. of Thermal Science and Technology*, 10(2010), 9-19.
- [26] D. D. Ganji, Z. Z. Ganji, H. D. Ganji (2011). Determination of temperature distribution for annular fins with temperature dependent thermal conductivity by HPM, *Thermal Science*, Vol. 15(1)(2011), 111-115.
- [27] H. A. Hoshyar, I. Rahimipetroudi, D. D. Ganji, A. R. Majidian. Thermal performance of porous fins with temperature-dependent heat generation via the homotopy perturbation method and collocation method, *Journal of Applied Mathematics and Computational Mechanics*, Vol. 14(4)(2015), 53-65. <https://doi.org/10.17512/jamcm.2015.4>.
- [28] I.V. Singh, K. Sandeep, R. Prakash. Heat transfer analysis of two-dimensional fins using a meshless element free Galerkin method, *Numerical Heat Transfer, Part A*, 44(2003), 73-84. <https://doi.org/10.1080/713838174>
- [29] S. Basri, M. M. Fakir, F. Mustapha, D. L. A. Majid, A. A. Jaafar. Heat distribution in rectangular fins using efficient finite element and differential quadrature methods, *Engineering*, 1(2009), 151-160. <https://doi.org/10.4236/eng.2009.13018>
- [30] T. Singh, S. Shrivastava, H. S. Ber H.S. Analysis of unsteady heat conduction through short fin with applicability of quasi theory, *Int. J. Mech. Eng. & Rob. Res.*, 2(1) (2013), 269-283.
- [31] A. K. Sao, Y. P. Banjare. Analysis of thermal characteristics of transient heat conduction through long fin and comparison with exact fin theory and quasi steady theory, *International Journal of Emerging Technology and Advanced Engineering*. 4(11)2014, 157-166.
- [32] B. Lotfi, A. Belkacem. Numerical method for optimum performance of fin profiles, *International Journal of Current Engineering and Technology*, 4(6)(2014), 3990-3998.
- [33] A. A. A. Al-Rashed, L. Kolsi, H. F. Oztop, N. Abu- Hamdeh, M. N. Borjini. Natural convection and entropy production in a cubic cavity heated via pin- fins heat sinks, *International Journal of Heat and Technology*, 35(1)(2017), 109-115. <https://doi.org/10.18280/ijht.350115>
- [34] D. Taler, J. Taler. Steady-state and transient heat transfer through fins of complex geometry, *Archives of Thermodynamics*, 35(2)(2014),117-133. <https://doi.org/10.2478/aoter-2014-0017>
- [35] P. Malekzadeh and H. Rahideh. Two-dimensional nonlinear transient heat transfer analysis of variable section pin fins, *Energy Conversion and Management*, 50(2009), 916-922. <https://doi.org/10.1016/j.enconman.2008.12.025>
- [36] C. S. Reddy, Y. R. Reddy, P. Srikanth. Application of B-spline based FEM to one-dimensional problems, *International Journal of Current Engineering and Technology*, 3(2014), 137-140.
- [37] Y. Sun, J. Ma, B. Li, Z. Guo. Prediction of nonlinear heat transfer in a convective radiative fin with temperature-dependent properties by the collocation spectral method, *Numerical Heat Transfer, Part B: Fundamentals*, 69(1), (2016), 8-73. <https://doi.org/10.1080/10407782.2015.1081043>
- [38] G. Rajul, T. Harishchandra, T. Brajesh. Nonlinear numerical analysis of convective-radiative fin using MLPG method. *International journal of heat and technology*, 35(4)(2017), 721-729

- [39] Z. Wei, L. Haifang, D. Xiaoze, Y. Yongping, S. Lei. Numerical and experimental research on performance of single- row finned tubes in air-cooled power plants, *International Journal of Heat and Technology*, 34(1)(2016), 137-142. <https://doi.org/10.18280/ijht.340120>
- [40] F. Hajabdollahi, H. H. Rafsanjani, Z. Hajabdollahi, Y. Hamidi. Multi- objective optimization of pin fin to determine the optimal fin geometry using genetic algorithm, *Applied Mathematical Modelling*, 36(2012), 244-254. <https://doi.org/10.1016/j.apm.2011.05.048>
- [41] H. Fatoorehchi, H. Abolghasemi. Investigation of nonlinear problems of heat conduction in tapered cooling fins via symbolic programming, *Appl. Appl. Math.*, 7(2)(2012), 717-734.
- [42] M. S. A. Latif, A. H. A Kader, H. M. Nour. Exact implicit solution of nonlinear heat transfer in rectangular straight fin using symmetry reduction methods, *Appl. Appl. Math.*, 10(2)(2015), 864-877.
- [43] A. Mahmoudi, I. Mejri. Analysis of conduction radiation heat transfer with variable thermal conductivity and variable refractive index: Application of the Lattice Boltzmann method, *International Journal of Heat and Technology*, 33(1)(2015), 1- 8. <https://doi.org/10.18280/ijht.330101>
- [44]. M. G. Sobamowo. Analysis of longitudinal fin with temperature-dependent thermal conductivity and internal heat generation. *Alexandra Engineering Journal*, 56(2017), 1-11. <https://doi.org/10.1016/j.aej.2016.04.022>
- [45]. M. G. Sobamowo, B. Y. Ogumola and G. Nzebuka. Finite volume method for analysis of convective longitudinal fin with temperature-dependent thermal conductivity and internal heat generation. *Transfer Phenoma in Fluid and Heat Flows III. Defect and Diffusin Forum*. 374(2017), 106-120.
- [46] M. G. Sobamowo, G. A. Oguntala and J. D. Femi-Oyetero. Investigation of the effects of magnetic field on the thermal performance of convective-radiative fin using wavelet collocation method. *Annals of Faculty of Engineering Honedoara-International Journal of Engineering*. Tome XV(2017), 179-186.
- [47] M. G. Sobamowo. Heat transfer study in porous fin with temperature-dependent thermal conductivity and internal heat generation using Legendre wavelet collocation method. *Communication in Mathematical Modeling and Applications*. Vol. 2(3)(2017), 16-28.
- [48] M. G. Sobamowo and O. M. Kamiyo. Multi-boiling heat transfer analysis of a convective straight fin with temperature-dependent thermal properties and internal heat generation. *Journal of Applied and Computational Mechanics*. 3(4)(2017), 229-239.
- [49] M. G. Sobamowo. Analysis of heat transfer in porous fin with temperature-dependent thermal conductivity and internal heat generation using Chebychev spectral collocation method. *Journal of Computational Applied Mechanics*. Vol. 48(2) (2017), 271-287.
- [50] A.J. Chapman, Transient heat conduction in annular fins of uniform thickness, *Chem. Eng. Symp.* 55(29), (1959) 195–201.
- [51] A.B. Donaldson, A.R. Shouman, Unsteady-state temperature distribution in a convecting fin of constant area, *Appl. Sci. Res.* 26 (1-2)(1972), 75– 85. <https://doi.org/10.1007/BF01897836>
- [52] N.V. Suryanarayana, Transient response of straight fins, *J. Heat Transf.* 97 (1975), 417–423. <https://doi.org/10.1115/1.3450391>
- [53] N.V. Suryanarayana, Transient response of straight fins part II, *J. Heat Transf.* 98 (1976), 324–326. <https://doi.org/10.1115/1.3450546>

- [54] J. Mao, S. Rooke, Transient analysis of extended surfaces with convective tip, *Int. Commun. Heat Mass Transf.* 21 (1994), 85–94. [https://doi.org/10.1016/0735-1933\(94\)90086-8](https://doi.org/10.1016/0735-1933(94)90086-8)
- [55] J.V. Beck, K.D. Cole, A. Haji-Sheikh, B. Litkouhi, *Heat Conduction Using Green's Functions Hemisphere, New York, 1992.*
- [56] R.H. Kim, The Kantorovich method in the variational formulation to an unsteady heat conduction. *Lett. Heat Mass Transf.* 3 (1) (1976), 73–80.
- [57] A. Aziz, T.Y. Na, Transient response of fins by coordinate perturbation expansion, *Int. J. Heat and Mass Transfer* 23 (1980), 1695–1698. [https://doi.org/10.1016/0017-9310\(80\)90232-X](https://doi.org/10.1016/0017-9310(80)90232-X)
- [58] A. Aziz, A.D. Kraus, Transient heat transfer in extended surfaces, *Appl. Mech. Rev.* 48 (3) (1995), 317–349. <https://doi.org/10.1115/1.3005105>
- [59] A. Campo and A. Salazar, Similarity between unsteady-state conduction in a planar slab for short times and steady-state conduction in a uniform, straight fin, *Heat Mass Transf.* 31 (5) (1996), 365–370. <https://doi.org/10.1007/BF02184052>
- [60] A.K. Saha, S. Acharya, Parametric study of unsteady flow and heat transfer in a pin-fin heat exchanger, *Int. J. Heat Mass Transf.* 46 (20) (2003), 3815–3830. [https://doi.org/10.1016/S0017-9310\(03\)00190-X](https://doi.org/10.1016/S0017-9310(03)00190-X)
- [61] T.H. Hsu, C.K. Chen, Transient analysis of combined forced and free convection conduction along a vertical circular fin in micro polar fluids, *Numer. Heat Transf. A* 19 (2) (1991), 177–185. <https://doi.org/10.1080/10407789108944844>
- [62] M. Benmadda, M. Lacroix, Transient natural convection from a finned surface for thermal storage in an enclosure, *Numer. Heat Transf. A* 29 (1) (1996), 103–114. <https://doi.org/10.1080/10407789608913781>
- [63] D.K. Tafti, L.W. Zhang, G. Wang, Time-dependent calculation procedure for fully developed and developing flow and heat transfer in louvered fin geometries, *Numer. Heat Transf. A* 35 (3) (1999), 225–249. <https://doi.org/10.1080/104077899275227>
- [64] A.K. Saha, S. Acharya, Unsteady simulation of turbulent flow and heat transfer in a channel with periodic array of cubic pin-fins, *Numer. Heat Transf. A* 46 (8) (2004), 731–763 *Exact Solution for Transient Heat Conduction through Long Fin.* <https://doi.org/10.1080/104077890504465>
- [65] M. Tutar, A. Akkoca, Numerical analysis of fluid flow and heat transfer characteristics in three-dimensional plate fin-and-tube heat exchangers, *Numer. Heat Transf. A* 46 (3) (2004), 301–321. <https://doi.org/10.1080/10407780490474762>
- [66] I. Mutlu, T.T. Al-Shemmeri, Steady-state and transient performance of a shrouded Longitudinal fin array, *Int. Commun. Heat Mass Transf.* 20 (1993), 133–143. [https://doi.org/10.1016/0735-1933\(93\)90014-M](https://doi.org/10.1016/0735-1933(93)90014-M)
- [67] R. K. Irey, Errors in the one-dimensional fin solution, *J. Heat Transfer* 90, 175–176 (1968).
- [68] K Laor and H Kalman. The effect of tip convection on the performance and optimum dimension of cooling fins. *Int. Comm. Heat Mass Transfer*, 19(1992), 569–584. [https://doi.org/10.1016/0735-1933\(92\)90012-7](https://doi.org/10.1016/0735-1933(92)90012-7)
- [69] W. Lau and C. W. Tan, Errors in one-dimensional heat transfer analysis in straight and annular fins, *J. Heat Transfer* 95(1973), 549–551. <https://doi.org/10.1115/1.3450110>
- [70] H. C. Unal, Determination of the temperature distribution in an extended surface with a non-uniform heat Effect of the boundary condition at a fin tip on the performance of the fin

1495 transfer coefficient, *Int. J. Heat Mass Transfer* 28(1985), 2279-2284.  
[https://doi.org/10.1016/0017-9310\(85\)90046-8](https://doi.org/10.1016/0017-9310(85)90046-8)

- [71] S.A. Atouei, Kh. Hosseinzadeh, M. Hatami, Seiyed E. Ghasemi, D.D. Ganji. Heat transfer study on convective–radiative semi-spherical fins with temperature-dependent properties and heat generation using efficient computational methods. *Applied Thermal Engineering*, Volume 89(5), 299-305, 2015. <https://doi.org/10.1016/j.applthermaleng.2015.05.084>
- [72] M. G. Sobamowo and A. A. Oyediran. Effects of Thermo-geometric parameter on the heat transfer rate in Straight fin wit variable thermal conductivity. *A Festschrift Celebrating 70 years of Life and Excellence of Emeritus Professor Vincent Olusegun Sowemimo Olunloyo*, 2013.



Research Article

## A comparative study on the energetic- exergetic and economical performance of a photovoltaic thermal system (PVT)

Canan Kandilli<sup>a</sup>

*Department of Mechanical Engineering, Uşak University, Uşak, TURKEY*

### Article Info

### Abstract

#### Article history:

Received 17 Jan 2019

Revised 4 Feb 2019

Accepted 9 Feb 2019

#### Keywords:

*Photovoltaic thermal system (PVT);  
Water heating system;  
Energy-exergy analysis;  
Economic analysis*

In this experimental study, it is aimed to present a comparative study on the energetic-exergetic and economical performance of the PVT system. A new and easy-handle approach has been also developed to assess the exergetic performance of a PVT system. Economical evaluation of both PV and PVT systems has been also performed by NPV method. Useful energy rate, surface temperature, electrical energy and overall energy efficiency, exergy efficiency, exergy destruction values of PV and PVT systems have been compared. It was found that the electrical efficiency, overall energy efficiency and exergy efficiency of PVT system vary between 0.10 and 0.13; 0.26 and 0.54 and 0.10 and 0.12 respectively. It is found that the exergy and energy efficiency values of the PVT system are greater than the exergy and energy efficiency values of the PV system. It is calculated that the PVT system has considerably short payback time after 8 years of operation; while the payback period of PV was found as 16 years under the same meteorological conditions.

© 2018 MIM Research Group. All rights reserved.

## 1. Introduction

The conversion efficiency of photovoltaic cells is relatively low, usually in the range of 10–20% for commercially available silicon cells. More than half of the solar radiation, collected with considerable effort and investment, is converted to thermal energy and then rejected to the environment. A well-known way to achieve a better overall efficiency is cogeneration: capturing the waste heat as well and using it as an additional energy product. This can be achieved with photovoltaic/thermal (PVT) collectors that contain a heat exchanger behind the PV cells to collect the heat rejected from the cells [1]. The concept of PVT has been used and discussed for more than three decades by various researchers both experimentally and numerically. During the 1970s, the research on PVT started, with the focus on PVT collectors, with the main aim of increasing the overall energy efficiency [2].

PVT idea is based on the utilizing both a PV and a thermal system together. The aim of PVT systems is not only to cool the system, is to utilize the heat emerged on the system as well. There are many theoretical and experimental studies on air or water cooling application for PVT system in the literature [3-17]. Chow et al. [8] developed energy models for a building-integrated photovoltaic/water-heating system. They showed that the photovoltaic/ water-heating system is having much economical advantages over the conventional photovoltaic installation. They also observed that the system thermal performance under natural water circulation is better than the pump-circulation mode. They found that the year-round thermal and cell conversion efficiencies were found

<sup>\*</sup>Corresponding author: [canan.kandilli@usak.edu.tr](mailto:canan.kandilli@usak.edu.tr)

<sup>a</sup> [orcid.org/0000-0001-7159-4174](https://orcid.org/0000-0001-7159-4174)

DOI: <http://dx.doi.org/10.17515/resm2019.90en0117>

respectively 37.5% and 9.39% under typical Hong Kong weather conditions. Pei et al. [17] proposed heat-pipe photovoltaic/thermal (HP-PV/T) collector. They found the daily thermal efficiency, electrical efficiency, total PVT efficiency and primary-energy-saving efficiency as 41.0–48.0, 10.0–11.2, 47.0–53.3 and 57.0–63.0% for the system using the collector with the tube space of heat pipes at 80 mm, respectively; while the daily thermal efficiency, electrical efficiency, total PVT efficiency and primary-energy-saving efficiency were 39.0–46.0, 9.0–11.0, 45.0–51.0 and 53.0–60.0% for the system using the collector with the tube space of heat pipes at 140 mm, respectively.

Although numerous studies exist on the energy performance of PVT systems, there are very limited studies on the exergetic assessment. It is essential to analyze the quality of energy as well as its quantity. Exergetic analysis of any system could provide more accurate results to evaluate the system performance. Chow et al. [18] carried out a study of the appropriateness of glass cover on a thermosyphon-based water-heating PVT system. They found that a glazed PVT system is suitable to maximize the quantity of either the thermal or the overall energy output. On the other hand, from the exergy analysis point of view, the increase of PV cell efficiency, packing factor, water mass to collector area ratio, and wind velocity are found favorable to go for an unglazed system, whereas the increase of on-site solar radiation and ambient temperature are favorable for a glazed system. Tiwari et al. [19] observed that the daily overall thermal efficiency of the integrated photovoltaic thermal solar system increases with increase constant flow rate and decrease with increase of constant collection temperature. They also investigated the system exergetically. Dincer et al. [20] performed a detailed review of photovoltaic and photovoltaic thermal systems on the basis of its performance based on electrical as well as thermal output. The performance analysis has been also discussed including all aspects, e.g., electrical, thermal, energy, and exergy efficiency. Sarhaddi et al. [21] presented a detailed energy and exergy analysis to calculate the thermal and electrical parameters, exergy components and exergy efficiency of a typical PVT air collector. They found that the thermal efficiency, electrical efficiency, overall energy efficiency and exergy efficiency of PV/T air collector is about 17.18%, 10.01%, 45% and 10.75% respectively for a sample climatic, operating and design parameters. Saidur et al. [22] gave a place to exergy analysis of PVT system in their comprehensive literature review including exergy modelling. Ozturk et al. (2012) performed an energy, exergy and Life Cycle Assessment (LCA) analysis of a Flat-Plate (FP) collector, a Photovoltaic (PV) system and a Photovoltaic-Thermal (PVT) collector. They found that instantaneous energy, daily energy and exergy efficiency of the FP collector, the PV system and the PV/T collector vary between 53–61%, 19–30%, 23–37% and 56–74%, 11–15%, 21–34% and 2–7%, 6–22% and 8–16%, respectively [23]. Tiwari and Barnwal (2009) carried out the performance analysis of a hybrid photovoltaic-thermal (PV/T) greenhouse air heater and dryer. They observed that exergy efficiency of the greenhouse air heater is less than the thermal efficiency, and exergy efficiency with load is lower than that of without load as expected [24]. Kumar and Tiwari (2009) presented the thermal analysis of a new design of hybrid photovoltaic/thermal (PV/T) active solar distillation system. They concluded that the average annual exergy efficiency of hybrid active solar still is higher than passive solar still almost by 25%, while the energy efficiency is lower by 24% [25]. Tiwari et al. (2009) studied on the Energy Pay Back Time (EPBT) of Hybrid Photovoltaic-Thermal (HPVT) air collector based on exergy analysis for composite climate of New Delhi. They also evaluated the exergy metrics namely Electricity Production Factor and Life Cycle Conversion Efficiency in addition to EPBT by using exergetic output. They concluded that that EPBT of HPVT air collector without balance of system based on exergy and energy output is about 10 years and 2 years, respectively, for single fan operation of the HPVT air collector [26].

Actually, there are many different active and passive cooling methods for enhancing PV module efficiency. While hybrid PV/TE system integrating heat sink [27], Hybrid micro-channel solar cell/module [28], using nanofluid [29], using PCM [30], direct liquid-immersion cooling [31], natural circulation of water in a flat-box absorber [32], using hybrid microchannel with nanofluid [33-35], using microchannel heat sink with nanofluid could be listed as passive cooling methods; jet impingement, water spraying, using ferrofluid and magnetic field and Jet array nanofluids impingement could be considered active cooling system in the literature [36-39].

However, comparative studies including exergetic assessment on PVT systems are very limited in the literature. In the present study, a new and easy-handle approach has been proposed to assess the exergetic performance of a PVT system; it is aimed to present a comparative study on the energetic- exergetic and economical performance of a PVT system consisting monocrystalline silicon solar cells and a copper plate with copper tubes on the back for water heating. Economical evaluation of both PV and PVT systems has been also performed by NPV method. There is not any study on comparison of PV and PVT systems by NPV method in the literature. The experiments have been conducted at Usak University, Department of Mechanical Engineering, in March, 2012. The data have been employed to determine electrical and thermal performance of the experimental (PVT) and the control (PV) systems. Useful energy rate, surface temperature, electrical energy and overall energy efficiency, exergy efficiency, exergy destruction values of PV and PVT systems have been compared. The variation of entropy generation due to surface temperature of PVT system has been examined and discussed. In the first section of the present study, it was given a brief review on PVT systems and explained the aim of the study. In the second section, theoretical aspects and thermodynamic analysis have been represented. Description of the control (PV) and experimental (PVT) systems employed in the study, data used in the calculations and the results of the experiments are covered in "Results and Discussion" as Section 3, while the last section gets conclusions.

## **2. Thermodynamic Analysis**

Solar energy exhibits a spectrum with a very wide range of wavelengths. A certain part of wavelengths of the solar spectrum are converted to electrical energy by PV materials. After the interaction between the materials and solar energy, a great portion of the solar energy is transformed to excessive heat, not to electrical energy. This excessive heat load on the materials affects negatively the crystalline structure of PV and causes to decrease the energy efficiency for both short and the long terms. However, PVT systems provide both electrical and thermal conversion and help to remove this excessive heat load. While this excessive heat load could be utilized as a thermal energy source, the electrical conversion efficiency of the PV can be kept at the desired values. For example, mono-crystalline Si solar cells have been employed in the present study. Mono-crystalline Si solar cells have a spectral response of 400-800 nm wavelength of solar radiation and can convert the solar energy to electricity in this spectral range. Wavelength values outside this spectral range cause the excessive heating load on the Si solar cell. This excessive heat load can be evaluated as a thermal energy source and can be utilized to heat water for building applications.

The first law of thermodynamics deals with the quantity of energy and asserts that energy cannot be created or destroyed. This law merely serves as a necessary tool for the bookkeeping of energy during a process and offers no challenges to the engineer. The second law, however, deals with the quality of energy. The second law of thermodynamics has proved to be a very powerful tool in the optimization of complex thermodynamic systems [23]. In this section, energy and exergy analyses have been modeled, and the NPV method has been explained for the economical analysis.

## 2.1. Energy Analysis

The overall energy efficiency of a PVT system could be calculated as below:

$$\eta_{pvt} = \eta_{pv} + \eta_{th} \quad (1)$$

The electrical energy efficiency of a PV system can be found as follows:

$$\eta_{pv} = \frac{V_m I_m}{A_{pv} I_t} \quad (2)$$

The thermal efficiency of a PVT system could be defined by following equation:

$$\eta_{th} = \frac{\dot{Q}}{A_{pv} I_t} \quad (3)$$

The useful thermal energy of any water heating system could be easily calculated as below:

$$\dot{Q} = \dot{m} C_p (T_{out,water} - T_{in,water}) \quad (4)$$

## 2.2 Exergy Analysis

Irreversibility in the system, in other words, the destruction of exergy can be presented as follows [40]

$$\Sigma \dot{E}x_{in} - \Sigma \dot{E}x_{out} = \Sigma \dot{E}x_{dest} \quad (5)$$

In the present study, a new and easy-handle approach has been also developed to assess the exergetic performance of a PVT system by defining the inlet exergy rate ( $\dot{E}x_{in}$ ) and the outlet exergy rate ( $\dot{E}x_{out}$ ) as below.  $\dot{E}x_{in}$  consists of the exergy rate of solar and exergy rate of inlet water and  $\dot{E}x_{in}$  could be presented as follows:

$$\dot{E}x_{in} = \dot{E}x_{solar} + \dot{E}x_{mass,in} \quad (6)$$

The outlet exergy rate ( $\dot{E}x_{out}$ ) can be defined as the sum of the electrical exergy rate from the PV part and the exergy rate of outlet water.

$$\dot{E}x_{out} = \dot{E}x_{mass,out} + \dot{E}x_{pv} \quad (7)$$

The exergy rate of solar energy could be found as following equation:

$$\dot{E}x_{solar} = \psi_{solar} I_t A_{pv} \quad (8)$$

The maximum efficiency ratio  $\psi_{solar}$ , can be calculated as follows:

$$\psi_{solar} = 1 + \frac{1}{3} \left( \frac{T_0}{T} \right)^4 - \frac{4}{3} \left( \frac{T_0}{T} \right) \quad (9)$$

where T was taken to equal the solar radiation temperature with 6000 K in exergetic evaluation given by Petela [41].

Inlet and outlet water exergy rates can be found as following equations [23]:

$$\dot{E}x_{mass,in} = \dot{m}_{in} \psi_{in} \quad (10)$$

$$\dot{E}x_{mass,out} = \dot{m}_{out} \psi_{out} \quad (11)$$

where  $\psi_{in}$  and  $\psi_{out}$  are specific exergy values for inlet and outlet water respectively and calculated as follows:

$$\psi_{in} = (h_{in} - h_0) - T_0(S_{in} - S_0) \quad (12)$$

$$\psi_{out} = (h_{out} - h_0) - T_0(S_{out} - S_0) \quad (13)$$

The electrical exergy output of PV part of the system could be calculated as follows:

$$\dot{E}x_{PV} = \dot{W} = \eta_{pv} I_t A_{pv} \quad (14)$$

The exergy (the second law) efficiency can be found as below:

$$\varepsilon = \frac{\dot{E}x_{output}}{\dot{E}x_{input}} = 1 - \frac{\dot{E}x_{dest}}{\dot{E}x_{input}} \quad (15)$$

The entropy generation rate can be expressed as follows;

$$\dot{S}_{gen} = \frac{\dot{E}x_{dest}}{T_0} \quad (16)$$

where  $T_0$  is dead state temperature.

### 2.3. Economical Analysis

Net Present Value (NPV) is one of the methods that allow analysing the economic aspects of an engineering system. It is possible to calculate the present value of all annual capital expenditures and savings by NPV methods during the life time of a project. Net present value (NPV) is the sum of all the current values (costs are shown negative, and net savings are shown as positive) is obtained. If NPV is positive then the project is accepted, otherwise application of the project is cancelled. NPV is calculated by the following formulas:

$$NPV = \sum_{i=1}^n (B - C)_i a_i \quad (17)$$

$$a = \frac{1}{(1+i)^p} \quad (18)$$

“a” is net present value factor, B is gain, p is period, i is discount rate in the equation given above.

### 3. Results and Discussion

An experimental (PVT) and a control (PV) system chosen the same PV material have been established at Usak University, Department of Mechanical Engineering. Energy and exergy analyses have been carried out for both experimental and control systems. The systems fixed at the same tilt angle ( $38^\circ$ ) and oriented the same direction have been tested under the same meteorological conditions, during March, 2012. While the inlet and outlet water temperatures, water mass flow rate, ambient temperature, global solar irradiance and temperature on the surfaces of PV and electrical measurements have been recorded for the experimental PVT system; global solar irradiance, surface temperature and electrical data have been collected for the control PV system simultaneously. The sixty-four data have been obtained and employed to compare the electrical and thermal performance of the systems. Properties and characterization of PV modules employed in the present study are presented in Table 1. In the construction of PVT, the thickness of the copper plate fixed to back of the tedlar layer of the PV system is 2 mm and copper pipes welded to the copper plate have a diameter as 8 mm and its length is 23 m. Back of PVT system has been insulated by a layer of glass wool. The photos of the experimental set up including PV and PVT systems can be seen in Fig.1.

Table 1 Properties and characterization of PV modules

$I_{sc}/I_{mp}$ (A)	8.154/7.586
$V_{oc}/V_{mp}$ (V)	37.30/27.18
$\eta_{cell}$ (%)	15.16
$\eta_{module}$ (%)	13.69
Area (m <sup>2</sup> )	1.617
Front Glass	Transparent, toughened safety glass
Cell Structure	Monocrystalline Si (156 mmx156 mm)
Cell Encapsulation	EVA (Ethylene Vinly Acetate)
Backsheet	Tedlar
Frame	Anodized Aluminum

Exttech HD200 type K thermocouples measuring the temperature range from -100°C to 1372°C with measurement error of  $\pm 0.15\%$  were utilized to get inlet and outlet temperature of water for the PVT system. Infrared thermometers operating range from -30°C to +550°C, with a measurement error of  $\pm 2\%$  have been employed to measure the surface temperatures of the PV and the PVT systems. The current and the voltage values obtained from the PV and PVT system have been read by the solar regulator (Steca PR2020).



(a)



(b)



(c)

Fig 1. The photos of the experimental set up (a) Structure of PVT system, (b) Obtaining data for PVT system, (c) Obtaining data for PV system

Delta OHM HD 2102.2 radiometric probe operating range from 0.1.10-3 W/m<sup>2</sup> to 2000 W/m<sup>2</sup> has been used to measure with an uncertainty of  $\pm 5\%$  was used to determine the solar irradiance on the surface of PV and the PVT system. The ambient temperature values

with  $\pm 2^\circ\text{C}$  accuracy have been obtained from the weather station (Davis Vantage Pro2) established on the roof of Mechanical Engineering Department, Usak University. The sixty-four measurements have been collected during the experiments. The results of the analysis according to the data obtained from experiments have been presented as below.

The variation of the useful energy rate (W) obtained from the PV and the PVT systems by incoming solar irradiance ( $\text{W}/\text{m}^2$ ) to the surface of the systems are presented in Fig.2. The experiments have been carried out on the roof of Usak University, Mechanical Engineering Department building during March, 2012. Useful energy rates ranged from 44.8 W to 124.4 W and from 83.3 to 584.8 W for PV and PVT systems respectively; while the solar irradiance varied from  $323 \text{ W}/\text{m}^2$  to  $780 \text{ W}/\text{m}^2$ . Useful energy rates increase by increasing solar irradiance values for both PV and PVT system. It is observed that the useful energy rates of the PVT system are highly greater than the useful energy rates of PV system.

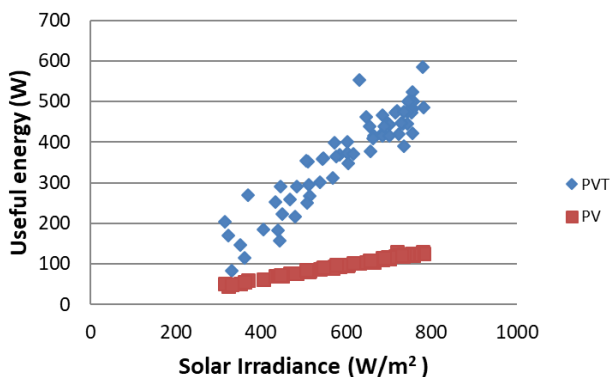


Fig 2. Variation of the useful energy rate (W) obtained from the PV and the PVT systems by solar irradiance ( $\text{W}/\text{m}^2$ )

The variation of surface temperature (K) of PV and PVT systems and ambient temperature (K) are plotted in Fig.3. The surface temperatures of PV and PVT system ranged from 293 to 316 K and 293 to 330 K respectively, while the ambient temperature varied from 283 to 289 K. It is remarkable that the surface temperature of the PVT system is higher than the surface temperature of the PV system. It is estimated that the well-applied insulation on the back of the PVT system causes to decrease the convection losses from bottom side of PVT system. On the other hand, PV module has lower the surface temperature due to convection losses from the bottom of the module. The higher surface temperature of the PVT system could mean that there is still some thermal energy can be transferred to the water. If the heat transfer amount from the solar cell to cooling water could be improved, the surface temperature of PVT could be diminished.

The variation of the electrical energy efficiency of PV and the PVT system and overall energy efficiency of the PVT system due to incoming solar irradiance ( $\text{W}/\text{m}^2$ ) to the surface of the systems are given in Fig.4. Electrical energy efficiency values ranged from 0.09 to 0.10 and from 0.10 to 0.13 for PV and PVT systems respectively and the overall energy efficiency values showed results from 0.26 to 0.54; while the solar irradiance varied from  $323 \text{ W}/\text{m}^2$  to  $780 \text{ W}/\text{m}^2$ . The overall energy efficiency values are in good agreement with the literature [8,17,21,23].

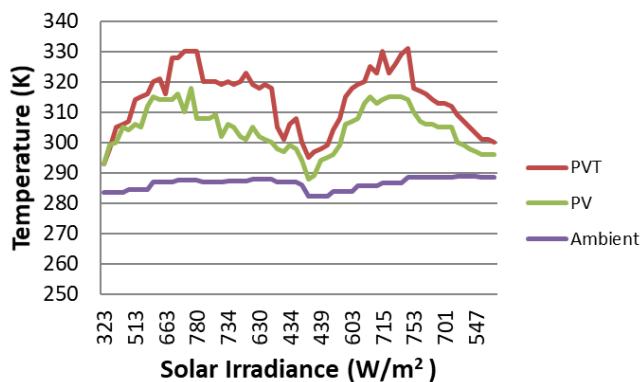


Fig 3. Variation of surface temperature (K) of PV and PVT systems and ambient temperature (K)

The electrical efficiency values of the PVT system are slightly higher than the electrical energy efficiency values of the PV system. In the literature, Tripanagnostopoulos et al. (2002) studied the performance characteristic of PV/water and PV/air systems and compared the electrical efficiency. They found that polycrystalline silisyum (pc-Si) PVT system was more effective as % 3.2 than of the polycrystalline silisyum (pc-Si) PV module [3]. In the present study, it could be confirmed that a PVT application provides the higher electrical energy efficiency than a conventional PV system.

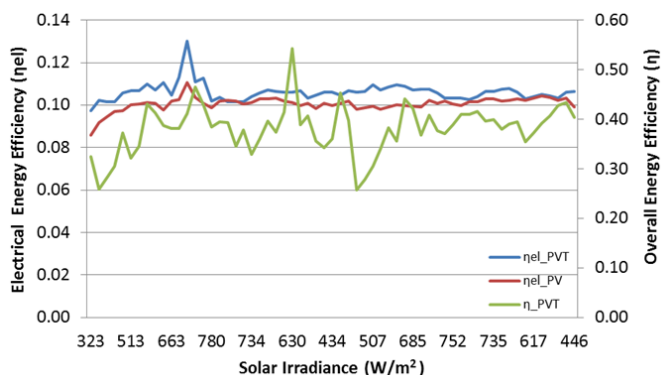


Fig 4. Variation of the electrical energy efficiency of PV and the PVT system and overall energy efficiency of the PVT system due to solar irradiance (W/m²)

The variation of the exergy efficiency of PV and the PVT system due to incoming solar irradiance (W/m²) are plotted in Fig.5. The exergy efficiency has taken value from 0.10 to 0.12 and from 0.09 to 0.12 for PVT and PV systems respectively; while the solar irradiance varied from 323 W/m² to 780 W/m². The exergy efficiency values of the PVT system are slightly greater than the exergy efficiency values of PV system. However, there is not any meaningful difference between the exergy efficiency values of PV and PVT systems.

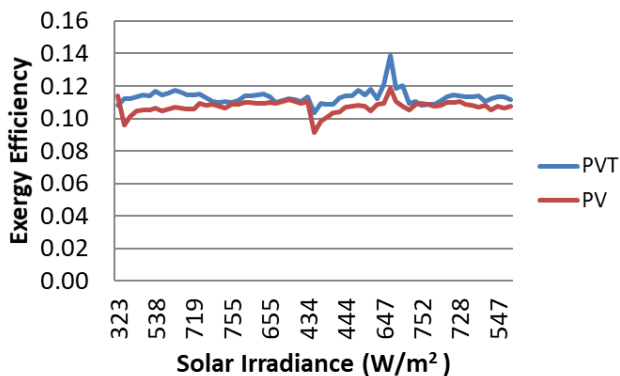


Fig 5. Variation of the exergy efficiency of PV and the PVT system due to solar irradiance (W/m<sup>2</sup>)

It is explanatory to examine exergy destruction and entropy generation for the second law of thermodynamics. The difference of the exergy destruction (W) of the PV system and PVT system by solar irradiance (W/m<sup>2</sup>) are shown in Fig.6. Difference of exergy destruction rates of PV and PVT systems ranged from 1.98 W to 14.79 W; while the solar irradiance varied from 323 W/m<sup>2</sup> to 780 W/m<sup>2</sup>. Exergy destruction rate of PV system is slightly greater than the exergy destruction rate of PVT. However, this difference is not meaningful; when they are compared to high inlet values of solar exergy.

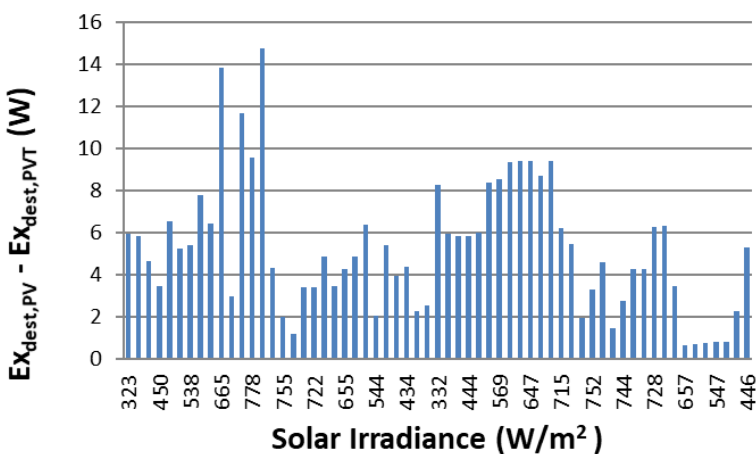


Fig 6. The difference of the exergy destruction (W) of the PV system and PVT system by solar irradiance (W/m<sup>2</sup>)

The variation of the entropy generation (W/K) of the PVT system due to surface temperature (K) of PVT system is represented in Fig.7. Entropy generation rates ranged from 1.55 W/K to 3.54 W/K for PVT system; while the surface temperatures of the PVT varied from 293 K to 330 K. Entropy generation rates increase by increasing surface temperatures of PVT system. It could be possible to decrease the entropy generation of PVT system by decreasing surface temperature of PVT system.

Some improvements could be carried out to minimize the entropy generation and maximize the exergy efficiency of the PVT system. Better heat transfer from the solar cells to the copper plate can be supplied by removing the tedlar layer of the PV panel. The surface area of pipes welded to the copper plate can be increased. Pipe diameter, wall

thickness of the pipes, material used can be changed to achieve optimum operation condition for future studies. In the present study, the PVT system has been operated at 0.0071 kg/h mass flow rate. The optimum mass flow rate can be investigated to provide maximum the first and the second law efficiencies of the thermodynamics for a future works.

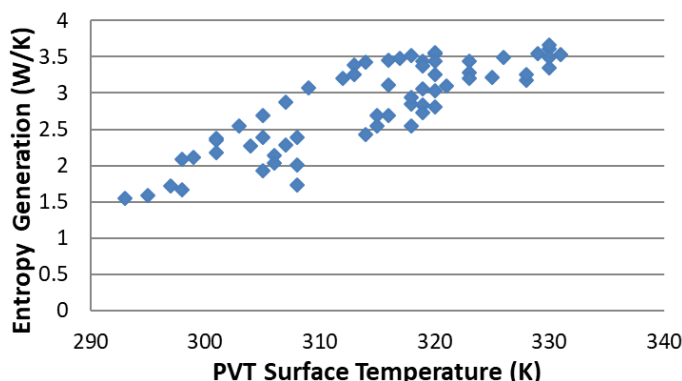


Fig 7. Variation of the entropy generation (W/K) of the PVT system due to surface temperature of PVT system

Table 1. Economical analysis of PVT system by NPV method

Period (Years)	0	1	2	3	4	5	6	7	8
Initial Investment Cost (\$)	-1363.0								
Benefits Per Year (\$)		202.00	202.00	202.00	202.00	202.00	202.00	202.00	202.00
Maintenance and Repair Costs (\$)		-0.11	-0.11	-0.11	-0.11	-0.11	-0.11	-0.11	-0.11
Interest rate	0.01	0.01	0.01	0.01	0.01	0.01	0.01	0.01	0,01
Net cash flow (\$)		201.89	201.89	201.89	201.89	201.89	201.89	201.89	201.89
Discounted net flow	0.99	0.99	0.98	0.97	0.96	0.95	0.94	0.93	0.92
NPV		199.89	197.91	195.95	194.01	192.09	190.19	188.30	186.44
		-	-	-	-	-	-	-	-
		1163.1	965.20	769.25	575.24	383.15	192.97	-4.66	181.78
		1							

Economical evaluation of both PV and PVT systems has been also performed by NPV method given as Eq. (17) and (18). The results of economic analysis were shown in Table 2 and Table 3. In the economic analysis, the yearly mean sunshine period was assumed as 7.5 h/day for Usak province and the cost of electricity was accepted 0.20 \$/kWh.

Average overall efficiency, produced energy per a year, annual income and investment cost of the PVT system were calculated as 0.32; 801 kWh/a; \$ 202 and \$1363, respectively. The produced power amounts by the PV and PVT systems were founded as 98.4 W and 363.8 W in average respectively. Maintenance and repair costs for both PV and PVT systems were

ignored. It is calculated that the PVT system has considerably short payback time after 9 years of operation; while the payback period of PV was found as 16 years.

**Table 2.** Economical analysis of PV system by NPV method

Period (Years)	0	1	2	3	4	5	6	7	8
Initial Investment Cost (\$)	-	1169.00							
Benefits Per Year (\$)		83.30	83.30	83.30	83.30	83.30	83.30	83.30	83.30
Maintenance and Repair Costs (\$)		-0.11	-0.11	-0.11	-0.11	-0.11	-0.11	-0.11	-0.11
Interest rate	0.01	0.01	0.01	0.01	0.01	0.01	0.01	0.01	0.01
Net cash flow (\$)		83.19	83.19	83.19	83.19	83.19	83.19	83.19	83.19
Discounted net flow (\$)	0.99	0.99	0.98	0.97	0.96	0.95	0.94	0.93	0.92
NPV		82.36	81.55	80.74	79.94	79.15	78.37	77.59	76.82
		-1086.64	-1005.09	-924.35	-844.41	-765.26	-686.89	-609.30	-532.48

Period (Years)	9	10	11	12	13	14	15	16
Initial Investment Cost								
Benefits Per Year	83.30	83.30	83.30	83.30	83.30	83.30	83.30	83.30
Maintenance and Repair Costs	-0.11	-0.11	-0.11	-0.11	-0.11	-0.11	-0.11	-0.11
Interest rate	0.01	0.01	0.01	0.01	0.01	0.01	0.01	0.01
Net cash flow	83.19	83.19	83.19	83.19	83.19	83.19	83.19	83.19
Discounted net flow	0.91	0.91	0.90	0.89	0.88	0.87	0.86	0.85
NPV	76.06	75.31	74.56	73.82	73.09	72.37	71.65	70.94
	-456.42	-381.11	-306.55	-232.72	-159.63	-87.26	-15.61	55.34

#### 4. Conclusion

Photovoltaic (PV) solar cells can convert a limited fraction of the solar radiation to electrical energy. Depending on the spectral properties of the materials of solar cells, a large proportion of the solar radiation cannot be converted to the electricity and an excessive heat load is occurred in the photovoltaic material. Solar spectra have a wide range of wavelength from 200 nm to 2500 nm, however a solar cell only transform the portion corresponding to the its spectral response ranges into electricity. Electrical conversion efficiency of the solar cell decreases both instantaneously and for long term due to excessive heat load generated on the solar cell and high internal resistance. Furthermore, this effect could damage the material in long term. It is reported in the literature that a temperature rises of 1 °C results in the loss of performance of PV panel by 0.5 % [42]. At this point, photovoltaic thermal (PVT) systems have been designed with the goal of removing this excessive heat. PVT systems produce both electrical and thermal energy by a single module. With this advantage, PVT systems are preferable for supplying energy demand of residential sector, especially.

In the present study, it was aimed to present a comparative study on the energetic-exergetic and economical performance of PVT system based monocrystalline silicon solar cells and a copper plate with copper tubes on the back for water heating.

The main conclusions, which may be drawn from the results of the present study, are listed as follows:

- The useful energy rates ( $W$ ) of PVT system are considerably greater than the useful energy rates ( $W$ ) of the PV system.
- It is remarkable that the surface temperature of the PVT system is higher than the surface temperature of the PV system.
- The electrical efficiency values of the PVT system are slightly higher than the electrical energy efficiency values of the PV system. The overall energy efficiency of the PVT system has been reached up to 0.54 and average value was calculated as 0.32.
- The exergy efficiency values of the PVT system are greater than the exergy efficiency values the PV system.
- Exergy destruction values of PV system are slightly higher than the PVT system.
- Entropy generation rates increase by increasing surface temperatures of PVT system. It is possible to decrease the entropy generation of PVT system by decreasing surface temperature of PVT system.
- The PVT system has considerably short payback time after 8 years of operation; while the payback period of PV was found as 16 years.

In the present study, a PVT system has been compared to a conventional PV panel by analysing these systems thermodynamically and economically. It is expected that this study could be very beneficial to researchers and practitioners dealing with the PVT systems to improve their systems efficiently. It is hoped that this study could help to understand the actual performance of PVT systems for building applications.

### Acknowledgement

This present work was developed within the framework of research projects having ID s 214M615 and 110M008 fully funded by The Scientific and Technological Research Council of Turkey (TUBITAK). The author would like to thank TUBITAK for the financial support given to the projects.

### Nomenclature

$A$	area, $m^2$
$C_p$	specific heat capacity, $J/kgK$
$\dot{E}_x$	exergy rate, $W$
$I_t$	Solar irradiance on the surface, $W/m^2$
$I$	current, $A$
$\dot{m}$	mass flow rate, $kg/s$
$\dot{S}$	entropy generation rate, $W/K$
$\dot{Q}$	useful energy rate, $W$
$T$	temperature, $K$
$V$	voltage, $V$
$\dot{W}$	work, $W$
$\psi_{solar}$	The maximum efficiency ratio
TL	Turkish Liras

### Greek letters

$\varepsilon$	exergy efficiency
---------------	-------------------

$\eta$  energy efficiency

$\psi$  specific exergy

### Subscripts

dest destruction

gen generated

in inlet

out outlet

pv photovoltaic

pvt photovoltaic/thermal

solar solar

th thermal

o environment

### References

- [1] Van Helden W.G.J, Van Zolingen R.J.Ch, Zondag H.A. PV Thermal systems: PV panels supplying renewable electricity and heat, *Progress in Photovoltaics: Research and Applications*, 2004; 12: 415–26. <https://doi.org/10.1002/ppp.559>
- [2] Hasan M.A. and Sumathy K. Photovoltaic thermal module concepts and their performance analysis: A review. *Renewable and Sustainable Energy Reviews*, 2010; 14:1845–1859. <https://doi.org/10.1016/j.rser.2010.03.011>
- [3] Tripanagnostopoulos Y., Nousia T.H., Souliotis M., Yanoulis P. Hybrid photovoltaic/thermal systems, *Solar Energy*, 2002; 72: 217-234. [https://doi.org/10.1016/S0038-092X\(01\)00096-2](https://doi.org/10.1016/S0038-092X(01)00096-2)
- [4] Tripanagnostopoulos Y. Aspects and improvements of hybrid photovoltaic/thermal solar energy systems. *Solar Energy*, 2007; 81: 1117–1131. <https://doi.org/10.1016/j.solener.2007.04.002>
- [5] Erdil E., Ilkan M., Egelioglu F. An experimental study on energy generation with a photovoltaic (PV)-solar thermal hybrid system. *Energy*, 2008;33:1241– 1245. <https://doi.org/10.1016/j.energy.2008.03.005>
- [6] Dubey S. and Tiwari G.N. Thermal modeling of a combined system of photovoltaic thermal (PVT) solar water heater. *Solar Energy*, 2008; 82: pp. 602–612. <https://doi.org/10.1016/j.solener.2008.02.005>
- [7] Dubey S. and Tiwari G.N. Analysis of PVT flat plate water collectors connected in series', *Solar Energy*, 2009; 83:1485–1498. <https://doi.org/10.1016/j.solener.2009.04.002>
- [8] Chow T.T., Chan A.L.S., Fong K.F., Lin Z., Heb W., Ji, J. Annual performance of building-integrated photovoltaic/water-heating system for warm climate application. *Applied Energy*, 2009; 86: 689–696. <https://doi.org/10.1016/j.apenergy.2008.09.014>
- [9] Kumar S., and Tiwari A. Design, fabrication and performance of a hybrid photovoltaic/thermal (PV/T) active solar still, *Energy Conversion and Management*, 2010; 51: 1219–1229. <https://doi.org/10.1016/j.enconman.2009.12.033>
- [10] Fang G., Hu H., Liu X. Experimental investigation on the photovoltaic–thermal solar heat pump air-conditioning system on water-heating mode. *Experimental Thermal and Fluid Science*, 2010; 34: 736–743. <https://doi.org/10.1016/j.expthermflusci.2010.01.002>
- [11] Pantic S., Candanedo L., Athienitis A.K. Modeling of energy performance of a house with three configurations of building-integrated photovoltaic/thermal systems. *Energy and Buildings*, 2010; 42: 1779–1789. <https://doi.org/10.1016/j.enbuild.2010.05.014>

- [12] Kamthania D., Nayak S., Tiwari G.N. Performance evaluation of a hybrid photovoltaic thermal double pass facade for space heating. *Energy and Buildings*, 2011; 43: 2274–2281. <https://doi.org/10.1016/j.enbuild.2011.05.007>
- [13] He W., Zhang Y., Ji J. Comparative experiment study on photovoltaic and thermal solar system under natural circulation of water. *Applied Thermal Engineering*, 2011; 31: 3369–3376. <https://doi.org/10.1016/j.applthermaleng.2011.06.021>
- [14] Dupeyrat P., Menezo C., Rommel M., Henning H-M. Efficient single glazed flat plate photovoltaic–thermal hybrid collector for domestic hot water system. *Solar Energy*, 2011; 85: 1457–1468. <https://doi.org/10.1016/j.solener.2011.04.002>
- [15] Tiwari G.N., Mishra R.K., Solanki S.C. Photovoltaic modules and their applications: A review on thermal modelling. *Applied Energy*, 2011; 88: 2287–2304. <https://doi.org/10.1016/j.apenergy.2011.01.005>
- [16] Gang P., Huide F., Jie J., Tin-tai C., Tao Z. Annual analysis of heat pipe PVT systems for domestic hot water and electricity production. *Energy Conversion and Management*, 2012; 56:8–21. <https://doi.org/10.1016/j.enconman.2011.11.011>
- [17] Fu H.D., Pei G., Zhang T., Zhu H.J., Ji J. Experimental study on a heat-pipe photovoltaic/thermal system. *IET Renewable Power Generation*, 2012; 6:129–136. <https://doi.org/10.1049/iet-rpg.2011.0142>
- [18] Chow T.T., Pei G., Fong K.F., Lin Z., Chan A.L.S., Ji J. Energy and exergy analysis of photovoltaic–thermal collector with and without glass cover. *Applied Energy*, 2009; 86:310–316. <https://doi.org/10.1016/j.apenergy.2008.04.016>
- [19] Tiwari A., Dubey S., Sandhu G.S., Sodha M.S., Anwar S.I. 'Exergy analysis of integrated photovoltaic thermal solar water heater under constant flow rate and constant collection temperature modes', *Applied Energy*, 2009; 86:2592–2597. <https://doi.org/10.1016/j.apenergy.2009.04.004>
- [20] Joshi A.S., Dincer I., Reddy B.V. Performance analysis of photovoltaic systems: A review. *Renewable and Sustainable Energy Reviews*, 2009; 13: 1884–1897. <https://doi.org/10.1016/j.rser.2009.01.009>
- [21] Sarhaddi F., Farahat S., Ajam H., Behzadmehr A. Exergetic performance assessment of a solar photovoltaic thermal (PV/T) air collector, *Energy and Buildings*, 2010; 42: 21984–21998. <https://doi.org/10.1016/j.enbuild.2010.07.011>
- [22] Saidur R., BoroumandJazi G., Mekhlif S., Jameel M. Exergy analysis of solar energy applications. *Renewable and Sustainable Energy Reviews*, 2012;16: 350– 356. <https://doi.org/10.1016/j.rser.2011.07.162>
- [23] Ozturk M., Ozek N. Batur H., Koc M. Thermodynamic and life cycle assessment of flat-plate collector, photovoltaic system and photovoltaic thermal collector. *International Journal of Exergy*, 2012; 11:229-251. <https://doi.org/10.1504/IJEX.2012.049745>
- [24] Barnwal P. and Tiwari A. Thermodynamic performance analysis of a hybrid Photovoltaic-Thermal (PV/T) integrated greenhouse air heater and dryer. *International Journal of Exergy*, 2009; 6:111-130. <https://doi.org/10.1504/IJEX.2009.023348>
- [25] Kumar S. and Tiwari G. N. Thermal modelling, validation and exergetic analysis of a hybrid Photovoltaic/Thermal (PV/T) active solar still. *International Journal of Exergy*, 2009; 6:567-591. <https://doi.org/10.1504/IJEX.2009.026678>
- [26] Tiwari A; Sandhu G.S., Barnwal P., Sodha M.S. Energy and exergy metrics analyses of Hybrid Photovoltaic-Thermal air collector. *International Journal of Exergy*, 2009; 6: 729-748. <https://doi.org/10.1504/IJEX.2009.027499>
- [27] Pang W, Liu Y, Shao S, Gao X. Empirical study on thermal performance through separating impacts from a hybrid PV/TE system design integrating heat sink. *International Communication in Heat and Mass Transfer*, 2015;60:9–12. <https://doi.org/10.1016/j.icheatmasstransfer.2014.11.004>

- [28] Agrawal S, Tiwari A. Experimental validation of glazed hybrid micro-channel solar cell thermal tile. *Solar Energy*, 2011; 85: 3046–56. <https://doi.org/10.1016/j.solener.2011.09.003>
- [29] Sardarabadi M, Hosseinzadeh M, Kazemian A, Passandideh-Fard M. Experimental investigation of the effects of using metal-oxides/water nanofluids on a photovoltaic thermal system (PVT) from energy and exergy viewpoints. *Energy* 2017; 138:682–95. <https://doi.org/10.1016/j.energy.2017.07.046>
- [30] Stropnik R, Stritih U. Increasing the efficiency of PV panel with the use of PCM. *Renewable Energy*, 2016;97:671–9. <https://doi.org/10.1016/j.renene.2016.06.011>
- [31] Han X, Wang Y, Zhu L. The performance and long-term stability of silicon concentrator solar modules immersed in dielectric liquids. *Energy Conversion and Management*, 2013; 66:189–98. <https://doi.org/10.1016/j.enconman.2012.10.009>
- [32] He W, Chow T-T, Ji J, Lu J, Pei G, Chan L-S. Hybrid photovoltaic and thermal solar collector designed for natural circulation of water. *Applied Energy* 2006;83:199–210. <https://doi.org/10.1016/j.apenergy.2005.02.007>
- [33] Karami N, Rahimi M. Heat transfer enhancement in a PV module using Boehmite nanofluid. *Energy Conversion and Management*, 2014;86:275–85. <https://doi.org/10.1016/j.enconman.2014.05.037>
- [34] Karami N, Rahimi M. Heat transfer enhancement in a hybrid microchannel-photovoltaic module using Boehmite nanofluid. *International Communication in Heat Mass Transfer*, 2014;55:45–52. <https://doi.org/10.1016/j.icheatmasstransfer.2014.04.009>
- [35] Radwan A, Ahmed M, Ookawara S. Performance enhancement of concentrated photovoltaic systems using a microchannel heat sink with nanofluids. *Energy Conversion and Management*, 2016;119:289–303. <https://doi.org/10.1016/j.enconman.2016.04.045>
- [36] Barrau J, Rosell J, Chemisana D, Tadriss L, Ibaez M. Effect of a hybrid jet impingement/micro-channel cooling device on the performance of densely packed PV modules under high concentration. *Solar Energy*, 2011; 85:2655–65. <https://doi.org/10.1016/j.solener.2011.08.004>
- [37] Nizetic S., Coko D, Yadav A, Grubisic-Cabo F. Water spray cooling technique applied on a photovoltaic panel: the performance response. *Energy Conversion and Management* 2016;108:287–96. <https://doi.org/10.1016/j.enconman.2015.10.079>
- [38] Ghadiri M, Sardarabadi M, Pasandideh-fard M, Moghadam AJ. Experimental investigation of a PVT system performance using nano Ferrofluids. *Energy Conversion and Management*, 2015;103:468–76. <https://doi.org/10.1016/j.enconman.2015.06.077>
- [39] Hasan HA, Sopian K, Jaaz AH, Al-Shamani AN. Experimental investigation of jet array nanofluids impingement in photovoltaic/thermal collector. *Solar Energy* 2017;144:321–34. <https://doi.org/10.1016/j.solener.2017.01.036>
- [40] Cengel Y. A., and Boles, A. *Thermodynamics: An Engineering Approach* 8th Edition, 2014, McGraw Hill Education, ISBN:978-0073398174.
- [41] Petela R. Exergy analysis of the solar cylindrical-parabolic cooker. *Solar Energy*, 2005;79: 221–33. <https://doi.org/10.1016/j.solener.2004.12.001>
- [42] B.J. Brinkworth, B.M. Cross, R.H. Marshall, H. Yang, Thermal regulation of photovoltaic cladding consequences, *Solar Energy*, 1997; 61:169-178. [https://doi.org/10.1016/S0038-092X\(97\)00044-3](https://doi.org/10.1016/S0038-092X(97)00044-3)



## *Research on Engineering Structures & Materials*

Research Article

1 **Hakan Sarıkaya, Gülşah Susurluk**

Effect of polypropylene fiber addition on thermal and mechanical properties of concrete

Research Article

13 **Vebil Yıldırım**

Exact radial free vibration frequencies of a thick-walled sphere made of an isotropic and homogeneous material A case study with a carbon nanofiller reinforced aluminum hollow sphere

Research Article

33 **Zeynep Ömeroğulları Başyiğit**

Inclusion compound formation between hazelnut oil and gamma cyclodextrin

Research Article

43 **M. G. Sobamowo**

Finite element analysis of transient thermal performance of a convective-radiative cooling fin: effects of fin tip conditions and magnetic field

Research Article

75 **Canan Kandilli**

Finite element analysis of transient thermal performance of a convective-radiative cooling fin: effects of fin tip conditions and magnetic field

C  
O  
N  
T  
E  
N  
T



Research on  
Engineering  
Structures & Materials

